論文 / 著書情報
Article / Book Information

題目(和文)	CH3Fをドープした固体パラ水素の局所的な構造に対する中赤外高分解能分光研究
Title(English)	High resolution infrared spectroscopic studies for the local structure of para-hydrogen crystal around dopant CH3F
著者(和文)	川﨑博之
Author(English)	Hiroyuki Kawasaki
出典(和文)	学位:博士(理学), 学位授与機関:東京工業大学, 報告番号:甲第10401号, 授与年月日:2017年3月26日, 学位の種別:課程博士, 審査員:金森 英人,上妻 幹旺,田中 秀数,齋藤 晋,大島 康裕
Citation(English)	Degree:Doctor (Science), Conferring organization: Tokyo Institute of Technology, Report number:甲第10401号, Conferred date:2017/3/26, Degree Type:Course doctor, Examiner:,,,,
学位種別(和文)	博士論文
Type(English)	Doctoral Thesis

High resolution infrared spectroscopic studies for the local structure of *para*-hydrogen crystal around dopant CH_3F

HIROYUKI KAWASAKI

The Department of Physics
Tokyo Institute of Technology

February, 2017

Abstract

Solid *para*-H_2 is well known as a prototypical quantum solid. There has been considerable previous experimental and theoretical research. However, the characters of the local structure of *p*-H_2 crystal around dopant have not been cleared yet. This research surveyed mainly four physical subjects related to the local structure of solid *p*-H_2 around dopant molecule.

The first subject is about the nuclear spin conversion rate of *o*-H_2 molecule in solid *p*-H_2. The temporal behaviors of the absorption spectrum of CH_3F-(*o*-H_2)$_n$ were observed. The spectral change is caused by the nuclear spin conversion of *o*-H_2 molecules in the first nearest neighbor site of CH_3F. The self-conversion rate and the catalyzed-conversion rate were estimated by fitting analysis. The decay time of the catalyzed-conversion was estimated to be 24.4(8) hours. This is the first time to estimate the catalyzed-conversion rate between one *o*-H_2 and one dopant molecule. From this research, we found that the catalyzed-conversion rate of *o*-H_2 by CH_3F is faster than the self-conversion rate, but the difference between them are not so large. The effect of CH_3F to the nuclear spin conversion of *o*-H_2 is not only to do the catalyzed-conversion, but also to accelerate the self-conversion of *o*-H_2 since CH_3F makes *o*-H_2 molecules come close to it. Thus, the effects of the dopant molecules to the nuclear spin conversion of *o*-H_2 should be treated from some points of view. This research could contribute not only to the knowledge of the system of CH_3F in solid *p*-H_2 but also the development of the detailed physical implications of nuclear spin conversion of *o*-H_2 with the dopant in solid *p*-H_2.

The second subject is about the origin of unknown peaks. New satellite series were found to the lower energy side of each main peak of the ν_3 band of CH_3F embedded in a *p*-H_2 crystal. All the peaks showed a common red shouldered line profile, which corresponds to partly resolved transitions of *ortho*- and *para*- CH_3F. Some experimental results may suggest that these satellite series originate from a family of CH_3F clusters involving *o*-H_2 in second nearest neighbor sites. A model function assuming this idea was used to resolve the observed spectrum into each Lorentzian component, and then the detailed features of these series were studied. The peak intervals in the series are not as equally spaced as the main series, but there is a strong resemblance to the satellite series. We proposed that the effect of *o*-H_2 molecules in the second nearest neighbor site of CH_3F could not be ignored.

The third subject is about the alignment of the dopant molecule. The polarization dependence of the ν_3 vibrational transition of CH_3F, whose rotational motion is hindered in *p*-H_2 crystal, was observed.

The experimental results were well explained by a simple six-way vacancy model and the alignment angle in the crystal is determined. The CH_3F is not aligned along the *c*-axis but tilted to 64° from the *c*-axis. This is the first time to estimate the alignment of dopant molecule in solid *p*-H_2 by experimentally. The method to estimate the alignment of the dopant can be used for other dopant molecules. This research could contribute to some studies, like which use the orientation of dopant molecules.

The fourth subject is about the structural changes of CH_3F-(*o*-H_2)$_n$ by the pumping lasers. By using two QC lasers, the processes of the structural change by the pumping beam were observed at the first time. In order to estimate each rate for the structural change of each cluster, these pump-probe experimental results were analyzed by using some model functions. The fitting results showed that the local thermal energy of the *p*-H_2 crystal around CH_3F increases and the resonance frequency of the CH_3F in the cluster is shifted. This research could contribute to understanding the mechanism of the thermal relaxation in solid *p*-H_2 around dopant.

In addition, some unknown peaks (e.g. the *d* series and *n* = 3' peak) have been surveyed. The characters and the origins for them were proposed. Some theoretical supports are quite important for the determination of the origins of these peaks.

From this research, some characters of solid *p*-H_2 to the dopant molecule were cleared. Furthermore, this research developed the knowledges about the interaction between *o*-H_2 molecules and CH_3F. The characters of the local structure of solid *p*-H_2 revealed in this research are not only for dopant CH_3F. These achievements can contribute to the studies for other dopants in solid *p*-H_2 and also the studies for the characters of solid *p*-H_2 itself.

Contents

Chapter 1 Introduction

In Chapter 1, the background of this research is presented. Section 1.1 and 1.2 explain the hydrogen molecules and the solid *para* hydrogen, respectively. Section 1.3 presents the overview of this thesis.

§ 1.1 *para*-hydrogen molecule

Hydrogen molecules are distributed to two types, *ortho*-H_2 (I = 1) and *para*-H_2 (I = 0). From the symmetry restriction of the wave function, the rotational quantum number J of *p*-H_2 is even and that of *o*-H_2 is odd. This fact was found at around 1927 [1-3]. At room temperature, the *ortho-para* ratio is 3:1 due to the statistical weight of each nuclear spin state and that is called "normal hydrogen". It is known that the nuclear spin conversion between *o*-H_2 and *p*-H_2 is almost forbidden without paramagnetic catalysts [4]. Therefore they can be treated as different molecules. In liquid and solid, however, the spin conversion cannot be neglected [5].

The energy levels of H_2 molecules are depicted in Fig. 1-1. The energy difference between their lowest levels of *p*-H_2 and *o*-H_2 is about 15.08 meV. The energy difference cannot be neglected since it makes "boil-off" problem. In these days, hydrogen has been attracting attention as one of the fuels. The possibility and scalability of this new candidate for fuels should not be discussed in this thesis. But without this discussion, it would be easily imagined that transforming the hydrogen gas to liquid is necessary in order to store and transport efficiently on the industry scale. The energy for sublimation of hydrogen is about 12 meV, thus the released energy at the conversion from *o*-H_2 to *p*-H_2 is enough to sublimate [6]. This is the boil-off problem. From this issue, the conversion of *o*-H_2 to *p*-H_2 before the storage of hydrogen is necessary and also the invention for the reasonable conversion way would be hoped. The mechanism of conversion has been investigated by some groups [7-12]. In addition to them, in order to understand the detail of the conversion process, the nuclear spin conversion with some molecules in solid *p*-H_2 has been researched for a long time

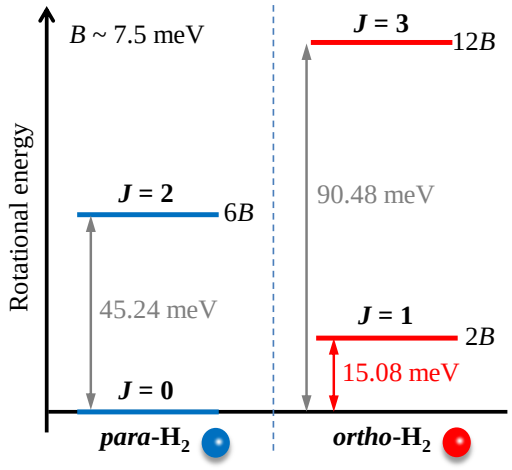

Fig. 1-1. The rotational energy levels of hydrogen molecule

[13-16]. This research also has curious to it and has researched the nuclear spin conversion at local region around dopant molecule.

§ 1.2 Solid *para*-hydrogen

Solid *p*-H_2 is well known as a prototypical quantum solid due to the light mass of the H_2 molecule and its weak and relatively isotropic intermolecular interactions. It is well known that solid *p*-H_2 forms the hexagonal close-packed (hcp) structure at a low temperature and at low concentration of *o*-H_2, as shown in Fig. 1-2. Squared distances and numbers of neighbors of solid *p*-H_2 are listed in Table 1-1. The lattice constant *a* and the *c/a* ratio for solid *p*-H_2 were also estimated in previous research. If the ratio equals $(8/3)^{1/2}$, the crystal is constructed by ideal spheres. In previous studies, some values of the lattice constant were reported since they calculated with different theoretical models and for different environments. Furthermore, the lattice constant for solid *p*-H_2 was reported 3.77-3.789 Å depending on the concentration of *o*-H_2 [17]. It should be pointed out that the lattice constant and the *c/a* ratio of solid *p*-H_2 have some fluctuation by the environment in it. In Ref. 4, the lattice constant of *p*-H_2 crystal was reported as 3.78 Å and the amplitude of zero-point vibration is estimated about 18% to the lattice constant. The *c/a* ratio for solid *p*-H_2 was reported that it is very close to the hcp value $(8/3)^{1/2}$ for solid *p*-H_2 at zero pressure in the reference. In Ref. 18, the lattice constant *a* and *c* of solid normal hydrogen were reported as 3.75 Å and 6.12 Å, respectively. Therefore, the *c/a* ratio is ~ 1.63 and this value is very close to $(8/3)^{1/2} = 1.633$.

There has been considerable previous experimental and theoretical research. As for spectroscopic studies, Welsh *et al.* observed infrared spectra of solid *p*-H_2 in 1955 [19,20], and Raman spectra in 1956 [21]. The physical properties of solid *p*-H_2 were summarized by Silvera [17] and Van Kranendonk [4] in the early 1980's. Then in the late 1980's, high-resolution laser spectroscopy of

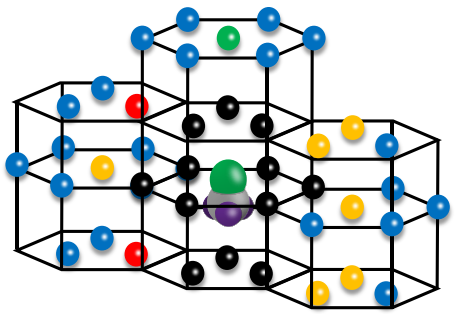

Fig. 1-2. The hcp structure of solid *p*-H_2. Each sphere shows the *p*-H_2 molecule. The black, red, green, yellow, and blue spheres indicate the 1st, 2nd, 3rd, 4th, and above 5th sites, respectively.

Table 1-1. Squared distances and numbers of neighbors of solid *p*-H_2 with hcp structure [4].

Neighbor *i*	$(R_i/R_1)^2$	Number of sites
1	1	12
2	2	6
3	8/3	2
4	3	18

p-H_2 crystals by Oka's group in Chicago showed that rovibrational transitions of H_2 itself could be as narrow as 0.001 cm^{-1} [22]. Furthermore, they reported the split of the rovibrational transitions of *o*-H_2 and *p*-H_2 by the effect of *o*-H_2 molecules [23-26]. M. Mengel *et al.* also reported the detail of the first vibrational overtone spectrum. Moreover, they reported the double transitions (e.g. $U_1(0)+Q_1(0)$, and $Q_1(0)+Q_1(1)$) and triple transitions (e.g. $S_1(0)+Q_1(0)+Q_1(0)$) by using high-resolution FTIR measurement [27-29]. From their reports, the narrow linewidths of the absorption spectra in *p*-H_2 crystal describe that the interaction between *p*-H_2 molecules is enough weak in solid *p*-H_2. Further, Oka's group showed that some dopant molecules can rotate freely in *p*-H_2 crystals, giving rovibrational spectra even narrower than in the gas phase [30-32]. Therefore, solid *p*-H_2 has been recognized as unique matrix isolation medium and many spectroscopic studies have been reported by using high-resolution FTIR spectrometers [33-38]. The target molecules studied in *p*-H_2 crystals can be classified into two groups, namely molecules which can rotate in the crystal and those which cannot. In the former case, the *M*-degeneracy of a rotational state splits in the crystal field. Therefore, polarization spectroscopy is useful to assign the spectral peaks, because the crystal *c*-axis is known to be normal to the substrate [39]. Using the selection rule on ΔM, the alignment of a dopant molecule was studied [33,34]. In the latter case, without rotation, there exist no *M*-components. Only a single transition which corresponds to a pure $Q(0)$ vibrational transition is observed because the rotational motion is hindered. There are some studies to the latter case [38,40], however, the alignments of the doped molecules have not been cleared yet. The knowledge of the orientation of the dopant molecules is very important. For example, the surveys which need to switch the direction of dopant molecules should know the alignment of the dopants. This research tried to determine the orientation of doped molecules, CH_3F, by the experimental approach.

The theoretical approach to the *p*-H_2 crystal has also researched for a long time. The mechanism of the interaction of *o*-H_2 in solid *p*-H_2, like *ortho-para* conversion, has been studied theoretically from the 1950s [41-43]. The structure of *p*-H_2 crystal has been studied from the late 1970's [44,45]. These studies described the difference between in-plane and out-of-plane for a pair of *o*-H_2 molecules. The Monte Carlo studies to *p*-H_2 clusters started from the 1990s [46,47]. The $(p\text{-}H_2)_N$ cluster size they were able to calculated at that time was up to $N = 34$. The theory has been improved, and recently, the vacancy model [48,49] and the potential of the *p*-H_2 cluster with other molecules [50,51] were studied. However, a reasonable model to explain some experimental results in *p*-H_2 crystal has not been established completely due to the large zero-point vibration that solid *p*-H_2 has. Therefore, the physical phenomenon should be observed by experimental approach for supporting the theoretical approach in the future.

In these days, the studies using the solid *p*-H_2 can be divided into two; studying the target molecules by using *p*-H_2 as a matrix isolation medium, and studying the properties of *p*-H_2. One of the purposes of the formers is to observe the chemical reaction or understand the formations of target complexes in the *p*-H_2 crystal since it enables us to understand the detailed interpretation of them. In fact, the characters of pure solid *p*-H_2 have been studied enough. However, the characters of the local structure around dopant have not been studied enough. At locally, the interaction between *p*-H_2 and *o*-H_2, and *o*-H_2 molecules have been studied but the interaction between *o*-H_2 molecule and the dopant molecule has not been studied completely. In order to use the solid *p*-H_2 as a matrix isolation medium, the local characters around the dopant molecule trapped in solid *p*-H_2 should be more identified. This research focuses on the local properties of the *p*-H_2 crystal especially around CH_3F doped in the crystal.

The observation of the ν_3 vibration band (~ 1040 cm^{-1}) in CH_3F shows a distinct spectral feature due to the CH_3F-(*ortho*-H_2)$_n$ (n = 0-12) clusters [52,53]. The peak position of the n = 0 cluster is 1040.19 cm^{-1}. The band origin ν_0 of CH_3F is 1048.610767(62) cm^{-1} [54]. Therefore, the matrix shift is -8.42 cm^{-1}. They reported that the value of the matrix shift is typical for small molecules isolated in solid *p*-H_2. Each line width of these peaks is much narrower than that in the rare gas matrix [55,56]. Absorption peaks of some other molecules in solid *p*-H_2 are also shifted but the situation for the ν_3 vibration band of CH_3F that each cluster's peak is obviously separated is unusual. In fact, the other vibrational bands of CH_3F as ν_4 and $2\nu_2$ are very broad and each cluster's peak is not observed separately. In order to survey the characters of the local structure in solid *p*-H_2, we need to observe each cluster's peak separately. Therefore, the ν_3 vibration band of CH_3F is good for the investigation of the local structure of solid *p*-H_2. In our laboratory, high-resolution measurement has been performed by McKellar *et al.* using a quantum cascade laser (QCL) [57]. We found that the spectrum for each cluster involves many weak satellite peaks, and some unidentified lines (d = 1, 2, *etc.*) were also found in the middle area of the cluster peaks. Additionally, the photochromic phenomenon between the peaks of the clusters was found by using a high power of QCL (~ 30 mW) [58]. However, the mechanism of this photochromic phenomenon has not been clearly understood yet. The origins of satellite peaks and other unknown peaks should be elucidated in order to understand the phenomenon occurs in solid *p*-H_2, especially the local region around CH_3F. Furthermore, the photochromic phenomenon also should be identified since it can promote to understand the effect of *o*-H_2 molecules to dopant molecules and also the character of *p*-H_2 crystal.

§ 1.3 Introduction of this thesis

In this research, the topics are (1) to estimate the nuclear spin conversion rate of *o*-H_2 forming the cluster with CH_3F, (2) to explain the physical origin for 6 satellite peaks: *n*'-series, which were observed in any clusters, and (3) to identify the alignment of CH_3F in solid *p*-H_2, and finally (4) to understand the photochromic phenomenon in this system. The purpose of these four topics is to promote the understanding the microscopic characters of *p*-H_2 crystal around the dopant molecules. This knowledge could contribute to the other studies that use *p*-H_2 crystal as a matrix isolation medium in order to observe the intermediate state of the chemical reaction or photoreaction of the dopant molecule in it [37,59,60], for example.

In Chapter 2, some instruments and the experimental ways of this research are reported.

In Chapter 3, the temporal behavior of the absorption spectrum for CH_3F-(*o*-H_2)$_n$ cluster is reported. In order to estimate the nuclear spin conversion rate of *o*-H_2 forming the cluster with CH_3F, the temporal behavior is analyzed with model function. And also, the physical origin for some unknown peaks is presented.

In Chapter 4, the experimental results on the temporal behavior, temperature dependence and pumping experiment in order to explain the physical origin for 6 satellite peaks are presented. Some contents in this chapter have been already reported as Ref. 61.

In Chapter 5, the experiment on polarization dependence is reported. The alignment of CH_3F in solid *p*-H_2 is estimated. Some contents in this chapter are also seen in Ref. 62.

In Chapter 6, the experimental results on pump-probe experiments are presented. In order to understand the mechanism of the migration of *o*-H_2, the experimental results are analyzed with model functions.

Chapter 2 Experimental procedures

§ 2.1 Method of making sample

2.1.1 Preparation of pure *p*-H_2

Hydrogen molecules are distributed to two types, *ortho*-H_2 (I = 1) and *para*-H_2 (I = 0), as described in Chap. 1. In order to make solid *p*-H_2, we have to prepare pure *p*-H_2 gas. It is known that the nuclear spin conversion between *o*-H_2 and *p*-H_2 is almost forbidden without paramagnetic catalysts. We use a converter with $Fe(OH)_3$ that has been used in our Laboratory [57,58,63]. By passing through the converter, the distribution for rotational state follows the Boltzmann distribution, thus *p*-H_2 (J = 0) dramatically increases if the temperature is enough low. From this point of view, the temperature of catalyst should be kept at around the triple point (13.8 K) when the gas passes through it. From the calculation about thermal equilibrium condition, the ratio of *o*-H_2 (J = 1) to *p*-H_2 (J = 0) at the triple point is about 10^{-5}.

The temperature of the catalyst is measured at two positions on the converter, bottom, and middle, as shown in Fig. 2-1. The converter is inserted in the liquid He tank and the temperature is adjusted by the distance between the bottom of converter and surface of liquid He. In our experiment, the bottom temperature of the converter is kept at 13.4 K. It is lower than the triple point; however, H_2 gas can pass through the catalyst at a rate of 300 ccm. The temperature at middle sensor depends on the remaining amount of liquid He in the tank; therefore, the temperature has some range between other experiments, like 30-50 K. The pure *p*-H_2 gas is stored temporarily (a few hours) in 15 L Pyrex glass vessel.

2.1.2 Method to control the ratio for *o*-H_2 / *p*-H_2

The concentration of *o*-H_2 in *p*-H_2 is about 10 ppm if we prepare it by the way mentioned above. To control the concentration of *o*-H_2 by only changing the converter temperature is so limited because the H_2 gas should change the form to liquid H_2 in order to pass through the catalyst. In this limitation, the temperature could only be changed between 13.8 K and 20 K. If we need more concentration of *o*-H_2, we store a few normal H_2 gas in the vessel before pure *p*-H_2 is stored. For example, we mix 1 Torr normal H_2 gas and 750 Torr *p*-H_2 for making about 1000 ppm (parts per million) *o*-H_2 / *p*-H_2 gas. This estimation follows that the *ortho-para* ratio at room temperature is 3:1. By this way, we

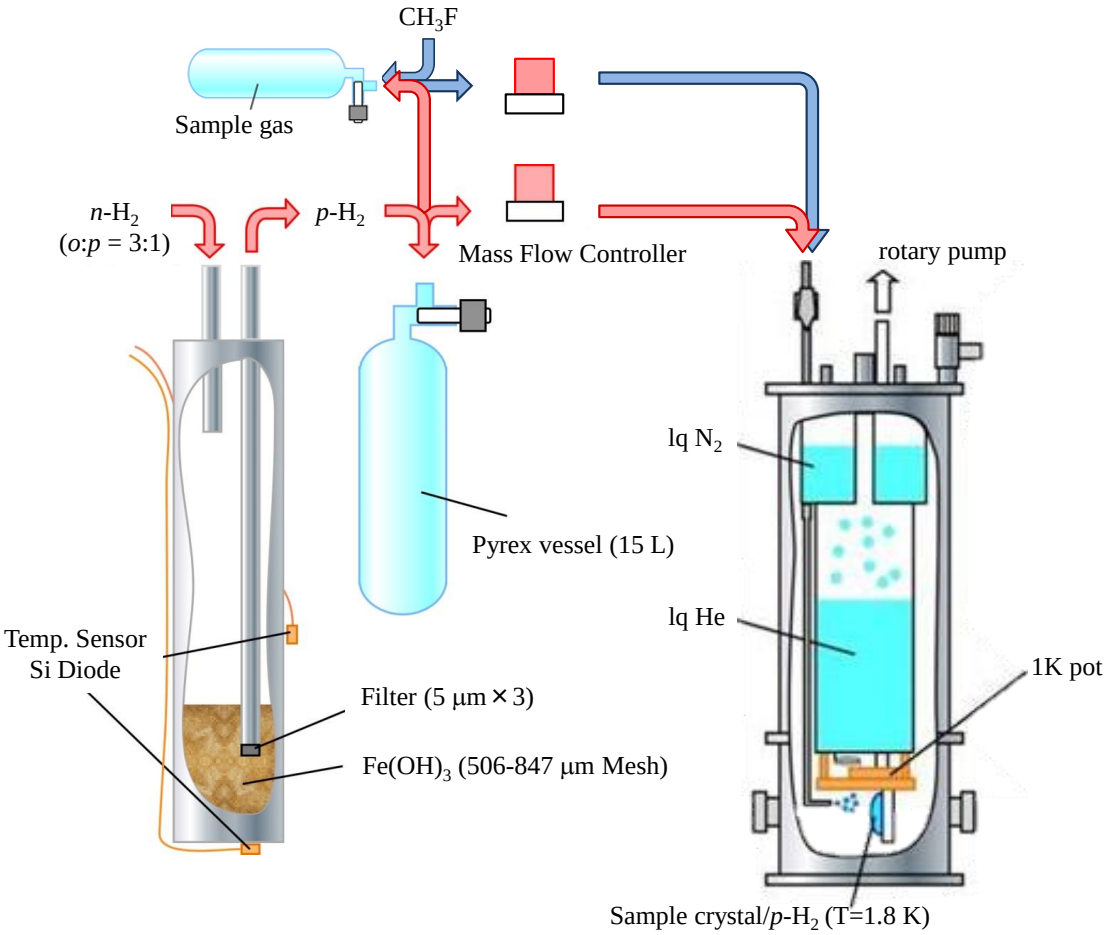

Fig. 2-1. The converter and the way of making sample. (Some parts were depicted by Dr. A. Mizoguchi)

can control the order of the concentration of *o*-H_2 from 10 ppm to 750000 ppm (75 %) thus normal hydrogen.

The determination of the concentration of *o*-H_2 in each sample should be treated very carefully because the concentration might not be constant in one crystal. The position dependence and the time dependence of the concentration should be considered. The ratio of *o*-H_2 would be higher around doped molecules which have the dipole moment, especially after annealing. This expectation was reported in some previous studies [64,65]. The spectrum pattern of CH_3F-(*o*-H_2)$_n$ clusters before annealing follows to the average concentration of this crystal [66]. However, we discuss the environment after annealing. In our case, we use CH_3F that has the dipole moment; therefore, we should treat the ratio very carefully. We should clearly divide which point of view we discuss at the whole sample or at the local point.

2.1.3 Cryostat

Figure 2-2 describes the diagram of the liquid He cryostat for making the sample with solid *p*-H_2. The sample should be kept the temperature around 2 K and the temperature is lower than that of liquid He. The substrate for the sample is cooled by attached to "1 K pot" for achieving the lower temperature. This is partially filled with liquid He fed through a narrow capillary. By evacuating the vaporized He gas in it with a rotary pump, the temperature of the pot and substrate could be cooled below 2 K. The needle bulb showed in the Fig. 2-2 controls the flow rate of the liquid He to flow into the pot.

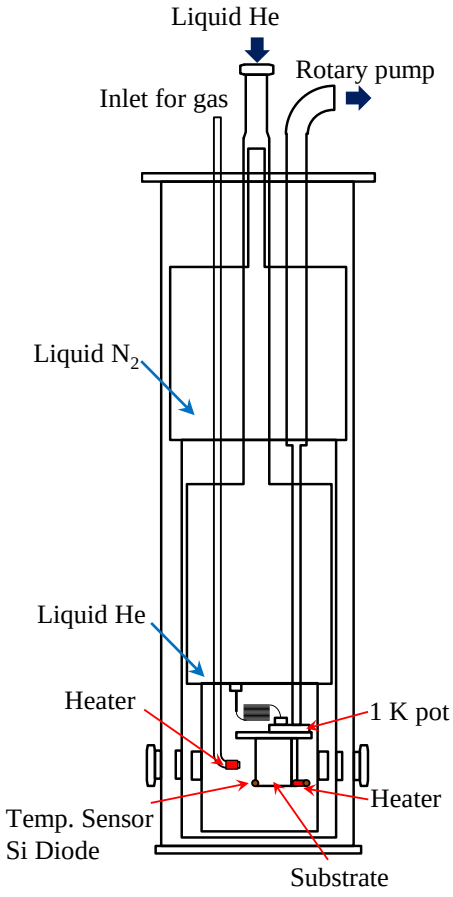

Fig. 2-2. Cryostat

The substrate for the sample is gold coated mirror made of copper. It is attached vertically to the 1 K pot by two copper frames. This mirror system is different from the previous researches in our Laboratory [57,58,63] or others [35,52,53]. The temperature of the substrate is monitored by using silicon diode temperature sensor attached to the frame. Since the material of the mirror and the frames are copper that has very high thermal conductivity, we can treat these frames, substrate, and also the sample crystal are the same temperature. The thermal conductivity of solid *p*-H_2 is about 2 $Wcm^{-1}K^{-1}$ [17] when the temperature is 2 K and the concentration of *o*-H_2 is about 1000 ppm. From the thickness of this sample and the time range of our experiment, the temperature of this sample and the substrate could be treated the same one. The temperature of the substrate is controlled by the balance of a heater on the frame and the flow rate of liquid He, as mentioned above. The substrate is set to 45 degrees to reflect the laser beam at the right angle in order to measure the polarization dependence of the crystal.

2.1.4 Method of making crystal samples

We use Deposition method. This measurement way was mainly established by Fajardo *et al.* [67]. The sample gas is rapidly vaporized to the cooled substrate and deposits, as seen in Fig. 2-1. At that

time, the temperature of the substrate is kept above 2 K. The rate of gas flow is 70 ccm. The flow rate should be kept around this value for keeping the environment in the cryostat [67]. The crystal grows several millimeters thick. The crystal made by this way is not perfect single crystal, therefore the quality of the crystal should be improved by annealing of the substrate [39,67]. In this study, we use one annealing way called "7 K annealing". After the deposition, the crystal is heated up to 7 K briefly and is cooled back to below 2 K [57,58].

CH_3F gas is stored in 1 L Pyrex vessel about a few mTorr. For mixing the sample gas and *p*-H_2 gas, *p*-H_2 gas is taken into the vessel from 15 L vessel to be premixed with CH_3F. At that time, the pressure difference between the two vessels is huge; therefore, it would not be occurred to pass through the CH_3F gas to the 15 L vessel.

First, pure *p*-H_2 gas from 15 L vessel is deposited on the substrate with the flow rate of 70 ccm for 10 - 20 min. Secondly, sample gas is also deposited by the same inlet with the flow rate of 0.2 ccm for around 30 min. Finally, the sample gas is stopped and only *p*-H_2 gas is deposited again for cover the crystal. The time with the flow of the sample gas directly correlates with the population of CH_3F molecules in the sample. By changing the rate of premixing and the flow rate, the CH_3F concentration could be controlled. In this work, the typical concentration is chosen to be 0.4 ppm to prevent the formation of self-clusters $(CH_3F)_m$, as the previous study about supersonic jet matrix isolation [68]. The typical thickness of the crystal is a few mm, through which we could observe convex lens effect by sight. After the deposition, the crystal is annealed by the brief increase of the temperature up to 7 K, then cooled back to 1.8 K for the laser spectroscopic measurement, as mentioned above.

§ 2.2 Infrared spectroscopy by using QCL

We observe the spectra of CH_3F in solid *p*-H_2 by using quantum cascade laser (QCL) [69]. We employ mainly three observation ways which are explained in the following sections.

In general, QCL is one of the semiconductor lasers and it emits middle to far infrared laser beam. The optical physics of a QCL differs from that of a diode laser. The comparison between a diode laser and QCL is described in Fig. 2-3. A diode laser transitions occur between the conduction band and valence band of the semiconductor material, as seen in Fig. 2-3(a). On the other hand, a QC laser transitions occur between the subbands within a given quantum well, as seen in Fig. 2-3(b). One of the advantages of this physical mechanism is that multiple photons can be generated by a

single electron since the electron responsible for the emission of the photon at the active region tunnels into the injector. Therefore, a single electron can make a number of photons that correspond to the number of active regions.

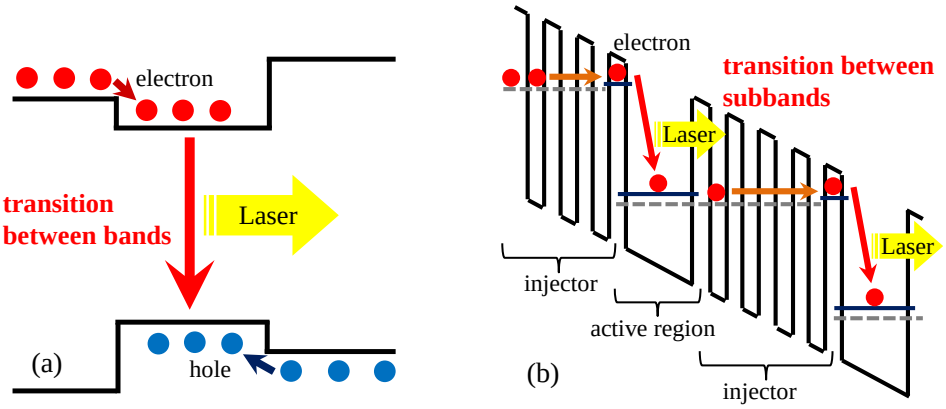

Fig. 2-3. The mechanism of semiconductor laser (a) and quantum cascade laser (b).

2.2.1 Normal one QCL measurement

The laser used in this work for measurement of the ν_3 band of CH_3F is CW quantum cascade laser [Hamamatsu C10337-02], as shown in Fig. 2-4. The QCL used in this work covered the spectral range of 1037.5 - 1042 cm^{-1} corresponding to n = 0 - 3 of the CH_3F-(o-H_2)$_n$ absorption series [52,53]. The line width of the laser is less than 6 MHz which is narrow enough to observe fine details in the spectrum. The output power is several 10 mW. For measurements, the laser power is attenuated down to several μW in order to avoid bleaching effects [58]. The laser frequency is swept by a 500 Hz sawtooth injection current. The spectral range of this sweep is about 1.4 cm^{-1}. The direct absorption signal through the crystal is detected with a MCT detector and averaged in a digital oscilloscope. Typical spectroscopic measurements are done at a temperature of 1.8 K, and the peak

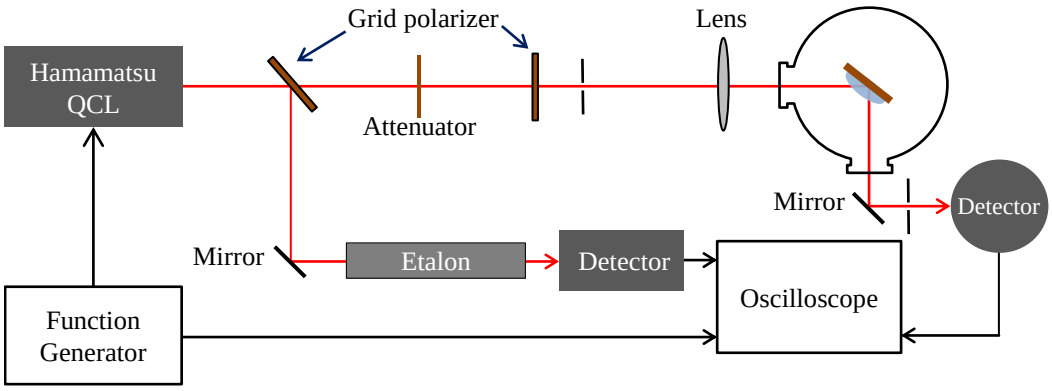

Fig. 2-4. The brock diagram of normal observation by using one QCL

positions of the main series are assumed to be equal to their previously measured values [55]. The spectral peaks of interest here are n = 0 (1040.189 cm^{-1}), n = 1 (1039.483 cm^{-1}), and n = 2 (1038.767 cm^{-1}). The relative frequency of those peaks is interpolated with a free-spaced etalon whose FSR is 0.0097 cm^{-1}.

Figure 2-5(a) shows the observed spectrum on the oscilloscope for one example. The baseline undulates that is caused by some effects like interference at grid polarizer or windows of the cryostat. The observed absorption spectra are converted to absorbance: $\ln[I(\omega)/I_0(\omega)]$, where $I_0(\omega)$ and $I(\omega)$ are the laser intensities before and after the crystal, respectively. Since a proper $I_0(\omega)$ spectrum is not obtained experimentally in this experimental setup, $I_0(\omega)$ is replaced with an approximated polynomial function determined by least-square fitting of the baseline in which there are no absorption lines, as described in Fig. 2-5(b). The black trace in this figure shows the fitting result. From these steps, the absorbance of every spectrum could have a few system errors especially for such kind of spectra in which some peaks are very weak and not observed obviously.

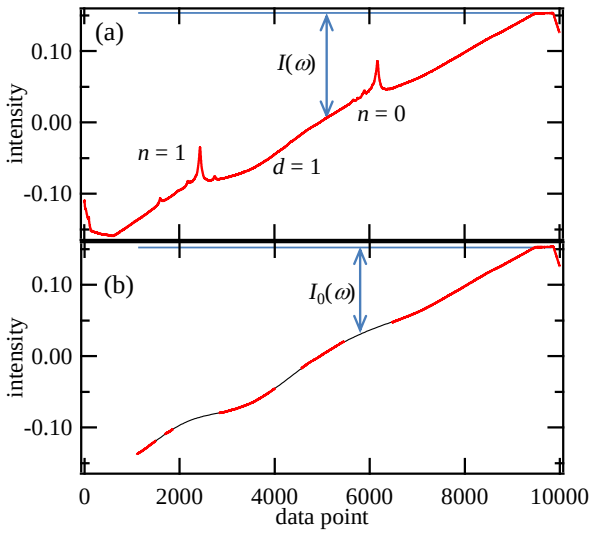

Fig. 2-5. The observed spectrum by oscilloscope. (a) The real spectrum observed by using QCL. The peaks correspond to n = 0 and 1 from the right side, respectively. (b) The masked spectrum for estimating $I_0(\omega)$. The masked points correspond to the peak positions of n = 0 and 1, d = 1 or others are removed. The black trace shows the line profile result for estimating the baseline.

2.2.2 Polarization spectroscopy

The measurement system is almost same to the above one. In order to change the polarization angle of the laser beam, we use two grid polarizers [WGP-8001]. The first polarizer is set at 45° to the original polarization axis of the laser beam. The reflected beam with a half of the power is followed to an etalon for wavelength calibration. The transmitted beam with rest of the power is further controlled to be any polarization angle β by the second polarizer and then used for the polarization spectroscopy of the sample crystal. The intensity of each peak varies at the position in the crystal

because the thickness of the crystal has a shape of thin convex lens profile. Moreover, the intensity of each peak varies with time [57]. Therefore we measure the polarization dependence at the same point in the crystal as quick as possible.

We introduce a Cartesian coordinate system to describe an interaction of the light and molecules in the crystal briefly since we introduce the detail in Chap. 5. The *XY*- plane is set on the surface of the substrate, and the *Z*-axis is normal to the substrate and is expected to be the *c*-axis of the hcp crystal. The laser beam is incident in the *XZ*-plane. The laser incidence angle α is defined by the angle to *Z*-axis. The laser polarization angle β is defined by the angle to *ZX*-plane, in other words, *p*-polarized light corresponds to $\beta = 0$ and *s*-polarized corresponds to $\beta = 90°$.

2.2.3 Pump-probe spectroscopy by using two QCLs

The laser system used in this work for the measurement of structural change of the cluster needs two QCLs, as shown in Fig. 2-6. One is Hamamatsu C10337-02, as mentioned above, and other is THORLABS's QCL [QD9650CM1AS]. It covers the spectral range of 1037.5 - 1040 cm^{-1} corresponding to $n = 0 – 3$ of the CH_3F-(o-H_2)$_n$ absorption series [52,53]. The line width of the laser is as narrow as Hamamatsu one. The output power is less than 70 mW. The sweep range for one scan is smaller than Hamamatsu one, therefore it is used for a pumping laser.

In order to observe the spectrum change, the two laser beam should be completely overlapped. The polarizations of these two laser beams are set for vertical and overlapped by first grid polarizer.

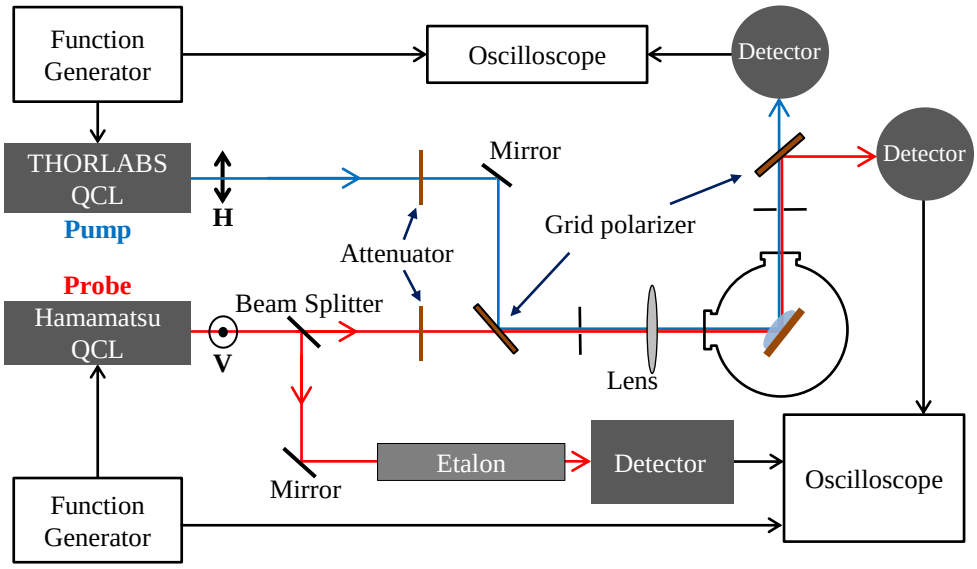

Fig. 2-6. The brock diagram of pump-probe experiments by using two QCL

After passing thorough the sample, the two beams are separated by the second polarizer and follow to each detector.

§ 2.3 FTIR spectroscopy

Figure 2-7 indicates the scheme and block diagram of FTIR spectroscopy. The FTIR is Bruker FTS 120-HR. For MIR region, Glowbar (100 - 5000 cm^{-1}) light source and KBr (400 - 4800 cm^{-1}) beam splitter are used. For NIR region, Tungsten lamp (3000 - 25000 cm^{-1}) light source and CaF_2 (1000 - 10000 cm^{-1}) beam splitter are used. For the detector, MCT (600 - 6000 cm^{-1}) or InSb (1850 - 9000 cm^{-1}) are used. In order to check the direction of *c*-axis of solid *p*-H_2 in this work, we measure the CH_4 spectrum in solid *p*-H_2 by using FTIR, following to the previous research [39]. The resolution is enough to 0.01 cm^{-1} for the check the spectrum peaks of CH_4.

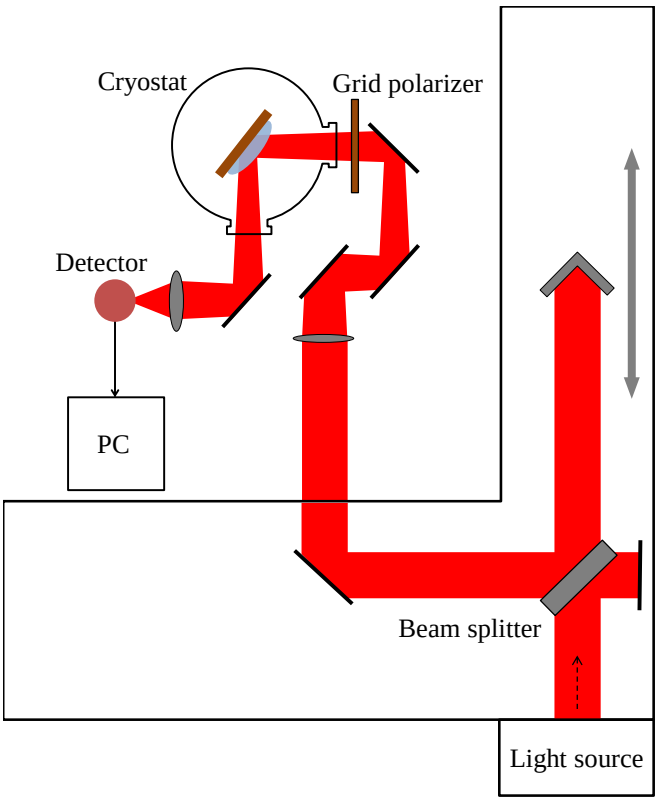

Fig. 2-7. FTIR spectroscopy

Chapter 3 Nuclear spin conversion of *o*-H_2

§ 3.1 Introduction

The nuclear spin conversion rate of *o*-H_2 in solid *p*-H_2 has been researched by theoretically and experimentally for a long time [42,70,71]. In general, H_2 molecules are separated into two that are *para* (I = 0, J = even) and *ortho* (I = 1, J = odd), and the nuclear spin conversion between them is negligible at the gas phase as mentioned in Chapter 1. In solid, however, the spin conversion occurs and the order of the decay time is hours in high *o*-H_2 concentration [5]. The detailed mechanism of the nuclear spin conversion was discussed in a previous research [42], and the interactions that cause the conversion are mainly the following three; the spin-spin interaction, the rotation spin interaction, and the electric quadrupole interaction [17]. The image for the mechanism of the nuclear spin conversion is explained briefly. The nuclear spins of two hydrogen atoms in *ortho*-hydrogen molecule perform the precession movements with the same frequency if these atoms feel the same magnetic field. However, the frequencies of the precession movements of the two atoms are changed if these atoms are in the non-uniform magnetic field. In that case, the interaction between the two hydrogen atoms cannot be neglected and the nuclear spin conversion in *o*-H_2 molecule is occurred. The non-uniform magnetic field for the *o*-H_2 molecule could be made by the other *o*-H_2 molecules or other dopant molecules in its first nearest neighbor sites. Thus, magnetic interactions are quite important for the nuclear spin conversions of *o*-H_2. Therefore, if paramagnetic impurities, such as O_2, exist in the solid H_2, they accelerate the spin conversion rate obviously. In previous studies, some effects of doped molecules to nuclear spin conversion rate of *o*-H_2 have been mentioned and the rate constants were determined [13,14,16,72,73].

These experimental researches for the nuclear spin conversion rate of *o*-H_2 in solid *p*-H_2 can be separated into two types. One type, which is the popular one, determines the nuclear spin conversion rate by observing the change in the absorption intensity of *o*-H_2 with time by FTIR [13]. The absorption spectrum of *o*-H_2 is observed at around 4000 cm^{-1}. The intensities of these peaks relate to the concentration of *o*-H_2 in *p*-H_2 crystal. By observing the change of the peak intensity of *o*-H_2 with time, the temporal behavior of the concentration of *o*-H_2 in *p*-H_2 crystal could be surveyed. From the time dependence of the concentration, the nuclear spin conversion rate of *o*-H_2 in the sample crystal could be estimated. It could be called the macroscopic study. The other type determines it by observing the change in the signal intensities of single and pair *o*-H_2 using NMR [5,74]. The signal

intensities are proportional to the number of the molecules. Therefore, from the temporal behavior of each signal, they estimated the conversion rate. It could be called the microscopic study. Both types have advantages and disadvantages. The former one could be judged by the amount of *o*-H_2 in the crystal directly therefore it can determine the concentration of *o*-H_2 in the whole sample. However, the determined conversion rate includes the time required for forming the pair of *o*-H_2 molecules since the nuclear spin conversion can only be happened when at least two *o*-H_2 molecules form a pair or cluster. Furthermore, *o*-H_2 could form cluster with above two *o*-H_2 molecules. Thus, it can discuss the decay time of concentration of *o*-H_2 for the sample, but cannot discuss the conversion rate of single pair *o*-H_2 molecules. The latter one can observe the time profile of single pair of *o*-H_2 molecules. However, it includes the time forming the larger cluster of *o*-H_2. Since it observes the signal of pair *o*-H_2, the decrease of it means that one *o*-H_2 is converted to *p*-H_2, or breaks up the pair, or one more *o*-H_2 comes and forms cluster of three *o*-H_2 molecules.

Several groups determined the *ortho-para* nuclear spin conversion rate of H_2 with the existence of CH_3F in solid *p*-H_2 [16,65]. In addition to them, Y. P. Lee's group reported that the existence of *o*-H_2 could affect the nuclear spin conversion rate of CH_3F from $I = 3/2$ to $I = 1/2$ [64]. The nuclear spin conversions of some dopant molecules in solid *p*-H_2 were observed [33,75]. It is easy to understand that the magnetic interaction between *o*-H_2 and CH_3F affects both nuclear spin conversion rates. Y. P. Lee's group determined the nuclear spin conversion rate of CH_3F. However, most of the researches about the nuclear spin conversion rate of *o*-H_2 with the existence of CH_3F have been discussed by the macroscopic studies. K. Yoshioka and D. T. Anderson reported the nuclear spin conversion rate of CH_3F and single *o*-H_2 [76]. However, the nuclear spin conversion rate was estimated with divided $n = 0$ cluster and others, therefore it would not be enough in the detail. It's very important to know the effect between *o*-H_2 molecules and between CH_3F and *o*-H_2 since it could promote the understanding the mechanism of the nuclear spin conversion of *o*-H_2 in solid *p*-H_2 with an impurity.

In this research, the time dependence of the CH_3F-(*o*-H_2)$_n$ clusters is observed in order to discuss the nuclear spin microscopic conversion rate. The decay time of each peak corresponding to each cluster shows the change in the concentration of *o*-H_2 around the CH_3F-(*o*-H_2)$_n$ clusters. Therefore the nuclear spin conversion rate of *o*-H_2 around CH_3F could be discussed from these results. Furthermore, the both conversion processes; self-conversion of *o*-H_2 molecules, and catalyzed-conversion of *o*-H_2 with CH_3F, could be estimated separately.

In this chapter, the experimental results of the time dependence for cluster peaks are reported. In order to check the concentration dependence of *o*-H_2, two samples with different conditions are prepared. The nuclear spin conversion rates of *o*-H_2 with or without the existence of CH_3F are

estimated.

§ 3.2 Experimental details

The experimental setup is mentioned in Section 2.2.1. In this research, the grid polarizer to change the polarization of the laser beam is removed because it was not necessary. The time dependence of absorption spectrum of CH_3F-(o-H_2)$_n$ clusters are observed by keeping the sample below 2 K. Some effects to the clusters such as high power laser beam are avoided as much as possible. Each spectrum is measured at every one or two hours for 24 hours. In order to survey the dependence of the nuclear spin conversion rate on the o-H_2 concentration, the temporal behaviors in two different samples are observed. In the first sample, the concentration of o-H_2 and CH_3F are around 1000 ppm and 0.4 ppm, respectively. This sample is named the "dense sample" in this thesis. In the second sample, on the other hand, the concentration of o-H_2 and CH_3F are around 100 ppm and 1.0 ppm, respectively. This sample is named the "thin sample".

To keep the liquid He in cryostat, we refill the liquid He to the tank in cryostat with the interval of around 10 hours. During the refilling, the temperature of substrate for the sample is increased above 2 K for about 30 min. Thus, the observation for temporal behavior could be more difficult if the thermal energy affects the cluster structure. In order to check the effect of temperature difference to the sample, the temperature dependence is also observed. In order to observe the temperature dependence, the sample temperature is controlled by using the heater attached on the substrate and adjusted the exhaust volume with bulb in front of rotary pump. The temperature of the substrate is fluctuated within about ±0.3 K until it reaches the equilibrium temperature.

The experimental setup for pumping each peak is also the same. When we breached the target peak, the attenuator for decreasing the laser power was taken away. The probe laser is used with the attenuator to observe the spectrum.

§ 3.3 Results and analyses

3.3.1 The observation for the spectrum change in time

The absorbance spectra are shown in Fig. 3-1, in which n = 0 - 3 cluster's peaks are recorded at different times after 7 K annealing. The horizontal axis is absorbance and each spectrum is described

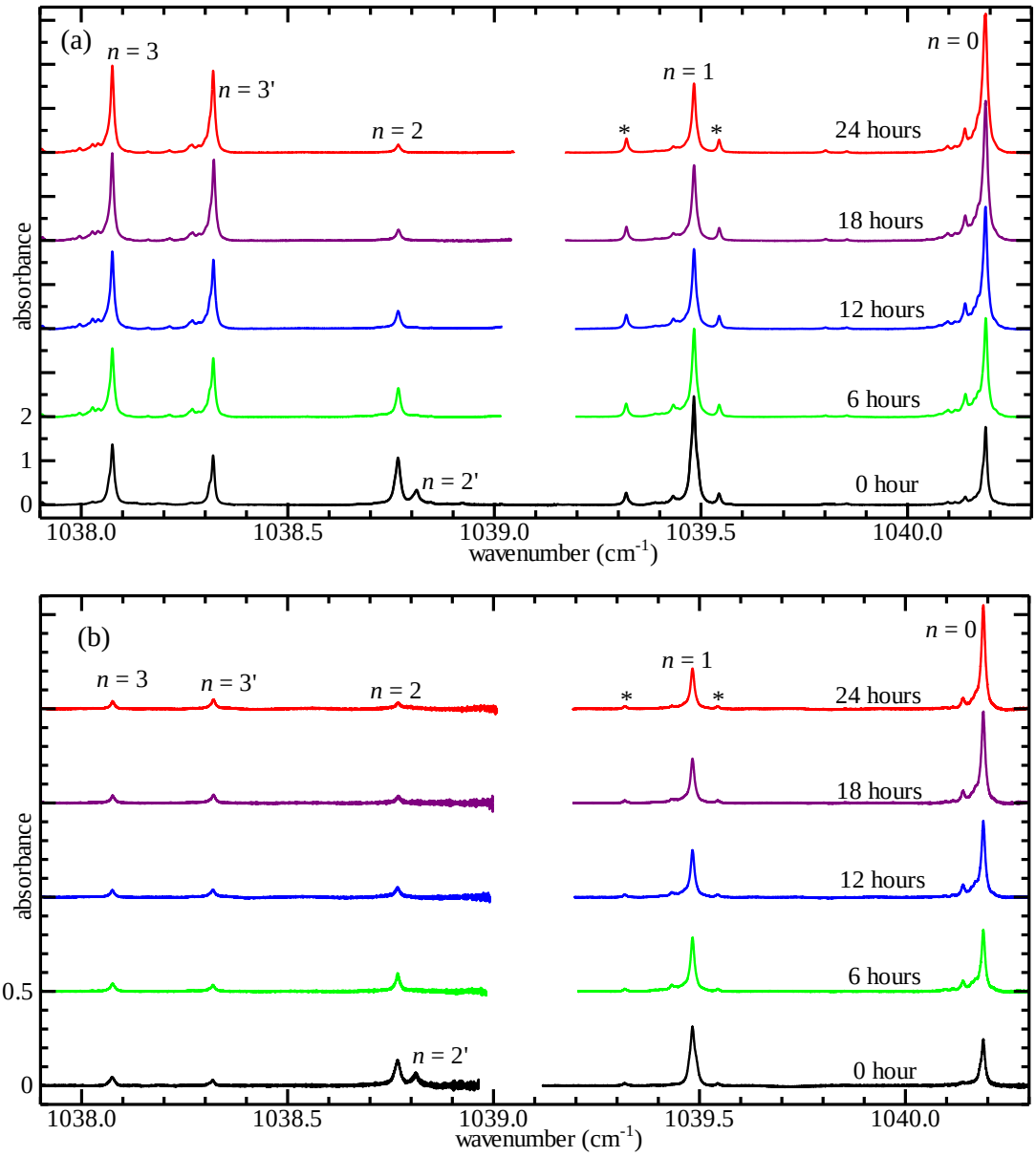

Fig. 3-1. The spectra of the ν_3 band of CH_3F-(o-H_2)$_n$ [n = 0, 1, 2, 3] measured for the dense sample (a) and the thin sample (b).

with 2 or 0.5 offset every 6 hours. The results for the dense and thin samples are shown in (a) and (b), respectively. The main series, labeled as n, corresponds to the spectrum peak series of CH_3F-(o-H_2)$_n$ clusters reported by Yoshioka and Anderson [52,53]. Each main peak has satellite peaks at the left (red) side and the satellite peaks show similar pattern with that reported by McKellar [57]. The n = 1 peak has two additional peaks at its both sides, as labeled with asterisks. The existences of these two peaks were reported in the previous study but their origins have not been revealed yet. However, their behaviors are different from the n = 1 main peak and also its satellite peaks. Therefore the two

peaks are not included in the satellite series of n = 1. The n = 3 main peak at 1038.075 cm^{-1} is accompanied with another strong peak at its right (blue) side (1038.318 cm^{-1}), as mentioned in Ref. 57. We name this unknown peak n = 3'. Another strong peak at the right side (1038.811 cm^{-1}) of the n = 2 peak, named n = 2', is also observed soon after 7 K annealing. However the peak decreased quickly and disappeared in several hours. This peak was also observed in a previous research [53].

It is known that the intensity distribution of these main peaks of CH_3F-(o-H_2)$_n$ clusters change in time [57]. In addition, the annealing changes the intensity distribution. Figure 3-2 shows the difference between before and after annealing. The result is for the dense sample. Before annealing, the intensity distribution of them follows the Poisson distribution since the numbers of o-H_2 molecules in each cluster with CH_3F are decided by the concentration of o-H_2 [66]. The 7 K annealing makes the crystal the single hcp structure since o-H_2 and p-H_2 can migrate easily by the thermal energy and change the crystal structure to more stable one; therefore, the linewidth of each peak becomes narrower. The distribution of o-H_2 might not be equal in the crystal and not follow the Poisson distribution completely since the electric interaction between CH_3F and o-H_2 can make o-H_2 come close to the CH_3F. This result is one of the evidences that CH_3F can make o-H_2 molecules come close to it. In this research, the initial distribution is defined at the situation soon after 7 K annealing (shown 0 hour in Fig. 3-1). The absorption intensities are different between the dense and thin samples. The thin sample has higher CH_3F concentration while the absorption is weaker than that of the dense one. The difference would be caused by the observed point, thus the thickness of the sample crystal at the observation points are different. The weak absorption intensities could cause to increase of the system error at analysis due to the bad S/N ratio but would not have any critical problems.

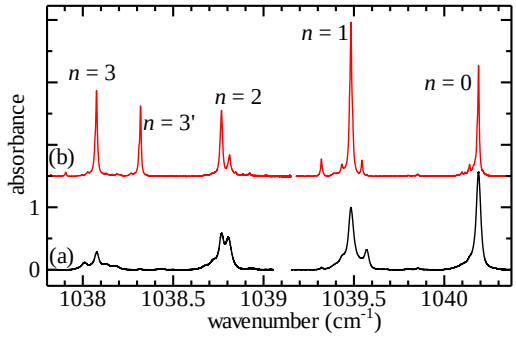

Fig. 3-2. The spectra of the ν_3 band of CH_3F-(o-H_2)$_n$ [n = 0, 1, 2, 3]. (a; black) before 7 K annealing. (b; red) after 7 K annealing.

The time dependence of integrated intensities of these peaks is shown in Fig. 3-3. It is easy to judge the time dependence. Each value in Fig. 3-3 includes not only the main peaks, but also the integrated intensity of satellite peaks and other unknown peaks observed very close to each main peak. The integrated ranges for n = 0, 1, 2 and 3 are 1040.05-1040.25 cm^{-1}, 1039.35-1039.53 cm^{-1}, 1038.70-1038.85 cm^{-1} and 1038.00-1038.40 cm^{-1}, respectively. The integrated intensities of n = 2 and 3 include the values of n = 2' and 3', respectively. The two peaks labeled with asterisks are not

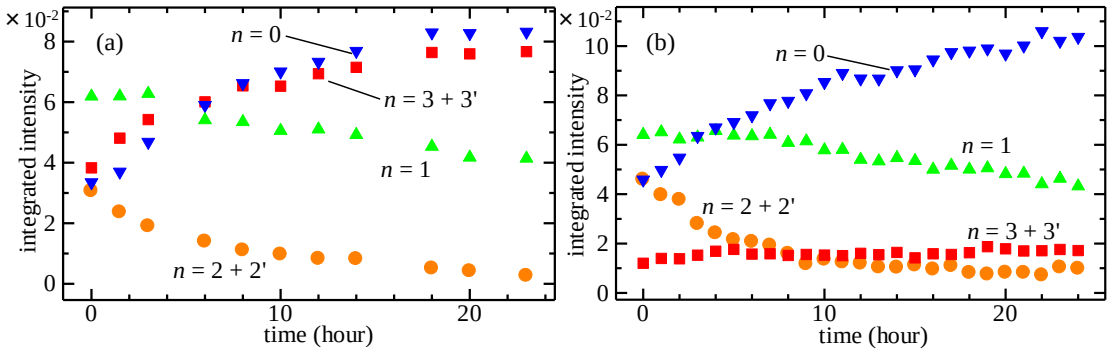

Fig. 3-3. The temporal behavior of the integrated intensities of each peak of CH_3F-(o-H_2)$_n$. (a) the result of the dense sample. (b) the result of the thin sample.

in n = 1.

The both experimental results show the intensities of n = 0 and 3 increase with time. On the other hand, the intensities of n = 1 and 2 decrease with time. The change in the intensity distribution of these peaks with time directly correlates to the change of the number of o-H_2 in its first nearest neighbor sites of CH_3F-(o-H_2)$_n$. There are two possible explanations for it: one is that o-H_2 is changed to p-H_2 by the nuclear spin conversion, and the other is that o-H_2 molecules are migrated to farther sites from CH_3F. The latter could happen due to the resonant *ortho-para* conversion [77], and that is called the migration or quantum diffusion [78]. However, the possibility that the o-H_2 in the first nearest neighbor site of CH_3F goes far away from CH_3F at 2 K might be very low since the electric interaction between CH_3F and o-H_2 is attractive. Furthermore, the satellite peaks are observed constantly for over 24 hours and the origins of them are the clusters formed with CH_3F and o-H_2 in its second-nearest neighbor sites, as discussed in Chap. 4. The fact would indicate that the migration of the o-H_2 in the second-nearest neighbor site to the first nearest neighbor is too little to observe it. Alternatively, the rates of migration of the o-H_2 between the first and second nearest neighbor sites of CH_3F are similar. From this result, the migration of the o-H_2 in the nearest neighbor sites of CH_3F is not the main mechanism of the cluster structural change. The temporal behavior of the CH_3F clusters with o-H_2 molecules would be mainly caused by the nuclear spin conversion of o-H_2 in its first nearest neighbor sites. The population of n = 3 increase at both samples. It would indicate that the population of $n \geq 4$ clusters are immigrated to the n = 3 by the nuclear spin conversion of o-H_2. Since the dense one accounts for a huge amount of the population of $n \geq 4$ clusters at the initial situation, the increasing ratio of n = 3 is high. On the other hand, the increase of the population of n = 3 are so small at the thin sample since the populations of $n \geq 4$ clusters are also small.

L. A-. Marguin and A. -M. Vasserot reported that the magnetic interaction between *o*-H_2 and CH_3F could induce the nuclear spin conversion and the rate would become faster than that without CH_3F [65]. Thus, the experimental results are explained that n = 2 cluster become n = 1, and n = 1 become n = 0 by conversion of the *o*-H_2 in the first nearest neighbor of each cluster. However, the temporal behavior of n = 3 cannot be explained by this theory. By following this theory, the intensity of n = 3 should decrease because it would be changed to n = 2 because one *o*-H_2 of n = 3 cluster is converted to *p*-H_2. This issue is discussed in Sec. 3.4.2.

3.3.2 The unknown peak that has different decay time

In order to check the temporal behavior of each satellite peak, Fig. 3-4 shows the satellite peaks of n = 0 and 1. These figures depict the results of the dense sample since it is easy to observe the satellite peaks than that of the thin one. Figure 3-4(a) describes that the intensity of satellite peaks around n = 0 (1040.04 - 1040.19 cm^{-1}) increases with time. On the other hand, that around n = 1 (1039.33 - 1039.48 cm^{-1}) decreases with time, as shown in Fig. 3-4(b). These behaviors are same with that of main peaks, as shown in Fig. 3-1(a). As described in Chap. 4, the satellite peak series are mainly composed of six peaks at both n = 0 and 1 main peaks, and the origin of them would be the CH_3F clusters formed with *o*-H_2 molecules in its second-nearest neighbor sites. The six satellite peaks are labeled by n' to compare with n main series. Therefore, it is convenient to identify those satellite peaks with a set of the number n and n' as (n, n'). One peak labeled with # in Fig. 3-4(a), however, is observed at the position between (0, 2) and (0, 3) peaks. Furthermore a similar peak is also observed at the position between (1, 2) and (1, 3) peaks as shown in Fig. 3-4(b). The temporal

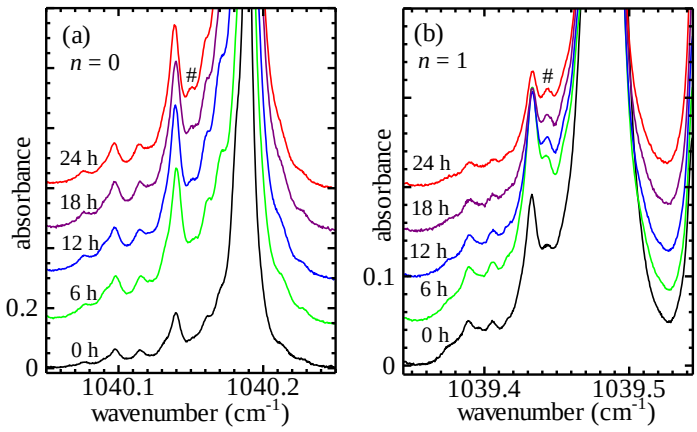

Fig. 3-4. The temporal behavior of satellite peaks in (a) n = 0 region and (b) n = 1 region. The black trace labeled 0 hour is observed soon after 7 K annealing. Each trace with labeled each time shows the spectrum at that time.

behavior of the # peak is different from other satellite peaks, as shown in Fig. 3-5. In this figure, the relative peak intensities to that of (1, 3) peak are plotted as the function of time. The relative intensities of (1, 4) and (1, 5) peaks to (1, 3) peak keep constant over the time, however that of the # peak rises over time. The temporal behavior of each peak might be determined by several physical dynamic processes such as the nuclear spin conversion between *o*-H_2 and *p*-H_2 and migration of *o*-H_2. Therefore the peaks marked with # are omitted from the satellite series in the analysis described in Chap. 4.

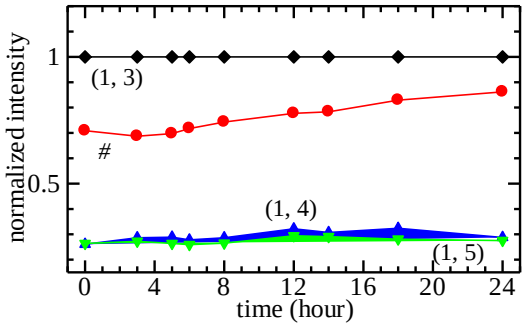

Fig. 3-5. The relative peak intensities to that of (1, 3) peak as the function of time. The # peak is different from others in the increasing ratio.

The origins of these peaks appeared at the right side of n = 2 and 3, in Fig. 3-1, also have been unknown. The temporal behaviors of them are completely opposite. The one at right side of n = 2, which is named n = 2', decreases with time. On the other hand, the peak at the right side of n = 3, which is named n = 3', increases with time. The intensity of n = 3' would become higher than that of n = 3 after a few tens hours [57]. These results are also observed in both of the dense and thin samples. The speed of change in the intensity distribution would depend on the sample conditions or the temperature. The temporal behavior of these unknown peaks would mean that the structure of n = 2' is more unstable than n = 2 at 2 K, and that of n = 3' is more stable than n = 3. After a few tens hours, the intensity distribution follows the pattern in Fig. 3-1, but when the temperature of the substrate is increased, the intensity distribution shows same pattern that is initial one soon after first 7 K annealing, as shown in Fig. 3-6. The spectra are not of the dense and thin samples. Similar results are observed for all sample, therefore this figure shows the clearest one observed to other sample. The trace (a) corresponds to the spectrum soon after 7 K annealing. The trace (b) was observed after 17 hours and the trace (c) was measured soon after re-annealing that was done soon after observing trace (b). The peak intensities for each trace are normalized because the intensity of trace (c) became weaker since some part of the sample crystal was sublimated by increasing the temperature. The relative intensity of n = 3 to n = 3' was changed and the n = 3 became stronger than n = 3' again. The peak of n = 2' appeared again. Thus, the relative intensities were almost returned to the initial spectrum, except that some points depend on the whole *o*-H_2 concentration in this sample, as shown at the relative intensities of n = 3 and 3' to others. Fig. 3-7 describes the temperature dependence of the satellite series of n = 0 and 1. Each spectrum in the figures is normalized since the intensity of each peak could be decreased by sublimation of the sample in the process of heating to 5

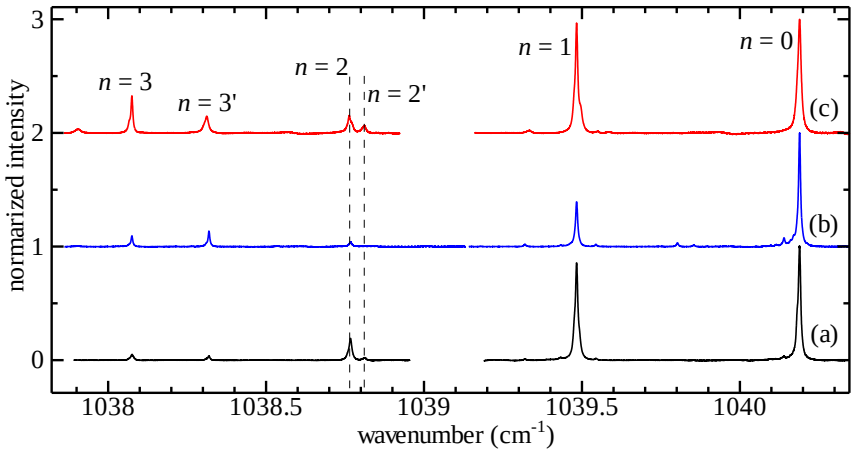

Fig. 3-6. The spectra of the ν_3 band of CH_3F-(o-H_2)$_n$ [n = 0, 1, 2, 3] measured by different situation. (a) observed soon after 7 K annealing. (b) observed the 17 hours later from 7 K annealing. (c) observed soon after re-annealing.

K. The main peak positions were shifted by about -0.0011 $cm^{-1}K^{-1}$ and -0.001 $cm^{-1}K^{-1}$ at n = 0 and 1, respectively [57]. It should be noted that the satellite peaks exists below 4 K while they are completely disappeared at 5 K at the same time. It would mean that the satellite series are originated from a common mechanism and the structures are broken at 4-5 K. The details are discussed at Section 4.3.6 in Chap. 4. Furthermore, the right shoulder at the n = 1 main peak was observed again. This peak was observed soon after 7 K annealing but disappeared within a several hours with keeping 2 K. This temperature dependence of the peak at the right side of n = 1 is very similar with n = 2'. In addition, the unknown peak observed at both sides of n = 1 labeled with asterisks were blue-shifted. It is clear that the origins of them are different from the satellite series although further studies are necessary to discuss the mechanism of the blue-shifting.

In order to survey the character of the n = 3 and 3' peaks, we observed the spectrum change by pumping each peak. The results of the pumping of each main peak are shown in Fig. 3-8. The black

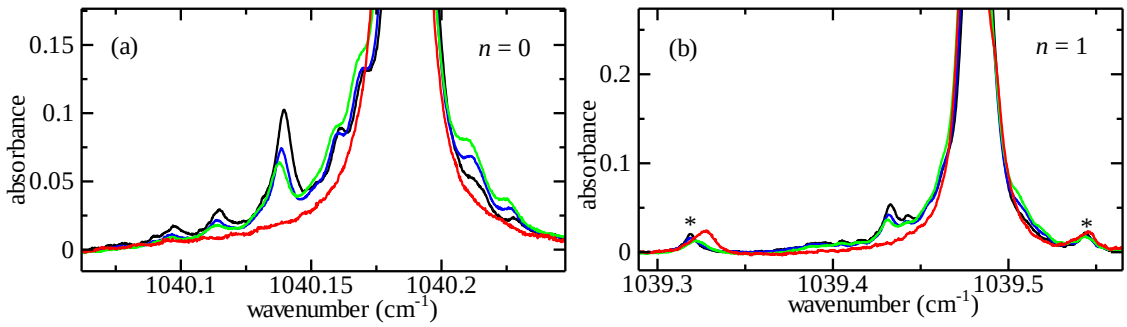

Fig. 3-7. The temperature dependence of the satellite peaks of (a) n = 0 and (b) n = 1. The trace colors show the spectrum at 2 K (black), 3 K (blue), 4 K (green), 5 K (red), respectively.

line shows the spectrum before the pumping and the red line shows that after the pumping. The period to keep irradiation of the pump beam is about 20 sec and the laser power is estimated around 2 mW. The n = 3 peak was almost disappeared after the pumping. On the other hand, the n = 3' peak was not completely bleached out by the pumping for 20 sec. Some peaks, labeled d = 3 and unknown peaks at the position between n = 3' and d = 3, and between d = 1 and n = 0 also changed their intensities. The d = 3 peak might be one peak that belongs to the series of d, and it is discussed in Chap. 6. However, the other peaks have not been assigned yet. It should be pointed out the intensities of n = 0 and 1 were almost constant through the pump experiment. Therefore, the population of the n = 3 and 3' cluster did not transfer to the cluster for n = 0 and 1.

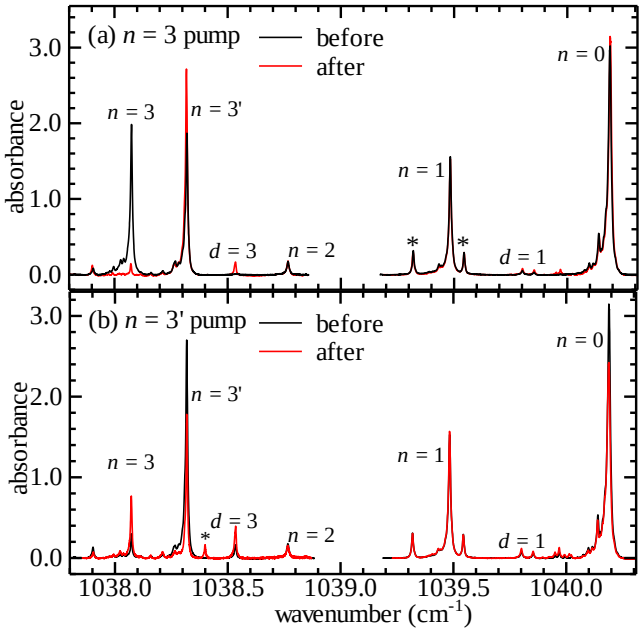

Fig. 3-8. The spectrum change by the pumping. (a) pumping of the n = 3 peak. (b) pumping of the n = 3' peak. The black and red traces show the spectrum before and after the pumping, respectively.

3.3.3 Fitting analysis

In order to estimate the nuclear spin conversion rate, we propose models for n = 0 - 2 and perform the fitting analysis with the rate equations for the experimental results. In general, comparing the molecular populations from the information of absorption intensities is difficult since the transition dipole moments are different with each cluster. In this research, however, all the peaks are responsible to the C-F stretching mode therefore it could be approximated that the effect of o-H_2 is small and the transition dipole moment for each cluster is similar with the ν_3 band of CH_3F.

Figure 3-9 shows the sum of each n peak's integrated intensity shown in Fig. 3-3. Figure 3-9(a) and (b) correspond to the results of the dense and thin samples, respectively. By linear least squares approximations to these results, the time dependence for the summed populations of the clusters approximately behave as below equations,

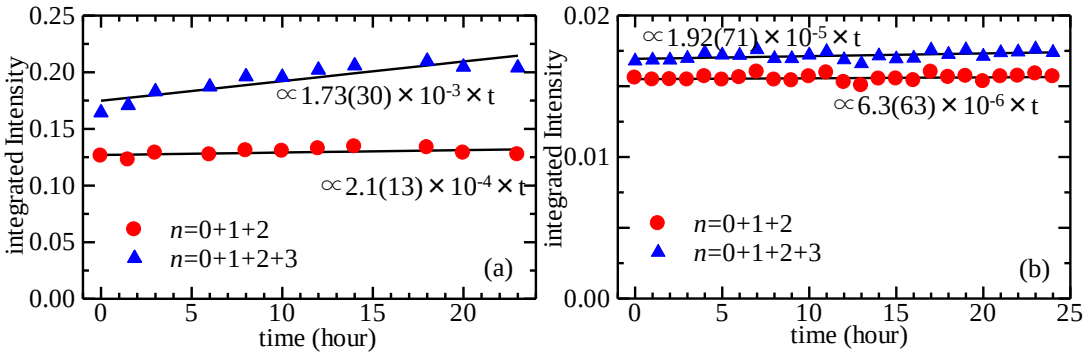

Fig. 3-9. The temporal behavior of the sum of the integrated intensities for each peak. The summed populations of n = 0 - 2 cluster peaks (red circle) and that of n = 0 - 3 cluster peaks (blue triangle). (a) at the dense sample. (b) at the thin sample.

$$
\begin{aligned}
&\text{The sum of } n = 0 - 2 \text{ for the dense}: 1.27(2)\times10^{-1} + 2.1(13)\times10^{-4}\times t \quad \text{[h]} \\
&\text{The sum of } n = 0 - 3 \text{ for the dense}: 1.78(4)\times10^{-1} + 1.73(30)\times10^{-3}\times t \quad \text{[h]} \\
&\text{The sum of } n = 0 - 2 \text{ for the thin}: 1.55(1)\times10^{-2} + 6.3(63)\times10^{-6}\times t \quad \text{[h]} \\
&\text{The sum of } n = 0 - 3 \text{ for the thin}: 1.69(1)\times10^{-2} + 1.92(71)\times10^{-5}\times t \quad \text{[h]}
\end{aligned}
\qquad (3-1)
$$

The estimations are based on the assumption that the absorption integrated intensities relate to the population of each cluster. The result indicates that the sum of the population of n = 0 - 3 increased by 23(4)% after 24 hours from 7 K annealing in the dense sample. On the other hand, that for the thin sample did not increase so much. The increase in the population was 3(1)% after 24 hours. The increase in the population of the sum of n = 0 - 3 clusters is appeared because the population of $n \geq 4$ clusters became the n = 3 cluster by converting their *o*-H_2 molecules. The absorption peaks of $n \geq 4$ clusters are outside for the range of QCL, therefore we are not able to discuss the temporal behavior of $n \geq 4$ clusters. But the existence of $n \geq 4$ clusters was checked in the previous studies [52,57], and the assumption could be possible. The difference between these samples was due to the difference of the initial population of $n \geq 4$ clusters. The populations for the sum of n = 0 - 2 are nearly unchanged with time in both samples. It was only changed by 4(2)% after 24 hours for the dense sample, and the thin sample had constant value for the population of n = 0 - 2. The phenomenon that the immigration of the population from n = 3 to n = 2 were not clearly observed in both samples. From these results, the sum of the population of n = 0 - 3 clusters cannot be treated as constant, but that of n = 0 - 2 clusters can be treated as constant. One possible mechanism is that the formation of n = 3 cluster has the magic number and the rate of the nuclear spin conversion of *o*-H_2 in it is dramatically suppressed, as it can be treated like a dam for the population. The detail of this mechanism is

discussed in Sec. 3.4.3. We construct the rate equation to this temporal behavior for the population of n = 0 - 2 and we estimate each nuclear spin conversion rates by self-conversion and catalyzed-conversion separately.

In this study, the mechanisms of the interactions, such as spin-spin interaction or rotation spin interaction, are not discussed, but the types of the conversion are discussed. One type is self-conversion (*SC*), which is caused by the interaction between *o*-H_2 molecules. The other is catalyzed-conversion (*CC*), which is caused by the interaction between *o*-H_2 and CH_3F. The population change by migration of *o*-H_2 to further site from the first nearest neighbor site of CH_3F is ignored, as mentioned above. Therefore the estimation of the decay time for each cluster only relates to the nuclear spin conversion of *o*-H_2. In fact, the interaction between *o*-H_2 in the first nearest neighbor site of CH_3F and *o*-H_2 in the second-nearest neighbor site of that would be possible. However, it is very complicated to treat the pair of *o*-H_2 molecules in the first and second nearest neighbors. In this analysis, the effect of *o*-H_2 molecules in the second-nearest neighbor sites of CH_3F is neglected. Based on these approximations, the nuclear spin conversion rate to n = 0 - 2 clusters are estimated. The relaxation model for the conversion from n = 2 to n = 0 is depicted in Fig. 3-10. Since the n = 2 cluster consists of two *o*-H_2 molecules and one CH_3F, the self-conversion could be happened and the catalyzed-conversion could also be occurred to both *o*-H_2 molecules. Since the electrical interaction between both *o*-H_2 molecules might form the pair of *o*-H_2 in the n = 2 cluster, the existence of non-pair of *o*-H_2 is neglected. The n = 1 cluster consists of one *o*-H_2 and one CH_3F, therefore the nuclear spin conversion is only occurred by catalyzed-conversion. For simplicity, the populations of n = 2, 1 and 0 are expressed as A, B, and C, respectively. The rate equations are expressed as

$$\frac{dA}{dt} = -\left(\frac{1}{\tau_{SC}} + \frac{2}{\tau_{CC}}\right) A, \frac{dB}{dt} = \left(\frac{1}{\tau_{SC}} + \frac{2}{\tau_{CC}}\right) A - \frac{1}{\tau_{CC}} B, \frac{dC}{dt} = \frac{1}{\tau_{CC}} B \qquad (3-2)$$

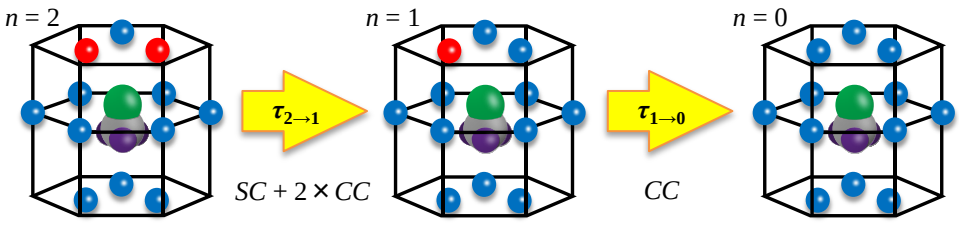

Fig. 3-10. The image of CH_3F-(*o*-H_2)$_n$ [n = 0, 1, 2] clusters. The red spheres indicate *o*-H_2 and blue spheres show *p*-H_2. The decay times relate to the self-conversion (*SC*) and catalyzed-conversion (*CC*).

The boundary condition is

$$N = A(t) + B(t) + C(t) \qquad (3-3)$$

The solutions for these differential equations can be written as

$$A(t) = A_0 \exp\left[-\left(\frac{1}{\tau_{SC}} + \frac{2}{\tau_{CC}}\right)t\right]$$

$$B(t) = -\frac{\tau_{CC} + 2\tau_{SC}}{\tau_{CC} + \tau_{SC}} A_0 \exp\left[-\left(\frac{1}{\tau_{SC}} + \frac{2}{\tau_{CC}}\right)t\right] + B_0 \exp\left(-\frac{t}{\tau_{CC}}\right) \qquad (3-4)$$

$$C(t) = N + \frac{\tau_{SC}}{\tau_{CC} + \tau_{SC}} A_0 \exp\left[-\left(\frac{1}{\tau_{SC}} + \frac{2}{\tau_{CC}}\right)t\right] - B_0 \exp\left(-\frac{t}{\tau_{CC}}\right)$$

where A_0 shows the initial value of A (n = 2) and B_0 is the coefficient for B.

The fitting result to the thin sample is depicted in Fig. 3-11. The estimated values in Eq. (3-4) for the both samples are summarized in Table 3-1. The fitting analysis is done both for the dense and thin samples, and also we tried to do the simultaneous fitting to the both results with the same τ values.

The estimated decay time of self-conversion has large uncertainty. It would indicate some assumptions that the o-H_2 molecules in an n = 2 cluster make a pair and the effect of o-H_2 in the second-nearest neighbor can be ignored would be too rough. In addition to them, the phenomenon of the migration of o-H_2 is ignored. Furthermore, the amount of the data points for the dense sample is not enough for this fitting analysis. The determined decay time by

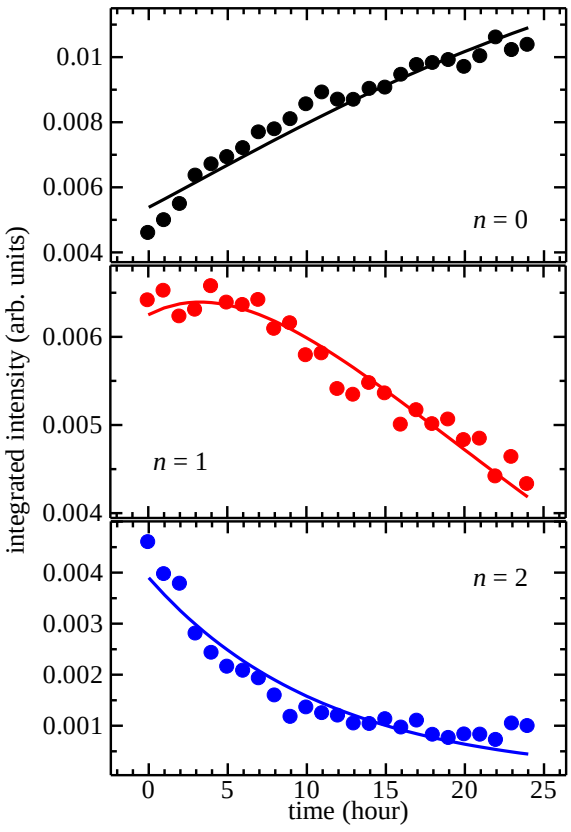

Fig. 3-11. The temporal behavior of the integrated intensities of CH_3F-(o-H_2)$_n$ clusters. Each point is experimental result and the traces are fitting results with Eq. (3-4).

Table 3-1. The estimated fitting parameters of the nuclear spin conversion rate of *o*-H_2 at the n = 2 and 1 clusters by self-conversion (τ_{SC}) and catalyzed-conversion (τ_{CC})

	dense	*thin*	Simultaneous	
			dense	thin
A_0	$2.78(20)\times10^{-2}$	$3.90(15)\times10^{-3}$	$2.78(11)\times10^{-2}$	$4.06(64)\times10^{-3}$
B	$1.12(6)\times10^{-1}$	$1.34(4)\times10^{-2}$	$1.12(3)\times10^{-1}$	$1.34(10)\times10^{-2}$
N	$1.29(2)\times10^{-1}$	$1.55(1)\times10^{-2}$	$1.29(1)\times10^{-1}$	$1.55(6)\times10^{-2}$
τ_{CC} (*h*)	23.2(13)	24.4(8)	23.2(7)	
τ_{SC} (*h*)	86(98)	121(82)	87(51)	

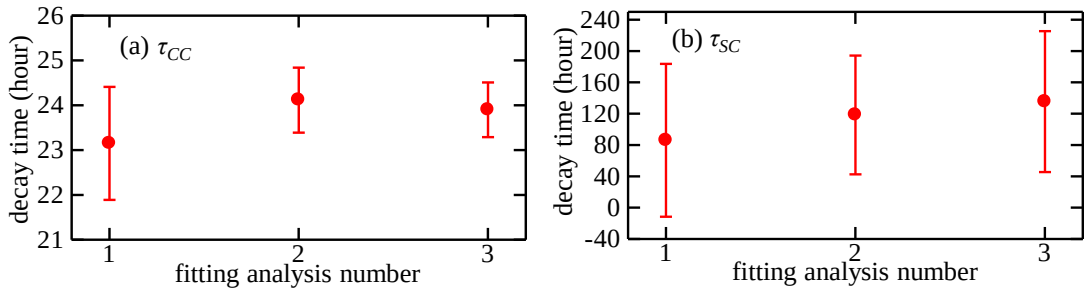

Fig. 3-12. The estimated decay time of (a) catalyzed-conversion and (b) self-conversion. The horizontal axis shows the fitting analysis number. 1, 2, and 3 show the result to the dense sample, to the thin sample, and the simultaneous, respectively.

self-conversion and catalyzed-conversion are shown in Fig. 3-12. Each value by the different analysis describes that the common value within each error-bar that shows 1σ statistical error. Thus, the concentration of *o*-H_2 and CH_3F in the sample crystal would not affect the conversion rate of *o*-H_2 in the cluster with CH_3F. The difference of the concentration would only appear to the peak intensity distribution.

3.3.4 Fitting analysis to n = 4

The sum of the population for n = 0 - 3 clusters increased since the population of $n \geq 4$ clusters were changed to n = 3 by the nuclear spin conversion of *o*-H_2. The rate could be estimated with a supposition that *o*-H_2 in n = 3 was not converted. If the increase in the population of n = 3 nearly equals to the decrease of the population of n = 4, the population change of n = 4 could be analyzed by fitting. Figure 3-13 depicts the cluster model for n = 4. The catalyzed-conversion process can be easily estimated since the number of *o*-H_2 in the first nearest neighbor sites is 4. On the other hand,

the number of possible formation for the *o*-H_2 molecules in the first nearest neighbor sites is variable.

The minimum number is 1, as described in Fig. 3-13, and the maximum is 5. Following the fitting analysis for the population change of n = 0 - 2 clusters, fitting of the population change for n = 4 clusters is attempted with the estimated τ value shown in Table 3-1. In order to estimate the number of *o*-H_2 pairs, one parameter for it is added, as C_{SC}. The fitting function becomes

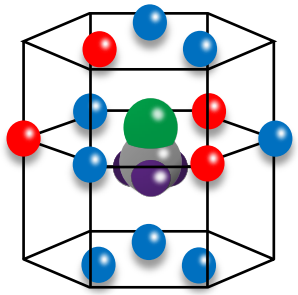

Fig. 3-13. One example of the image of CH_3F-(*o*-H_2)$_4$ cluster. The red and blue H_2 molecules show *o*-H_2 and *p*-H_2, respectively.

$$D(t) = D_{offset} + D_0 \exp\left[-\left(\frac{C_{SC}}{\tau_{SC}} + \frac{4}{\tau_{CC}}\right)t\right] \qquad (3-5)$$

The values of τ_{CC} and τ_{SC} are fixed to 24.4 and 121, respectively. D_{offset} is a coefficient for the offset of the population since the population of n = 4 at 24 hours could not be estimated and is set to be 0, as shown in Fig. 3-14. Figure 3-14 shows the temporal behavior for the estimated population of n = 4 in the dense sample. These dots correspond to the experimental result and the black line shows the fitting result where that C_{SC} is fixed to 1. The result of the thin sample does not have enough S/N ratio for this fitting analysis since the increase in the population of n = 3 from n = 4 does not have enough amount. The C_{SC} was estimated -5(2) by the fitting analysis. It would mean that this model is not good for this experimental result. The reason why the fitting analysis is not successful would be because the estimated population of n = 4 includes other populations than n = 4. As mentioned above, the immigrated population to n = 3 is not only from n = 4 cluster, but also $n \geq 5$ clusters. Thus, for the accurate fitting analysis, the peaks of $n \geq 4$ clusters should be observed. If the C_{SC} value is changed, the curvature of the fitting line is not dramatically changed. Thus, we cannot estimate the number of the *o*-H_2 pairs in the first nearest sites of n = 4 clusters from this analysis.

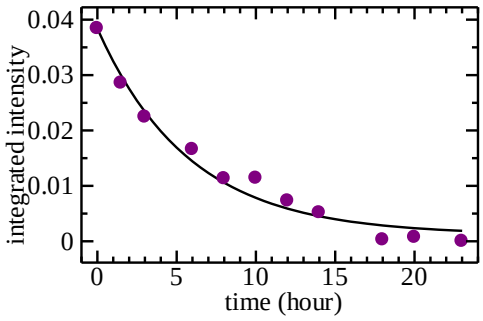

Fig. 3-14. The assuming temporal behavior of the integrated intensity of n = 4. Each point describes the experimental result that is estimated from the increase in the population of the n = 3 peak. The trace shows the fitting analysis result by using Eq. (3-5) with τ that is fixed to the value in Table 3-1.

§ 3.4 Discussion

3.4.1 The nuclear spin self-conversion rate

As mentioned above, the nuclear spin conversion rate of *o*-H_2 by itself is almost forbidden at the gas phase. At solid state, the rate is also very small without any paramagnetic catalysts and it depends on the concentration of *o*-H_2 in it. If the concentration of *o*-H_2 is below 1%, the concentration has been observed constant over periods in the order of weeks [5]. For over 20%, the concentration change follows to the rate equation

$$\begin{aligned} C &= -kC^2 \\ \frac{1}{C(t)} &= kt + \frac{1}{C(0)} \end{aligned} \qquad (3-6)$$

where C is the concentration of *o*-H_2 and k that is the reaction rate is about 50 h^{-1}. The conversion rate is about 2 %/h in pure *o*-H_2 crystal [4]. The value is a little different from our result. The reason is that the point of measurement is different. They determined the spin conversion rate from the observation result of $S_0(1)$ signal that attributes to *o*-H_2. Therefore, the decay time was determined from sum of all *o*-H_2 in the whole solid hydrogen. The previous studies are classified with the macroscopic group, as mentioned in Sec. 3.1. On the other hand, the decay time is determined in this research from the observation for the change of the absorption peaks of CH_3F-(*o*-H_2)$_n$ clusters with time. Thus, this research mainly discusses the spin conversion rate of *o*-H_2 with another one *o*-H_2 molecule.

S. Washburn *et al.* researched the nuclear spin conversion rate by observing the signal change in time of single *o*-H_2 and pair *o*-H_2 by using NMR [5]. They observed the temporal behaviors of the absorption signals for out-of-plane and in-plane pairs of *o*-H_2 and determined the characteristic decay times of them. Their analysis had one problem, which was mentioned by themselves, that the decay time of the pair signals included the decay time for forming larger clusters. Thus, the pair signal is disappeared when the pair becomes one new cluster with other *o*-H_2 molecules. From this prospect, the true decay time of the nuclear spin conversion rate of the *o*-H_2 pair would be longer than they estimated. Their results, the decay times of out-of-plane and in-plane pair are over 50 hours and 20±5 hours at 0.36 K, respectively. In our experiments, the estimated value is around 100(50) hours and it is a little longer than previous one. It cannot be judged which kind of the formation occurred for *o*-H_2 pair in each cluster, out-of-plane or in-plane one. However, the value

they estimated could be longer by ignoring the time for forming large cluster of *o*-H_2.

3.4.2 The nuclear spin catalyzed-conversion rate

The estimated value of τ_{CC} is the catalyzed nuclear spin conversion rate of *o*-H_2 by CH_3F. The catalyzed-conversion rate of *o*-H_2 in solid H_2 with dopant other molecules has been investigated for some molecules [13,15,65,79]. These researches determined the conversion rate of *o*-H_2 at each experimental condition. From the group theory, CH_3F belongs to the C_{3v} point group and the nuclear spin statistics is determined. CH_3F has total hydrogen nuclear spin I = 3/2 and 1/3 when the rotational quantum number K is 0 modulo 3 and the K is not 0 modulo 3, respectively. Thus, at low temperature, CH_3F has only K = 0 with I = 3/2 (*ortho*) and K = 1 with I = 1/2 (*para*). CH_3F has always the non-zero nuclear functions. L. Abouaf-Marguin *et al.* reported the nuclear spin conversion rate of *o*-H_2 with CH_3F molecule in solid normal H_2 [16]. From their result, CH_3F affects the nuclear spin conversion rate of *o*-H_2 and the rate at their experimental environment was determined. The condition was different from our experiment. The lattice constant for solid *p*-H_2 was reported 3.77-3.789 Å depending on the concentration of *o*-H_2 [17]. Thus, the lattice constant of solid normal H_2 could be estimated around 3.77 Å. In Ref. 16, they used normal H_2 to make sample crystal and the concentration of CH_3F was 1/4000 = CH_3F/H_2, thus much higher than ours. The conversion rate they determined from their experimental result was 0.208(8) min^{-1} without migration time of *o*-H_2. Thus, the τ they estimated was about 5 min and that in this research is 24.4(8) hours. The value they estimated was much shorter than ours. The difference would be caused by mainly two causes. One is that the ratio of *o*-H_2 to CH_3F. In this research, the ratios of 1:1 or 1:2 for CH_3F vs *o*-H_2 in its first nearest neighbor sites are discussed. On the other hand, the previous study discussed the situation where CH_3F vs *o*-H_2 was almost 1:12. Therefore it's too difficult to discuss the effect of CH_3F on one *o*-H_2 from their result. From these points of view, this research is the first time to discuss the pure effect of CH_3F on the nuclear spin conversion rate of one *o*-H_2 in solid *p*-H_2. However, even if the situation they estimated was CH_3F:*o*-H_2 = 1:12, the decay time was too short than our result. Their decay time should be 1/12 times of ours if the CH_3F has 12 *o*-H_2 molecules in its first nearest neighbor sites, thus the decay time should be 2 hours from our estimation. The other reason is that CH_3F can make *o*-H_2 molecules close to it by electric interaction. The evidence of this phenomenon could be observed through the intensities distribution change induced by annealing, as seen in Fig. 3-2. CH_3F contributes to the nuclear spin conversion of *o*-H_2 not only by the catalyzed-conversion, but also by accelerating the self-conversion of *o*-H_2 molecules around it.

However, in the previous research, the catalyzed-conversion rate was determined with the fixed self-conversion rate that was determined at the sample without CH_3F. Thus, the catalyzed-conversion rate they estimated could be included the conversion rate by self-conversion.

Furthermore, the difference could be caused by the difference of the interaction distances between each molecule. The decay time is absolutely depends the distance of the molecules [79]. The twelve *o*-H_2 molecules in first nearest neighbor sites of CH_3F would change the crystal structure. The spectrum of CH_3F-(*o*-H_2)$_{12}$ cluster shows very broad peak, as shown in Fig. 2 in Ref. 53. The nuclear spin conversion rate by magnetic interaction is inversely proportional to the cubed of the distance between molecules. Thus the distance of the *o*-H_2 around CH_3F of high *n*-th clusters would be closer and the intensity of magnetic interaction becomes larger than that of the one *o*-H_2 and CH_3F. These would cause the difference between the previous research and this study.

3.4.3 The temporal behavior of *n* = 3 peak

The nuclear spin conversion rate of the n = 3 cluster is much slower than others. As discussed above, one possibility of this mechanism is that the n = 3 cluster has a magic number and the rate of nuclear spin conversion dramatically suppressed. The magic number, however, is difficult to be explained. For example, the meaning of the “magic number” for the cluster with OCS and He [80] is that the character of the cluster is dramatically changed at that number. They discussed the threshold of the superfluid but even if the number of He is over the threshold, the phenomenon is still kept. However, in our experimental case, we discuss the nuclear spin conversion rate and it depends on the strength of the magnetic interactions. Therefore, it is not easy to believe that three *o*-H_2 molecules and one CH_3F form a characteristic cluster and the interactions among these molecules become so weak. Furthermore, the population of n = 4 clusters decreased as well as n = 2. The fact can be checked by observing the increase of peak intensity at n = 3 with time.

One possibility for the magic number is that the three *o*-H_2 in the n = 3 cluster are not adjacent to each other. The self-conversion process would have not happened. The image of this cluster is shown in Fig. 3-15. CH_3F is a symmetric-top rotor with the C_{3v} symmetry. The most stable formation of one CH_3F and three *o*-H_2 molecules would keep the C_{3v} symmetry and thereby three *o*-H_2 molecules form an equilateral triangle around CH_3F. If the three *o*-H_2 stay at the body plane of CH_3F, there are six nearest sites, and

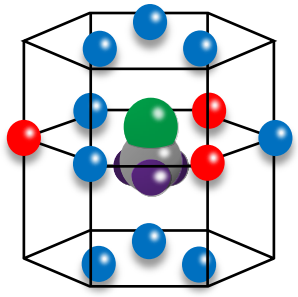

Fig. 3-15. One possible structure of the n = 3 cluster.

they cannot be adjacent to each other. Even if following the cluster model, the catalyzed-conversion process, however, has to occur. Therefore, the nuclear spin conversion rate of $n = 3$ cluster should be close to the value of $3/\tau_{CC}$ but the experimental result was not so.

Another possibility is that the conversion rate of *o*-H_2 is dramatically changed by their relative position toward the CH_3F. The conversion rates are changed by the formations of out-of-plane or in-plane *o*-H_2 pair [5], as discussed above. It is determined by the effect of the crystal field in *p*-H_2 whether the *o*-H_2 pair becomes out-of-plane or in-plane. In this situation, the CH_3F has the dipole moment that is much larger than the crystal field. Therefore, the nuclear spin conversion rate of *o*-H_2 around CH_3F would be different where the *o*-H_2 stays close to the CH_3F.

As another possibility is that the *o*-H_2 molecules in the second nearest neighbor sites can migrate to first nearest sites. The observed spectrum looks like the phenomenon that the change of the $n = 3$ clusters to the $n = 2$ clusters is not happened. However, if the rate of immigration from $n = 2$ to $n = 3$ is very fast and that of the opposite one is late, the phenomenon could be explained. The cluster change from $n = 2$ to $n = 3$ is happened since the *o*-H_2 in the far site comes to the first nearest neighbor site. The opposite change is happened due to the nuclear spin conversion of *o*-H_2 in the first nearest neighbor site of $n = 3$ cluster. Even if the latter one has a same value with estimated τ_{CC} and τ_{CC}, the change cannot be observed when the rate of former one is so fast. In fact, the absorbance spectrum at the 24 hours still has $n = 2$ peak. Therefore, the spectrum would indicate the nearly equilibrium state for the immigration rates between $n = 2$ and $n = 3$. The migration rate of *o*-H_2 from far site to the first nearest site could be changed by the number of *o*-H_2 molecules in the first nearest neighbor sites; therefore, the temporal behavior of each cluster would be different. The rates of migration of *o*-H_2 between each cluster, however, are not able to be estimated by the fitting analysis since the parameters are too much. The theoretical calculation about the rate for the migration of *o*-H_2 is necessary to determine the parameters for understanding the detail of the phenomenon at local structure around CH_3F.

3.4.4 The origins of *n* = 3’ and 2’ peaks

The origin of the $n = 3$’ peak has not been proved yet. One assumption for it is the absorption peak from CH_3F in the face-centered cubic (fcc) structure of solid *p*-H_2. It is well known that solid *p*-H_2 form the hexagonal closed-packed (hcp) structure at low temperature and at low concentration of *o*-H_2. N. S. Sullivan *et al.* reported the threshold of transformation from hcp to fcc, and the figure summarizing the results is shown in Fig. 3-16 [81,82]. The *p*-H_2 crystal forms fcc when the

concentration of *o*-H_2 is around 85% at 2 K, which is the same temperature as in our experimental condition. The concentration is much higher than that in our experiment. However, at the microscopic, the concentration around n = 3 clusters is very high and CH_3F molecules could affect the environment. Assuming that the environment around n = 3 cluster is near the situation that the concentration of *o*-H_2 is higher than 85% in H_2 crystal without CH_3F, the structure of solid *p*-H_2 around n = 3 cluster temporarily becomes the hcp structure by 7 K annealing. The structure would transform to fcc from hcp slowly while keeping at 2 K. This hypothesis could explain the experimental result that the relative intensities changed from n = 3 to n = 3'. Furthermore, it could explain the temperature dependence that the relative intensity of n = 3 became stronger than n = 3' again when the sample temperature returned above 5 K, as shown in Fig. 3-6. In addition, the n = 3' peak was disappeared when the temperature of the sample was kept at 4 K for 1 hour and 3 K for 1 hour, as shown in Fig. 3-17. In this figure, the spectra are taken from different samples therefore the S/N of trace (a) is worse than trace (b). Following this theory, the origin of some peaks at n = 4 are also from fcc structure and the temporal behavior of them would look like n = 3', thus these peaks increase with time. In order to assign the peaks of n = 4 clusters, the spectra change in figure 11 of Ref. 57 were checked. However, it is very difficult since all n = 4 peaks decrease with time because of the immigration to n = 3 clusters.

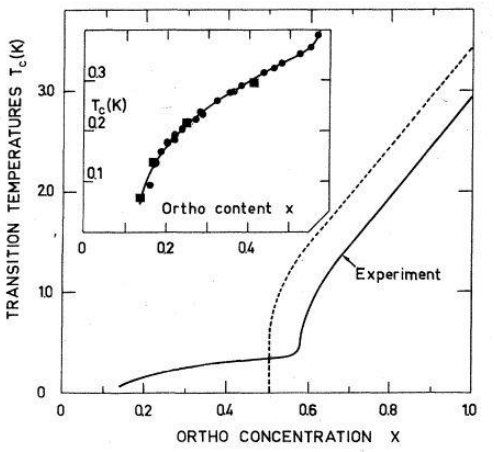

FIG. 1. Phase diagram of solid ortho–para–hydrogen mixtures. The solid lines indicate the transition hydrogen–temperatures $T_c(X)$ deduced from the NMR studies as described in the text. The broken line represents the critical temperatures calculated in Reference (12) for $X > 0.5$. The inset shows the glass phase transitions on an expanded scale. The solid circles are taken from this work and Ref. 8, and the solid squares are from Ref. 16.

Fig. 3-16. The phase diagram of solid hydrogen. This figure is referred from the reference 81.

The pump experimental results would also support this hypothesis. As seen in Fig. 3-8, n = 3 was disappeared and n = 3' was not disappeared by pumping for 20 sec on each peak. It would indicate that the n = 3' cluster was more stable than n

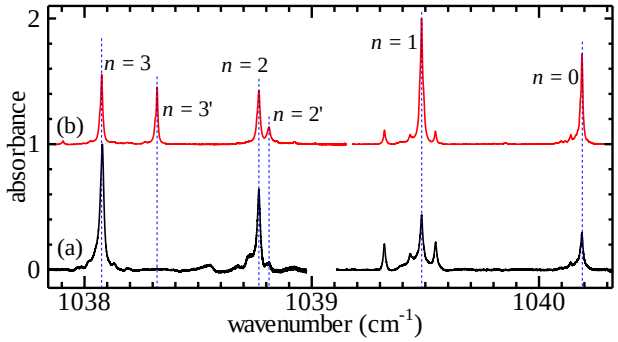

Fig. 3-17. The comparison of spectra. Trace (a); after 4 K for 1 hour and 3 K for 1 hour. Trace (b); after 7 K annealing. Two spectra are from different samples.

= 3 and it is easier to transform the crystal structure between fcc and hcp than to migrate for the *o*-H_2 in *n* = 3 and 3' clusters from first nearest site to far site. The thermal energy that the crystal gets from the vibrational energy of CH_3F could change the structure of the crystal. However, the thermal diffusion would be so fast that it would not be easy for the crystal structure to change from fcc to hcp. Therefore, the decay of *n* = 3' by the pumping was slower than that of *n* = 3. Following this assumption, the fcc structure is more stable around CH_3F-(*o*-H_2)$_3$ therefore the pump beam would be one trigger to transform the crystal structure from hcp to fcc. If this phenomenon really happens, it could be a very interesting topic since the crystal structure change by laser irradiation could be observed. We hope to continue the survey and elucidate it experimentally.

The peak of *n* = 2' cannot be explain by the same theory for *n* = 3'. Their behaviors to temperature were definitely opposite. The *n* = 2' peak appears above 5 K and disappears under 5 K in a few hours. Therefore, the mechanisms for the appearance of *n* = 2' and 3' would be different. The unknown peak at the right shoulder of *n* = 1, discussed in Ref. 57, also has the same origin as *n* = 2'. The mechanism has not been identified yet.

§ 3.5 Conclusion

This research investigated that the nuclear spin conversion rate of *o*-H_2 molecules in the first nearest neighbor site of CH_3F by observing the temporal behavior of the spectrum for the clusters with CH_3F and *o*-H_2 molecules. The estimated self-conversion rate has large uncertainty, and the value is the same order with the previous study [5]. The catalyzed-conversion rate is also estimated by the fitting analysis. The decay time is 24.4(8) hours and it is longer than that in the previous study [16]. The main cause of the inconsistency would be the difference of the experimental ways. The estimated catalyzed-conversion rate in this research is caused by the interaction between one CH_3F and one *o*-H_2 molecule. On the other hand, the previous studies researched it from the concentration of *o*-H_2 in solid *p*-H_2. It means that they did not discuss the interaction between one CH_3F and one *o*-H_2. Therefore, the value is clearly different from the previous research and this is the first time to estimate the catalyzed-conversion rate from microscopic study. From this research, we found that the catalyzed-conversion rate of *o*-H_2 by CH_3F is faster than the self-conversion rate, but the difference between them are not so large. By comparing the previous research and this one, the effect of CH_3F is not only to do the catalyzed-conversion, but also to accelerate the self-conversion since CH_3F can make *o*-H_2 molecules come close to it.

This research could contribute not only to the knowledge for the system of CH_3F in solid *p*-H_2, but also the development of the detailed physical implications of nuclear spin conversion of *o*-H_2 with dopant in the solid *p*-H_2. However, this research has not been complicated. In order to analyze more detail, we should observe the temporal behavior of absorption peaks of $n \geq 4$ clusters. By the experiment, we could identify the phenomenon that happens in the $n = 3$ peak.

The origin of the $n = 3$' peak would be the signal from CH_3F in the fcc structure of *p*-H_2 crystal. Still now, there are some issues such as the origins of $n = 2$' and #, and the mechanism of the nuclear spin conversion at $n = 3$ cluster. This would be main issue of this research from now on.

Chapter 4 The origins of satellite peaks

§ 4.1 Introduction

By using QCL with high-resolution spectroscopy, we can resolve and identify the *ortho*-CH_3F (J = 0, K = 0) and *para*-CH_3F (J = 1, K = 1) components separately in a single shouldered peak, in spite of the $\Delta K = 0$ selection rule of the parallel band transition [57]. The spectral shape is shown in Fig. 3 in Ref. 57. In addition, many weak peaks were observed at the red (lower energy) side of the main peaks forming the regular n series, as mentioned in Chap. 3. These were considered to be "satellite" peaks somehow related to the CH_3F clusters, but no detailed explanation or analysis of them was given. In the previous studies, this kind of structures was observed and analyzed for some molecules like CO_2 [35] and HF [83].

In this chapter, the details of these satellite peaks associated with the main series of the ν_3 band by using the high sensitivity of the QC laser absorption spectroscopy are reported. In order to understand the photochemical dynamics of the CH_3F-(o-H_2)$_n$ clusters, the assignment of the satellite peak is indispensable, because each main peak has a particular relationship with some certain satellite peaks through the photochromic phenomenon [57].

In addition to that, the character of satellite series when bleached by laser beam is investigated. By irradiating on each peak at about 10 mW, the peak decreases and other peaks increase. In order to check the origin of satellite peak from other point of view, we try to bleach each satellite peak and discuss it. Furthermore, we observed the temperature dependence to the satellite series, as we introduced in Chap. 3.

Most parts of this chapter are the same experimental results and discussions that we published in Ref. 61.

§ 4.2 Experimental details

The experimental setup is mentioned in Sec. 2.3. In this research, the grid polarizer is also moved out in order to change the polarization of laser beam because it is not necessary. The laser power is decreased by the attenuator to avoid adverse effects to the clusters as much as possible. The sample condition of the concentration of o-H_2 is about 1000 ppm, and CH_3F is 0.4 ppm.

The pumping experimental setup is also the same. When we bleach the target peak, the attenuator

for decreasing the laser power is taken away. The probe laser is used with attenuator to observe the spectrum.

§ 4.3 Results and analyses

4.3.1. The *n* = 0 satellite series

The spectrum around the n = 0 main peak is shown in detail in Fig. 4-1(a), which is measured at one hour after 7 K annealing. The horizontal axis plots wavenumber with offsets that are adjusted to the main peak position at 0. We observe about six satellite peaks to the red side of the main n = 0 peak and two weak peaks to the blue side. The spectral reproducibility of these peaks is confirmed in all our observed crystals. Here we focus on the red side satellite peaks, which are numbered with a letter n' starting from the main peak as n' = 0. The blue side satellite peaks are numbered n' = -1 and -2 from the main peak, and we discuss them below. In this series, it should be pointed out that the n' = 3 peak has a red sided shoulder, and a similar shoulder is observed for the n' = 5 peak. Such a red-side shouldered structure is a common feature of the main series, which had been revealed as superposition of ${}^{q}Q_0(0)$ (*ortho*-CH_3F (K = 0)) and ${}^{q}Q_1(1)$ (*para*-CH_3F (K = 1)) transitions [57]. Therefore, these satellite peaks most likely originate from similar clusters which contain a single CH_3F molecule.

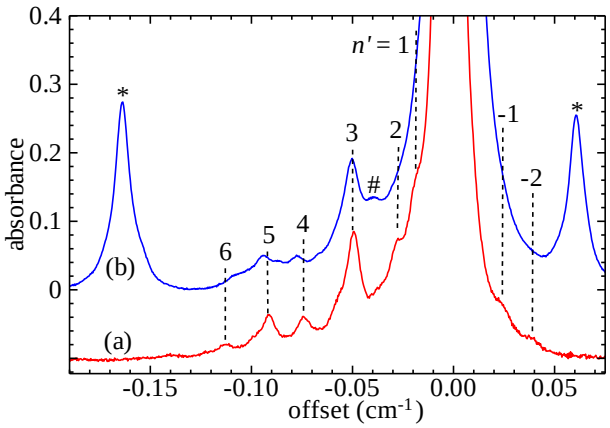

Fig. 4-1. The enlarged absorbance spectra measured at one hour after 7 K annealing. The temperature of the crystal is 1.8 K. (a; red) the n = 0 main peak at 1040.187 cm^{-1}. (b; blue) the n = 1 main peak at 1039.480 cm^{-1}. The abscissa axis is the offset wavenumber from each main peak. The peaks belong to the satellite series are labeled with a number n' ordered from the main peak. Peaks marked with * and # are not considered as a member of the satellite series.

4.3.2. The *n* = 1 satellite series

Another important fact is that there is a similar satellite series observed to the red side of the $n = 1$ main peak. As shown in Fig. 4-1(b), the offset position of each n'-th satellite peak in the $n = 0$ and 1 main peaks correlates very well. Therefore, it is convenient to label those satellite peaks with a set of the number n and n' as (n, n'). In this manner, the n-th main peak is also represented as (n, 0) peak. It should be noted that (1, 3) peak is the strongest in the $n = 1$ series and has also the shouldered structure on the red side just like the $n' = 0$ pair.

However, there are additional peaks marked with # and *, as we mentioned in Chap. 3. The # peak is also observed at $n = 0$, but * peaks appear only in the $n = 1$ region as seen in Fig. 4-1. We found that these peaks have different temporal behaviors from the (n, n') series, as described in Fig. 3-5 at Chap. 3.

4.3.3. Fitting analysis

The observed spectral pattern and temporal behavior, as discussed in Chap. 3, suggest that each component of the main series, which corresponds to the CH_3F-(o-H_2)$_n$ clusters, has a similar satellite series. Furthermore, the temperature dependence shown in Fig. 3-7 in Chap. 3 indicates that the satellite series are not constructed by some rotational components. If it were related to some rotation of CH_3F, the temperature increase should provoke a reaction. However the result is completely the opposite, therefore we estimate that the origin of satellite series dose not relate to a rotation of CH_3F. We need an extended cluster model which can describe the hierarchy of structures observed in the spectrum. First, we do not think that the new satellite series involves more than one CH_3F in the cluster. Because once dimer is created, strong dipole-dipole interaction would more or less hinder the C_3 axis rotational motion. Even if the hindrance is not so strong, the rotational states become completely different energy structures because of the coupling of two identical rotors. The shoulder structure observed in the satellite peaks is very similar to that of the main series. This fact suggests that only a single CH_3F is freely rotating along the C_3 axis in the cluster just like the CH_3F-(o-H_2)$_n$ clusters. Another reason why we can deny the possibility of dimers is the small concentration of CH_3F. There was a report on the CH_3F dimer in Ar matrix isolation, in which the dimer was produced in a supersonic-jet expansion, then deposit on a cold plate [68]. Even though their concentration of CH_3F was 1000 ppm, which is 2500 times larger than our concentration of 0.4 ppm, the intensity of the dimer was much smaller than that of the monomer. In addition, the peak attributes to the dimer of CH_3F would appear around 1030 cm^{-1}, therefore the shift value is different

from the satellite peaks. It is hard to consider a cluster belonging to the new satellite series would involve more than one CH_3F. Instead, we formulate a hypothesis based on an extended cluster model of CH_3F-(*o*-H_2)$_n$-(*o*-H_2)$_{n'}$, in which *n'* indicates the number of *o*-H_2 in the second-nearest neighbor sites. Each *n'*-th peak in the satellite bands is not well separated. In order to extract more information, we try to decompose the observed spectrum into each component. The model function used in the fitting analysis is a superposed Lorentzian function considering the pair of transitions from *ortho*- and *para*-CH_3F.

$$f(\omega) = \sum_{n=0}^{1} \sum_{n'=0}^{6} \left[\frac{A^o_{nn'}}{(\omega - \omega^o_{nn'})^2 + (\gamma^o_n)^2} + \frac{A^p_{nn'}}{(\omega - \omega^o_{nn'} + \Delta\omega^{op})^2 + (\gamma^o_n)^2} \right] \qquad (4-1)$$

In this formula, *ortho*- or *para*-CH_3F is distinguished by superscript "*o*" or "*p*", and $A_{nn'}$ and $\omega_{nn'}$ represent the intensity and frequency of the (*n*, *n'*) peak, respectively. $\Delta\omega^{op}$ represents the frequency difference between the *ortho*- and *para*-CH_3F pair, and is assumed to be common among all the satellite peaks because no significant difference of $\Delta\omega^{op}$ has been observed in the main series. For the linewidth parameters, we assume that their variation for the *n'*-th component of the same *n* value is negligibly small. Therefore, we could reduce the number of independent linewidth parameters to four: γ_0^o, γ_1^o, γ_0^p and γ_1^p.

Here, the upper limit of *n*' is assumed to six, because there are six sites in the second-nearest neighbor in hcp crystal. As reported previously in Ref. 64, the *para*-CH_3F state relaxes into the *ortho*-CH_3F state at a rate of several hours in *para*-H_2 crystals, which was supposed to be accelerated by the *o*-H_2 involved. The *o*-H_2 molecules in second-nearest neighbor could also accelerate the relaxation of CH_3F. So the spectral intensity ratio between *ortho*- and *para*-CH_3F should be treated as a time-variant parameter depending on each (*n*, *n*') peak. However, since our laboratory has reported that the relaxation rate in the (0, 0) peak is not so different from that in the (1, 0) peak [57], we can fix the ratio of integrated peak intensity to a common ratio *C* for all (*n*, *n*') peaks as follows,

$$C = \frac{A^p_{nn'} \times \gamma^p_n}{A^o_{nn'} \times \gamma^o_n} \qquad (4-2)$$

This treatment means that $A^p_{nn'}$ is replaced with $CA^o_{nn'}\gamma_n^o/\gamma_n^p$, and the number of the running parameters is reduced. Still, the correlation among the parameters $A_{nn'}$, γ_n, $\Delta\omega^{op}$, and *C* remained strong and it is difficult to determine them independently. Therefore, both the (0, *n*') and (1, *n*')

series are simultaneously fitted while sharing $\Delta\omega^{op}$ and C in the least squares analysis. The result thus determined for the spectra observed after 7 K annealing is listed in Table 4-1 and graphically

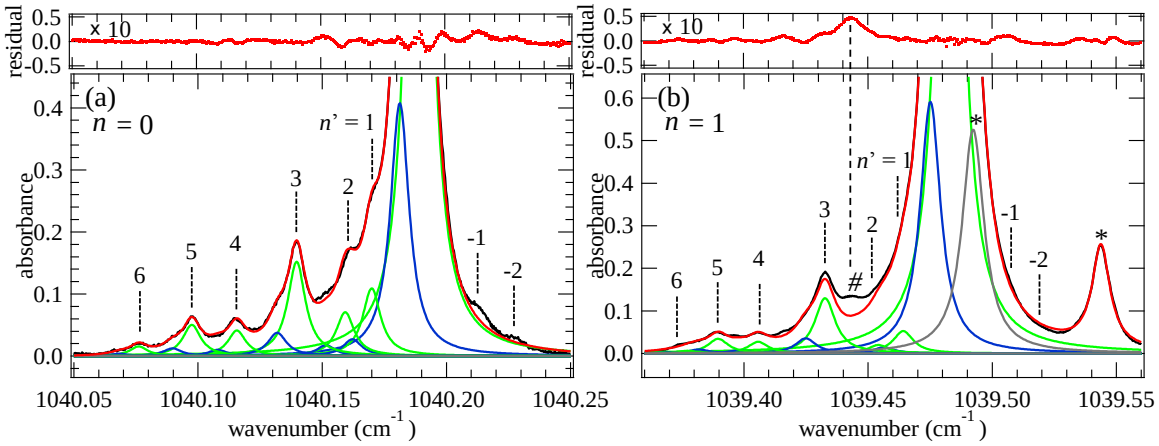

Fig. 4-2. The result of the fitting analysis of (a) n = 0 and (b) n = 1 main peak and its satellite peaks. Bottom panel: the spectrum (black) observed at 1.8 K following the 7 K annealing is well fitted with a sum (red) of n'-th *ortho*- (green) and *para*- (blue) components. Peaks marked with * and # (gray) are excluded in this analysis. Top panels: residual error multiplied by 10.

Table 4-1. The determined fitting parameters of the satellite series[a] of CH_3F in the *p*-H_2 crystal[b]

	n = 0		n = 1		n = 2
n'	$A^o_{0n'}$	$\omega_{0n'}$ (cm^{-1}),	$A^o_{1n'}$	$\omega_{1n'}$ (cm^{-1}),	$A^o_{2n'}$
0	3.10(01)×10^{-5}	1040.1890 [c]	5.24(03)×10^{-5}	1039.4830 [c]	3.91(01)×10^{-5}
1	2.05(03)×10^{-6}	1040.1699(1)	1.28(05)×10^{-6}	1039.4641(2)	4.9(47)×10^{-8}
2	1.33(03)×10^{-6}	1040.1593(1)	4.81(76)×10^{-7}	1039.4541(7)	4.31(62)×10^{-7}
3	2.85(02)×10^{-6}	1040.1397(0)	3.15(07)×10^{-6}	1039.4327(1)	1.09(04)×10^{-6}
4	7.76(20)×10^{-7}	1040.1156(2)	6.59(27)×10^{-7}	1039.4058(3)	2.98(32)×10^{-7}
5	9.49(21)×10^{-7}	1040.0975(1)	8.33(33)×10^{-7}	1039.3896(3)	5.31(32)×10^{-7}
6	2.92(20)×10^{-7}	1040.0761(5)	1.54(31)×10^{-7}	1039.3772(15)	4.5(31)×10^{-8}
γ^o_n (cm^{-1})	4.332(08) ×10^{-3}		4.925(14) ×10^{-3}		6.499(14)
γ^p_n (cm^{-1})	4.550(37) ×10^{-3}		4.999(36) ×10^{-3}		6.804(23)
$\Delta\omega^{op}$ (cm^{-1})	7.79(2) ×10^{-3} [d]				7.79 ×10^{-3} [e]
C	2.86(7) ×10^{-1} [d]				2.86 ×10^{-1} [e]
Standard deviation(1σ)	0.004 [d]				0.004

[a] Spectrum was measured just after 7 K annealing at the crystal temperature of 1.8 K.
[b] The concentrations of *o*-H_2 and CH_3F are 1000 ppm and 0.4 ppm, respectively.
[c] Fixed to the value of Ref. 57
[d] common to n = 0 and 1.
[e] fixed to the value determined in n = 0 and 1.

shown in Fig. 4-2. Each *ortho* and *para* component of the (*n*, *n'*) line is shown separately, and the summed up model function and observed spectrum are overwritten. The two peaks marked with * are treated as additional Lorentzian components. The residual error shows that there is no trace of any peaks at the position where *n'* = 7 would appear if it existed. Meanwhile there is an unidentified peak at 1039.44 cm^{-1} marked #, which is excluded in this analysis because of its different temporal behavior as mentioned above.

4.3.4. The *n* = 2 satellite series

Following the success of the fitting analysis for the *n* = 0 and 1, an attempt to fit the *n'* series of the *n* = 2 main peak was performed with the same model function. Since the intensities of the *n* = 2 satellite are too weak to determine the interval values of $\Delta\omega_{2,n'}$ independently, we had to fix them to $\Delta\omega_{0,n'}$. It is necessary to add two Lorentzian components in the blue side of the *n* = 2 main peak. The result of fitting is shown in Table 4-1 and Fig. 4-3.

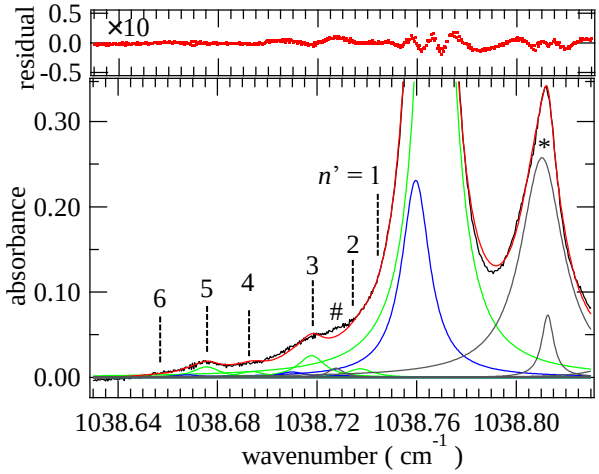

Fig. 4-3. The result of the fitting analysis of *n* = 2 main peak and its satellite peaks. The caption is the same as Fig. 4-2.

The error of the fitting and standard deviation are as small as those of the *n* = 0 and 1. This correlation suggests that the *n* = 2 main peak also has the satellite series with the same interval peak pattern as *n* = 0 and 1. Meanwhile, the linewidth of *ortho*-CH_3F and *para*-CH_3F is determined to be γ^o = 6.499(14) × 10^{-3} cm^{-1}, and γ^p = 6.804(23) × 10^{-3} cm^{-1}, respectively. The linewidth tends to increase with an increase in *n*.

4.3.5. Pumping of each peak

The results of each main peak's bleaching are shown in through Fig. 4-4(a) – (c). In order to check the difference by pumping each peak, the black trace shows the spectrum before the pumping and red trace shows it after the pumping. Fig. 4-4(a) describes that the *n* = 2 main peak decreases and the *n* = 1 satellite peaks increase when the *n* = 2 main peak is pumped. The satellite peaks at *n* = 1 not only increase on the positive number side of *n'*, but also on the negative side. The increased position looks similar with the position of (0, -1) and (0, -2). We can't determine that the peak is the same

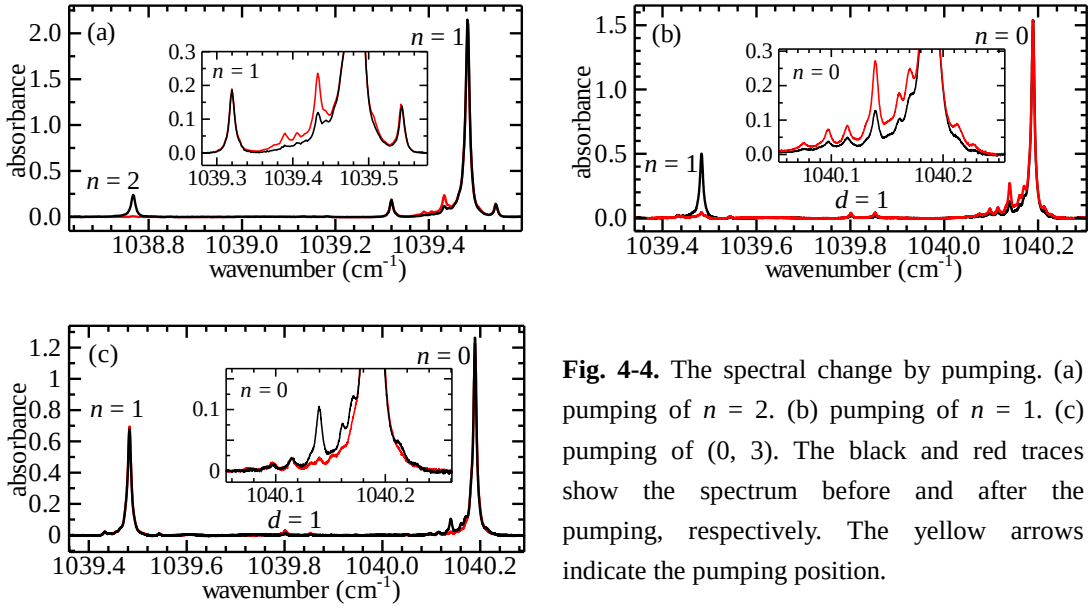

Fig. 4-4. The spectral change by pumping. (a) pumping of n = 2. (b) pumping of n = 1. (c) pumping of (0, 3). The black and red traces show the spectrum before and after the pumping, respectively. The yellow arrows indicate the pumping position.

origin as the one when n = 0 since n = 1 has the one peak on blue side of the main peak, as reported in Ref. 57. The main peak does not change the intensity. The integrated intensities of both of before and after the pumping are nearly conserved. The integrated intensities from before and after the pumping are conserved at 102(25)%. The value with error is obtained from the average of the same experimental results in different samples. Thus, the population of the cluster that corresponds to the n = 2 main peak is mainly changed to that of the satellite peaks of n = 1. These changes by the pumping would be caused by the migration of *o*-H_2 around CH_3F. The irradiation beam gives the vibrational energy for CH_3F and the energy transfers to the lattice of *o*-H_2 crystal as thermal energy. The *o*-H_2 molecules in the first nearest neighbor site of CH_3F can migrate due to getting the thermal energy.

Fig. 4-4(b) shows the result that the n = 1 main peak is pumped. The response is very similar with that of n = 1 and 2 at pumping of the n = 2 peak. The n = 1 main peak decreases and the n = 0 satellite peaks increase. The two peaks labeled *d* (to be discussed in Chap. 5) also increase. However, the intensity of the main peak at n = 0 does not change. The integrated intensities from before and after the pumping are conserved at 92(9)%. Thus, almost the entire population of the cluster that corresponds to the n = 1 main peak is changed to that of the satellite series of n = 0.

Fig. 4-4(c) shows the result of pumping of (0, 3) peak. This experiment is same as in Ref. 58. The result describes the spectrum with pumping of (0, 3) taken soon after pumping of the n = 1 main peak. It should be noted that we can't only discuss the effect of the pumping since we already know that the n = 1 peak can recover some intensity over time after pumping of n = 1. The result in Fig.

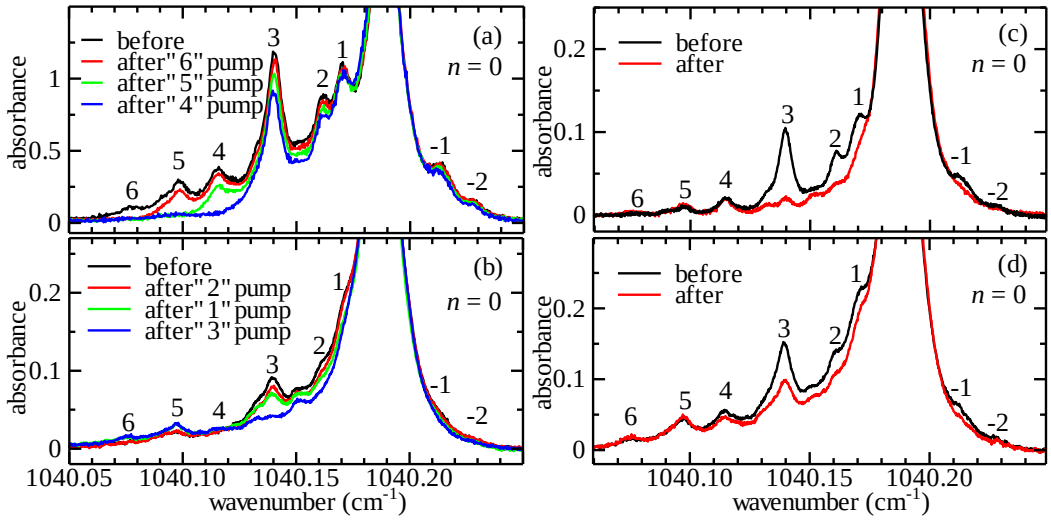

Fig. 4-5. The spectrum change by pumping of satellite peaks of n = 0. (a) pumping of n' = 6, 5, and 4. (b) pumping of n' = 3, 2, and 1. (c) pumping of n' = 3. (d) pumping of n' = -1. The order of the pumping is described at upper-left in each graph. Each color of trace and arrow relate the order of pumping.

4-4(c) shows that most of the population of the (0, 3) is transferred to the n = 1 main peak. The integrated intensities from before and after the pumping are conserved at 73(14)% since the population of the n = 0 cluster changed to the n = 1, 2 and 3 clusters. With the decrease of the (0, 3) peak, the other satellite peaks (n' = 1 and 2, and n' = -1 and -2) decrease in intensity. In order to understand the phenomenon, we need to survey the correlation between the satellite peaks.

In order to check the correlation between satellite peaks, each satellite peak at n = 0 is bleached, and the results are depicted in through Fig. 4-5(a) – (d). Each graph depicts only the satellite peak region. The pumping positions are described at the upper right in the figures. The numbers at each peak in the figures correspond to the number of n'. Fig. 4-5(a) – (d) show some of the pumping results simultaneously and the order of the pumping follows in order from the top of the notation on the left side. Each spectrum is measured in an interval of a few minutes. From these results, the satellite peak can be bleached alone. It can be clearly observed that the three peaks numbered n' = 6, 5 and 4 are bleached alone. n' = 1 and 2 look to be bleached with neighbor n' peak, however their relative intensities are changed by pumping of each peak. The decreasing with other peaks would occur to the neighbor peaks is also bleached by pumping of their tail, as shown in Fig. 4-2, and therefore the rate of decrease are changed by pumping position and the relative intensity is not conserved. The n' = 3 peak decreases along with n' = -1 and -2. It would not be the same mechanism in relation to n' = 3, 2, and 1, since the peak position is far enough and the overlap of each peak's tail can be neglected. In order to check that the same phenomenon could be observed in the n = 1

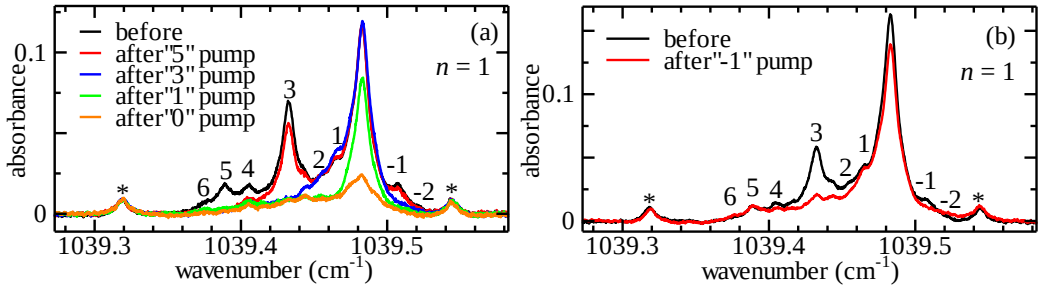

Fig. 4-6. The spectrum change by pumping of satellite peaks of n = 1. (a) pumping of n' = 5, 3, and 1. (b) pumping of n' = -1. The order of the pumping is described at upper-left in each graph. Each color of trace and arrow relate the order of the pumping.

satellite series, we did the same experiment to n = 1 and the results are depicted in Fig. 4-6(a) - (b). From these results, the same phenomenon occurred from the pumping experiment to the satellite peaks of n = 1. The peaks of n = 1, including the main peak, respond weaker to the pumping than n = 0. This means that the decay time of n = 1 by bleaching is faster than n = 0. Thus, the stability of each cluster is different and the one *o*-H_2 molecule at the first nearest neighbor site could be easily migrated to a farther site than what happened to the opposite phenomenon. The details of the physical implications of the pumping are discussed in Chap. 6. The spectrum of n = 1 shown in Fig. 4-6(a) – (b) is one piece of evidence that the peak pumped there decreases with neighbor peaks much more than that of n = 0.

Fig. 4-7 shows the spectrum pumping of the n = 0 main peak. Fig. 4-7(a) shows the spectrum at the range of n = 0 to 1, and (b) and (c) show the area expanded at the region around n = 1 and 0, respectively. The black, red, and blue traces describe the spectrum before pumping, after pumping,

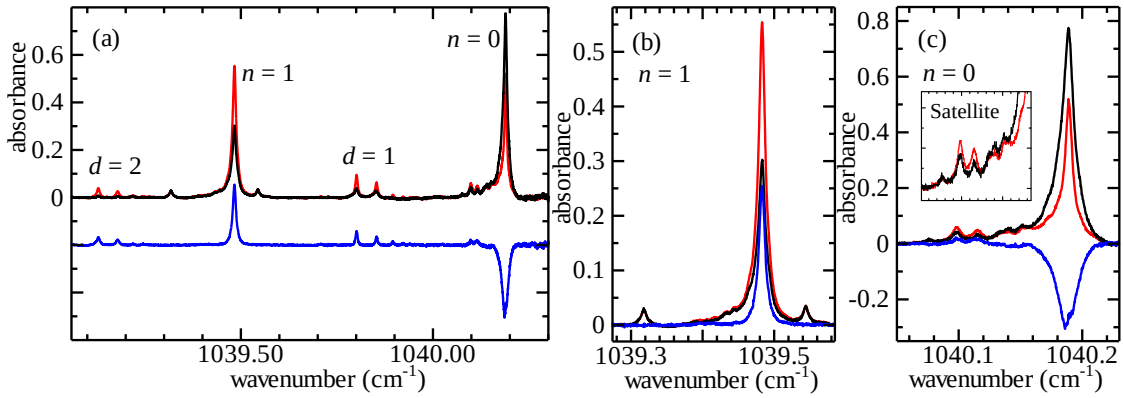

Fig. 4-7. The spectrum change by pumping of n = 0 main peak. (a) The spectra at before (black) and after (red) the pumping. The blue trace indicates the difference of them with offset. (b) The enlarged absorbance spectra at n = 1. (c) The enlarged absorbance spectra at n = 0. The range of satellite peaks is expanded and shown at the figure in (c).

and the difference between them, respectively. The increasing position at $n = 1$ is the only main peak component, thus (1, 0) peak, and did not appear at the satellite peaks. The peaks labeled *d* (to be discussed in Chap. 5) also increase by the pumping of the $n = 0$ main peak. The linewidth of $n = 0$ peak is narrower than before the pumping. The bleached line shape, as shown by the blue trace in Fig. 4-7(c), explains that the main peak is not composed of a single component. The broad line shape would indicate that many peaks come from the clusters CH_3F and some *o*-H_2 molecules in far sites, like third nearest or greater, gather around the main peak component. Furthermore, if the classical treatment could be used, the broad line could also be affected due to the local position of *o*-H_2 around CH_3F. Thus, there are some different configurations depending on the position of *o*-H_2, as at the fluorine-side plane, or methyl-side plane of CH_3F in the hcp crystal. These different configurations could have different binding energies, resulting in small spectral peak shifts. The shift to the red side could be easily understood since it would be the same mechanism of the series of *n* and *n*'. We know it is not straight forward to relate the intensity of the interaction to the transition frequencies, however the peaks appeared at blue side of main peak should be surveyed more in order to understand the mechanism of the blue shift. The reaction to pumping of $n = 0$ can be explained by the cluster model as shown in Fig. 4-8. The $n = 0$ could be divided for some types of clusters. If the cluster has no *o*-H_2 even in far sites, the cluster cannot be changed by the pumping like Fig. 4-8(a). If some *o*-H_2 molecules stay in the third or a greater far sites, the cluster form can change to an $n = 1$ or higher *n*'-th cluster, as described in Fig. 4-8(b). Furthermore, we observe the (0, 5) and (0, 6) increase when $n = 0$ main peak is bleached as shown in Fig. 4-7(c). It could cause that the cluster of

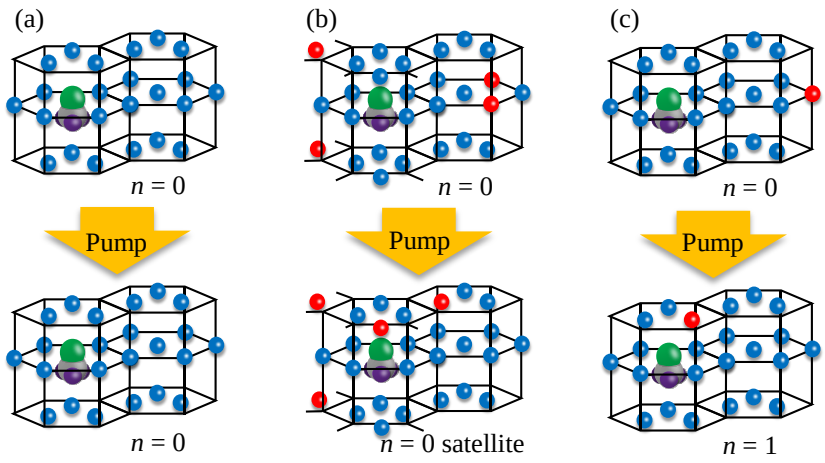

Fig. 4-8. The image for the transition of cluster structure by pumping of $n = 0$ main peak. (a) $n = 0$ cluster with few *o*-H_2 molecules shown by red molecules. (b) $n = 0$ cluster with high concentration of *o*-H_2. (c) $n = 0$ cluster with a few *o*-H_2 molecules.

(0, 2) or (0, 1) with some *o*-H_2 molecules in its third nearest site to change to the clusters of (0, 5) or (0, 6) by the migration of *o*-H_2 from a far site to a second-nearest site.

4.3.6. Temperature dependence of satellite peak

The temperature dependence of the satellite peaks is observed and the results are shown in Fig. 3-7 in Chap. 3. The result indicates that the satellite series can be observed at fewer than 4 K. However, they are not be observed at 5 K for both of n = 0 and 1. The satellite peaks have the same reaction to the temperature of the substrate. Their origins would be the same mechanism. In addition, we can assume that the depth of the potential barrier for forming a satellite series is around 4-5 K. At that temperature, the main n series can still exist. It would indicate that the potential barrier of first nearest site to *o*-H_2 is higher than 5 K. The potential barrier to *o*-H_2 in the second nearest site might be shallower than that in the first one. The experimental result would support the second-nearest model for the origin of the satellite peaks. It is a very curious phenomenon that the unknown peak labeled # also disappeared at 5 K.

§ 4.4 Discussion

4.4.1. Peak position of the satellite series

The intervals of the satellite peaks: $\Delta\omega_{n,n'}$ are not as equally spaced as those of the main series, but the shift pattern of the n = 0 and 1 satellite series is very similar, as seen in Fig. 4-9. Furthermore, the n = 2 satellite series is also well represented by using the interval pattern of n = 0. These facts suggest that the n'-satellite series are derived from the same mechanism. Under the second-nearest neighbor model of CH_3F-(*o*-H_2)$_n$-(*o*-H_2)$_{n'}$, the n'-series should arise from the interaction of CH_3F and n' *o*-H_2 molecules in second-nearest neighbor sites. Analogous to the main n-series, in which each peak corresponds to the cluster possessing n *o*-H_2 molecules in first nearest neighbor sites, the pattern of the satellite n'-series might be determined by the same mechanism. However, the averaged interval of 0.02 cm^{-1} for the n'-series is about thirty times smaller than that of the main n-series. The dipole-quadrupole interaction between CH_3F and *ortho*-H_2 varies inversely with the fourth power of the distance. The ratio of the first and second nearest neighbor distance is 3.78/5.35 and its fourth power is 0.24. This suggests that the second-nearest neighbor frequency shifts should be much larger than observed, even if the dielectric permittivity of hydrogen (ε = 1.28) is taken into consideration [84]. However, we know it is not straight forward to relate the stability of the clusters

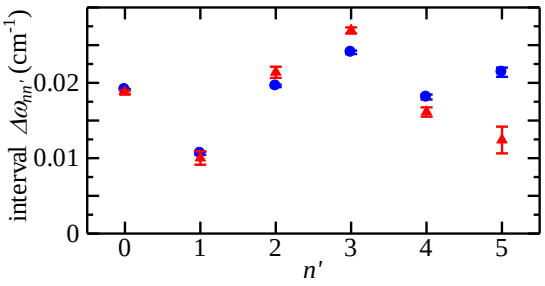

Fig. 4-9. The intervals $\Delta\omega = \omega_{n,n'} - \omega_{n,n'+1}$, of the satellite peaks for n = 0 (blue circle) and n = 1 (red triangle) measured just after 7 K annealing. The abscissa axis is the index number for the satellite peaks; n'.

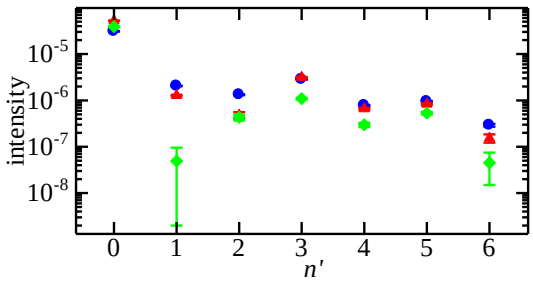

Fig. 4-10. The intensity distribution of the n = 0 (blue circle), n = 1 (red triangle) and n = 2 (green diamond) satellite series.

to the transition frequencies. Rather, the irregularity of the interval pattern shown in Fig. 4-10 might suggest the possibility of an inhomogeneous frequency shift due to a local position of *o*-H_2 in the cluster.

4.4.2. Intensity distribution in the satellite series

Fig. 4-10 shows the intensity distribution of the satellite series of n = 0, 1 and 2. Both n = 0 and 1 are very much like each other, however, these intensity distributions do not appear statistical. This is contrary to the case of the main series, which shows a typical Poisson distribution [66] before annealing. The dominant feature of the n'-series is that the intensity of n' = 3 is notably stronger than others. This phenomenon looks like the pattern of n-series, as shown in Fig. 3-1(a) in Chap. 3. However the trend is also observed for the thin sample, as shown in Fig. 3-1(b). Thus, even if the n = 3 main peak is weaker than other peaks in the n-series, the intensity of n' = 3 would be stronger than others of that n'-series. This fact suggests that n' = 3 might be a kind of 'magic number' related to a relatively stable structure of the clusters. There are six second nearest neighbor sites in the hcp crystal. Under the cluster model with second nearest neighbor, three of them are in the fluorine-side and other three in the methyl-side. As occupation of the former site by *o*-H_2 is more stable than the latter site, a kind of closed-shell effect might be brought by filling all the three sites.

4.4.3. ortho-para ratio

In free space, the conversion between *ortho*- and *para*-CH_3F seldom happens, therefore, the total thermal population ratio parameter C of *para* to *ortho*-CH_3F is determined to be 1.25 at room temperature [85]. Meanwhile, at the cold temperature limit, all the population is located at each

lowest state, so the ratio of $K = 1$ to $K = 0$ state should keep this statistical ratio in the gas phase. The population ratio parameter C in the p-H_2 crystal is determined to be 0.286(9) just after 7 K annealing, which is 2.5 hours since the time the crystal deposition started. After 6 hours, the C ratio becomes $2.69(84) \times 10^{-2}$. This determines a decay ratio of 0.39(7) h^{-1}, which should be compared with the previous result of 0.13(3) h^{-1} reported by Y. P. Lee group [64]. The difference presumably comes from the concentration of o-H_2 and the temperature in the crystal. Our density and temperature are 1000 ppm and 1.8 K, and theirs 100 ppm and 3.3 K, respectively. The higher density of o-H_2 makes the decay rate of the *para*-CH_3F faster through the magnetic interaction between the nuclear spins. This phenomenon has been reported for other molecules like CH_4 [33,39,86] or CH_2Cl [36], as mentioned above. In addition to this, the higher temperature might also make it faster due to thermal fluctuations. The experimental result suggests that the magnetic interaction of o-H_2 could exceed the thermal effect.

4.4.4. Linewidth

Regarding the linewidth of the ν_3 band, Miyamoto *et al*. reported that the overall linewidth of the main series depends on the concentration of o-H_2 from the linewidth analysis on FTIR spectra [87]. Our previous laser study showed that the linewidth of the main peak (γ_n) has a tendency to increase with an increase in n [57]. In this systematic fitting work, the linewidth of each satellite peak ($\gamma_{nn'}$) is also represented well with a common linewidth of the main peak γ_n, of course, which tends to increase with the increase of n. The reason why we cannot see a significant n'-dependence is the same reason the peak-shifts of the satellite peaks are too small as described in Sec. 4.4.1.

General speaking, there are two ways of thinking about this tendency to increase. The first is the idea of inhomogeneous line broadening due to the local position of o-H_2 around CH_3F. That is to say, each n-th main peak consists of several Lorentzian components. For example, in the case of the $n = 1$ cluster, there are three different configurations depending on the position of o-H_2 at the fluorine-side plane, body plane, or methyl-side plane of CH_3F in the hcp crystal. These different configurations could have different binding energies, resulting in small spectral peak shifts. If the energy difference of these three configurations is small enough for all to be populated thermally, the spectral line profile would be a superposition of those configurations. Up to $n = 6$, the larger n-th cluster has more configurations, thus the linewidth becomes wider with the increase of n. The second is homogeneous line broadening due to the presence of o-H_2 around CH_3F. The relaxation of an optically excited state would be enhanced by a larger quantity of o-H_2 in nearest neighbor sites. As the result, the decay

accelerates with the increase of *n*. In this case, position of *o*-H_2 in the twelve nearest neighbor sites is not important because *o*-H_2 is postulated to be non-localized.

From the pumping results, as shown in Fig. 4-7, the real linewidth of only CH_3F in pure solid *p*-H_2 could be narrower than estimated by the fitting analysis. The main peak linewidth after the pumping of $n = 0$ main peak is several tens of percent narrower than that before the pumping. It's nearly impossible that the effect *o*-H_2 is completely avoided, since the sample made by only *p*-H_2 couldn't be established. We should note that the *n*-series and *n*'-series would include the broadening effect. We believe that the linewidth will be discussed further and determined by comparing with the estimated value from the theoretical approaches in the future.

4.4.5. Reactions to the pumping

The fact that each satellite peak can be bleached indicates that the origins of the satellite peaks are not the rotational components. Of cause CH_3F in solid *p*-H_2 couldn't rotate freely, except along C_3 axis, as well known. However, even if the rotation could be allowed, the shift should be much larger and the peak intensity should be repaired more quickly. Therefore, we determine their origins should be more stable, like some kind of clusters.

The $n' = 3$ peak decreases along with $n' = -1$ and -2. As discussed above, it would not be the same mechanism in relation to $n' = 3$, 2, and 1. In the case for the neighbor peaks, as $n' = 3$, 2, and 1, the decreasing with other peaks would occur to the neighbor peaks is also bleached by pumping of their tail, as shown in Fig. 4-2, and therefore the rate of decrease are changed by pumping position and the relative intensity is not conserved. On the other hand, in the case for (0, 3) and (0, -1) or (0, -2), the peak position is far enough and the overlap of each peak's tail can be neglected. The relation between (0, 3) and (0, -1) or (0, -2) could be explained by the difference of the position of *o*-H_2 in one cluster. Thus, the number of *o*-H_2 molecules is the same for these three peaks, but the position is different. As discussed above, the *o*-H_2 position to the CH_3F could change the peak position from the classical point of view. The experimental result shows that the decay time of (0, 3) is slower than (0, -1). The structure of the $n' = 3$ cluster could have the most stable position for three *o*-H_2 molecules in second nearest neighbor site for CH_3F. The structure of the $n' = -1$ and -2 clusters could have other formations with CH_3F and three *o*-H_2 molecules in its second nearest neighbor sites. If the positions of *o*-H_2 molecules can change, the experimental results could be explained. This is one possibility but we haven't found critical evidence of it.

By assuming the origin of satellite peak is second-nearest model, the model could not explain the

results of pumping. For example, when the n = 1 main peak is bleached, as shown in Fig. 4-4(b), the one *o*-H_2 molecules in first nearest neighbor migrates to second-nearest or greater far site and the n = 0 main peak or (0, 1) should increase. However, the result shows that all satellite peaks increase. Thus, the number of *o*-H_2 molecule is not conserved in the cluster model. In order to explain the result of pumping of n = 1, we estimate that if some *o*-H_2 molecules in the third or further sites are migrated to second nearest site since the site is more stable. However, if the hypothesis is correct, the experimental results of pumping of (0, 0) or (0, 3) would not be explained. The n = 1 main peak increased by pumping of the n = 0 main peak or (0, 3), as shown in Fig. 4-4(c) and 4-7. If *o*-H_2 is more stable in second-nearest than in the farther site, the population of n = 0 should migrate to that of the n = 1 satellite peaks by pumping of n = 0. The results, however, did not show that. It would mean that the mechanisms at the migration of *o*-H_2 molecule from the first to the second nearest site and from the second to the first nearest site are different. This will be the main issue of the research from now on. Theoretical studies are desired to confirm these phenomenons.

4.4.6. The versatility of the fitting function

We check the versatility of the fitting function by trying a fitting analysis on other spectra. These spectra data are chosen from two points. One is the observed time difference, since the spectrum of CH_3F-(*o*-H_2)$_n$ changes its intensity distribution with time, as shown in Chap. 3. The fitting analysis results describes that the function supports the experimental results. The population ratio parameter C of *para* to *ortho*-CH_3F is changing with time, as discussed in Sec. 4.4.3. The other point is the difference of the sample conditions. We try the fitting analysis to some different samples. To some samples, the fitting function represents the experimental results well. On the other hand, some spectra are not successful in the fitting analysis with this function. The observed spectra with weak satellite peaks are not able to be fitted by this fitting function. The accuracy of the spectrum shape of the satellite series is not enough for this fitting analysis if the spectrum has only a weak satellite series. As mentioned in Chap. 2, the accuracy of the base line decreases with decreasing the intensity of satellite series. This is one main issue for an ill-fitting analysis on some spectra. The spectra after laser pumping of any peak also cannot be used for s fitting analysis. One reason is that the line width of the peak pumped of is changed, as mentioned at Sec. 4.3.5. The line shape would be created with the sum of many of the peaks from the cluster of CH_3F and *o*-H_2 molecules in its third or farther sites. Therefore the line width of one peak would be easily changed from other peaks by pumping. From these results, we determine that the fitting function has versatility with some conditions. One is

that the parameters of peak position should be fixed if the signal of the satellite series is not clear enough. And also, we should consider the possible value of each parameter, especially $\Delta\omega_{n,n'}$, γ_n and *C*. These parameters can be dramatically changed in a fitting analysis, however from the physical point of view, these value should have similar value with those in Table 4-1. The population ratio parameter *C* of *para* to *ortho*-CH_3F can be changed with time but the value can also be estimated from the previous researches. It cannot be larger than 1.25 since it becomes smaller than that of the total thermal population ratio at room temperature. This fitting function can be used for any spectra so long as the points we mentioned are taken into account.

§ 4.5 Conclusion

New satellite series were found to the lower energy side of each main peak of the ν_3 band of CH_3F embedded in a *p*-H_2 crystal. The red shoulder line profile in each peak suggests single CH_3F molecule is rotating around the C_3 axis in the *p*-H_2 crystal. Some common features including temporal behavior, temperature dependence and reaction to the pump beam suggest that the satellite series originate from the clusters described by the second nearest neighbor model. A profile analysis based on this model was used to resolve each Lorentzian component and the detailed features of the series were studied. The peak intervals in the satellite series are not as equally spaced as the main series, but there is a strong resemblance among the satellite series. The peak intensity distribution in the satellite series showed an irregular pattern, rather than a statistically smooth one, but there is a strong resemblance among the satellite series in which $n' = 3$ is the strongest. Among those series the linewidths are very similar. However, the observed peak shifts in the satellite series are too small to be explained by a simple dipole-quadrupole interaction model.

In addition, we applied a pump probe experiment to each peak. From these results, each satellite peak can be breached individually. However the number of *o*-H_2 molecules around the CH_3F cluster is not conserved between before and after pumping.

It would be natural to consider the second nearest neighbor cluster model as an extension of the first nearest model. Indeed, some observations are explained in analogy with the first nearest neighbor model, but quantitative assessment is not yet satisfactory.

Chapter 5 Alignment of CH_3F in solid *p*-H_2

§ 5.1 Introduction

As described above, the target molecules studied in *p*-H_2 crystals can be classified into two groups, namely molecules which can rotate in the crystal and those which cannot. The border of these groups was reported that it depends on the amount of the rotational constants of dopant molecules. M. E. Fajardo *et al.* reported that the molecules whose rotational constant is less than ~ 1.5 cannot rotate freely in solid *p*-H_2 [88]. The threshold has not been determined completely therefore it has been one big topic in the studies of solid *p*-H_2.

In the former case, the *M*-degeneracy of a rotational state splits in the crystal field. Therefore, polarization spectroscopy is useful to assign the spectral peaks, because the crystal *c*-axis is known to be normal to the substrate [39,89,90]. Using the selection rule on ΔM, the alignment of a dopant molecule was studied [33,34].

In the latter case, without rotation, there exist no *M*-components. Only a single transition which corresponds to a pure *Q*(0) vibrational transition is observed because the rotational motion is hindered. So there are fewer experimental studies on the alignment of a dopant molecule, but there has been some theoretical work based on *ab initio* calculations. For example, the alignment of CO_2 was studied by Jun-He Du *et al.* [35]. They calculated the potential energy surface of CO_2 in a *p*-H_2 crystal and estimated that the polar angle of CO_2 is 51.3° with respect to the crystal *c*-axis. This estimate has not been confirmed experimentally.

CH_3F is another member of the latter nonrotating group. Y. P. Lee's group found that, in a *para*-H_2 crystal, CH_3F rotates freely around its C_3 symmetry axis but does not rotate around the other two principal axes [52]. This raises the important question as to which direction the C_3 axis points in *p*-H_2 crystal. This research attempts to decide the orientation of CH_3F in solid *p*-H_2.

So far most of spectroscopic studies on CH_3F in *p*-H_2 crystal were done by FTIR spectroscopy. In this research, the IR quantum cascade laser for high-resolution and high-sensitivity absorption spectroscopy of this system is used. In the chapter, the experimental results of laser polarization spectroscopy in order to probe the alignment of CH_3F in *p*-H_2 crystals are introduced.

Most parts of this chapter are the same experimental results and discussions that we published in Ref. 62.

§ 5.2 Experimental details

The experimental setup is described in Sec. 2.2.2. The substrate is placed in two setups. One is the 45˚configuration in which the substrate is placed at 45˚ to the incident laser beam, reflecting it at a right angle as shown in Fig. 5-1(a). The other setup is the normal incident configuration in which the laser beam is incident at a small angle less than 3˚, as shown in Fig. 5-1(b). The *o*-H_2 concentration is estimated to be the order of 1000 ppm or less.

Generally, the quality of a crystal made with deposition method is not as good as that made with a liquid epitaxial method in a cell. It is known that hcp structure is the most stable in a pure *p*-H_2 crystal, as described above, but also that a mixture of fcc and hcp poly-crystals or an amorphous is possible with the deposition method [67]. Annealing then greatly improves the crystal quality, and we had already confirmed our crystal quality in the previous work using a transparent BaF substrate through the study of CO/*p*-H_2 crystals [63]. But in the present work, using a metal mirror substrate with greater heat capacity, the check of this quality is necessary. For this purpose, we prepare a CH_4/CH_3F/*p*-H_2 crystal, because the direction of the *c*-axis in the hcp structure can be evaluated through the polarization dependence of the CH_4 spectrum. Momose *et al.* studied the rotationally resolved vibrational transitions with a crystal created by the epitaxial method in a metal cell and characterized the hcp structure and the direction of *c*-axis [39], showing that several transitions of ν_4 band of CH_4 at 1300 cm^{-1} are very useful in this respect. Therefore, we prepare *p*-H_2 crystal containing 0.4 ppm CH_3F and ~20 ppm CH_4, and observe the spectrum before and after the 7 K annealing using a laser polarization probe as well as an FTIR spectrometer [Bruker FTS 120HR] with a resolution of 0.01 cm^{-1}. The way of this experiment is described in Sec. 2.3. The results for surveying the axis of solid *p*-H_2 are described in the next section.

The intensity of each peak varied at the position in the crystal because the thickness of the crystal has a shape of thin convex lens profile. Moreover, the intensity of each peak varied with time [57],

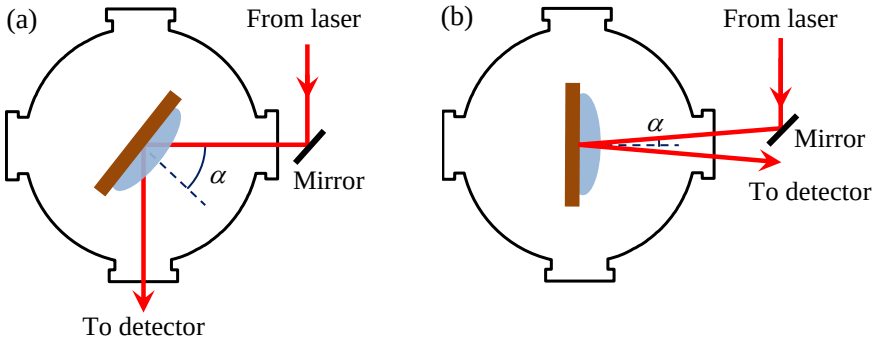

Fig. 5-1. The laser alignment for changing the incident angle α. (a) $\alpha = 45°$. (b) $\alpha \approx 0°$.

as described in Chap. 3. Therefore, the polarization dependence is measured at the same point in the crystal as quick as possible.

Figure 5-2 depicts a Cartesian coordinate system to describe an interaction of the light and molecules in the crystal. The *XY*-plane is set on the surface of substrate, and the *Z*-axis is normal to the substrate and is expected to be the *c*-axis of the hcp crystal. The laser beam is incident in the *XZ*-plane. The laser incidence angle α is defined by the angle to *Z*-axis. The laser polarization angle β is defined by the angle to *ZX*-plane, in other words, *p*-polarized light corresponds to $\beta = 0$ and *s*-polarized corresponds to $\beta = 90°$. θ is the orientation angle of CH_3F with respect to the *X*(*c*)-axis. Those angles are shown in Fig. 5-2.

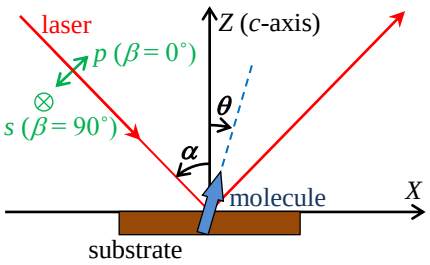

Fig. 5-2. Definition of the coordinate and angles. *XY*-plane: substrate surface. *Z*: normal line (*c*-axis), α : incident angle of the laser to *c*-axis of the hcp crystal, β : polarization angle of the laser to *Z* (*c*)-axis, θ : orientation angle of CH_3F to *Z* (*c*)-axis.

§ 5.3 Results

5.3.1 Evaluation of the *p*-H_2 crystal

For the confirmation of the crystal structure and its *c*-axis direction, the ν_4 band of CH_4 is used. The band region could be observed in detail clearly by high resolution spectroscopy as 0.01 cm^{-1}, as shown in Fig. 5-3. The trace (a) shows the spectra of before 7 K annealing. The absorption spectrum at 1302.5-1304.5 cm^{-1} corresponds to the *Q*(1) region. The attribution for each peak follows to the Ref. 39. The observed spectrum shows that some peaks come from different crystal structure, like at 1303.3 and 1303.6 cm^{-1} which correspond to the *Q*(1) transition of CH_4 in fcc and hcp structure, respectively. The peaks due to the crystal structure of fcc are marked with asterisk. The trace (b) describes the spectra after the 7 K annealing which is observed without polarizer. Comparison with before and after tells that the peak marked with asterisk disappears and the others remain and become much sharper. The conclusion is that the solid *p*-H_2 deposited on the cold substrate becomes hcp after 7 K annealing. It should be noted that the definition of hcp by this experiment is for macroscopic study, thus most parts of the crystal ought to be hcp structure by following the

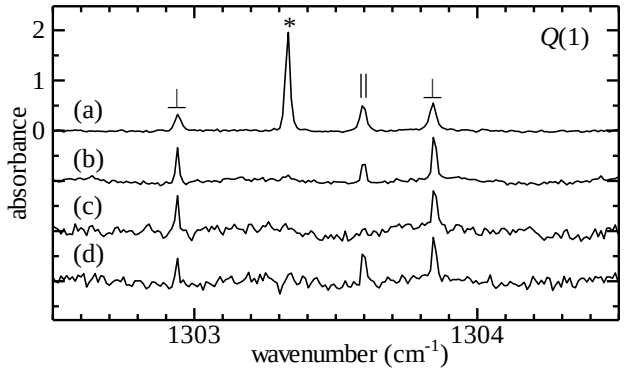

Fig. 5-3. The ν_4 absorption region of CH_4 in *p*-H_2 crystal. Trace (a) shows the sample before 7 K annealing. Trace (b) depicts the sample soon after 7 K annealing. Trace (c) and (d) are observed by perpendicular and parallel polarized light beam to the normal to the substrate, respectively. The label for each peak describes the direction of the transition moment to the *c*-axis. The peak due to the crystal structure of fcc is marked with asterisk.

experimental result. However, we cannot completely deny the possibility that the local structures around some CH_3F molecules have other crystal structure such as fcc.

Then, the direction of the hcp *c*-axis is investigated by polarization spectroscopy in the same regions. The traces (c) and (d) show the spectra observed by perpendicular and parallel polarized light beam to the normal to the substrate, respectively. Thus, the definition for the polarization of light follows to the Fig. 5-2. Each rovibrational transition spreads due to the crystal field in the hcp structure. For example, the *Q*(1) transition splits into several peaks due to the crystal field. One peak at 1303.60 cm^{-1} is assigned with parallel transition moment to the *c*-axis, and others at 1302.92 and 1303.82 cm^{-1} are assigned with perpendicular transition moment [39], as marked with in the upper one of Fig. 5-3. When the incident angle α of laser is set at 45° to the substrate, the parallel peak is not observed but the perpendicular peaks are observed at the β = 90° condition, that is to say, *s*-polarized. Similar results were also observed for other transitions. The parallel peaks are completely not observed when the polarization of light takes *s*-polarized however the perpendicular peaks are observed when the polarization of light takes *p*-polarized. The reason is that the incident angel α of laser is set at 45° to the substrate. The parallel component of light to the substrate is not able to be vanished as long as the incident angle has any angle except 90°.

From these experimental results, it is confirmed that the *p*-H_2 crystal on metal mirror substrate after 7 K annealing is an hcp crystal whose *c*-axis is normal to the substrate. This evaluation is based on the observation of absorption spectra of CH_4. Therefore, the sample crystal could have mosaic structure and some defections. The existence of such defections in the sample crystal which was made by the same way in this research was reported by analyzing the linewidth of CO in *p*-H_2

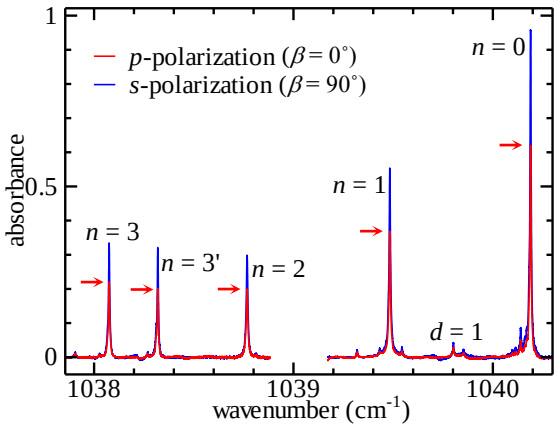

Fig. 5-4. Polarization dependence of the main series at the incident angle $\alpha = 45°$. Spectrum obtained in the *s*-condition is shown in blue and that in the *p*-condition is shown in red with arrows indicating the peak position.

crystal [63].

5.3.2. Polarization dependence of CH_3F in *p*-H_2 crystal

The polarization dependence of CH_3F in the *p*-H_2 crystal is measured by using QC laser spectroscopy. At the incidence angle of 45°, the intensities of absorption peaks change with the polarization angle *β*. Figure 5-4 shows the comparison of two spectra obtained in *p*- and *s*-polarization to the *c*-axis. The absorbance of each peak in the *s*-condition is larger than that in the *p*-condition by a common factor of 1.4.

It should be noted that the satellite peaks have the same intensity ratio as the main peaks. In Fig. 5-5, the spectrum of $n = 0$ satellite observed in the perpendicular condition is overlapped with one in the parallel condition with the same common factor of the main series. Good agreement of the two spectra indicates that the satellite peaks have the same polarization dependence.

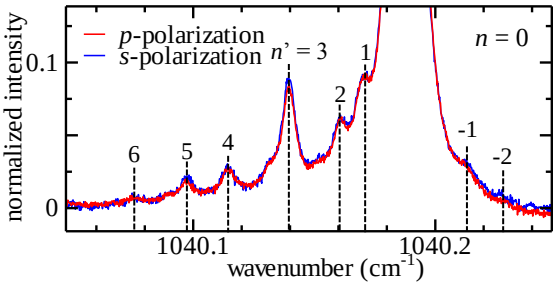

Fig. 5-5. The enlarged spectra of the satellite peaks beside $n = 0$ peak observed with the perpendicular and parallel conditions, where the intensity of the latter is normalized at $n = 0$ main peak of the former.

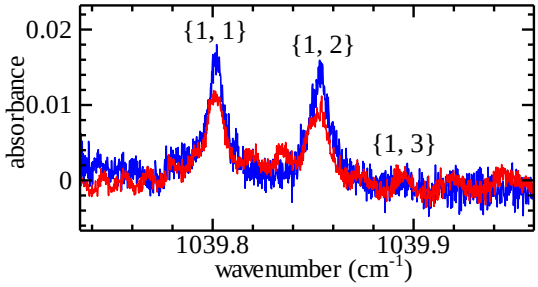

Fig. 5-6. Polarization dependence of the *d* series at the incident angle $\alpha = 45°$. Spectrum obtained in the *s*-condition is shown in blue and that in the *p*-condition is shown in red.

The unknown peaks are also observed between n = 0 and 1, named d. Since the peaks are discussed in Chap. 6, the labels for them are introduced briefly without the detailed explanation about them in this chapter. It is convenient to label those d peaks with a set of the number d and d' as {d, d'}. The type of parentheses for the d and d' series is used the different one to the n and n' series in order to compare the differences of them. In this manner, the d-th left peak is represented as {d, 1} peak and the numbers are arranged from left to right. By following the labeling rule, Fig. 5-6 shows the comparison of two spectra at {1, 1} and {1, 2} peaks obtained in p- and s- polarization to the c-axis. The absorbance of each peak in the s-condition is larger than that in the p- condition by a common factor of about 1.4. {1, 3} peak looked like to be observed, but the intensity is too weak to analyze. The d' series of d = 2 are also observed but the intensities are so weak.

5.3.3. Incidence angles dependence of the polarization

In order to get more information on the alignment of CH_3F, the polarization dependence of the main series was studied by changing the β angle in 10˚ steps. The result at the incident angle of 45° is shown in Fig. 5-7(a), whose vertical axis is normalized by the maximum intensity of each n-th peak. All n-th peaks show a similar profile with a maximum value at β = 90° and minimum values at β = 0° and 180°.

In case of larger molecules which cannot rotate freely, the alignment of a molecule becomes the subject of discussion. CH_3F may be an intermediate case, in which the rotational motions are hindered except for the one around the C_3-axis. Supposing that the C_3-axis is locked firmly along the

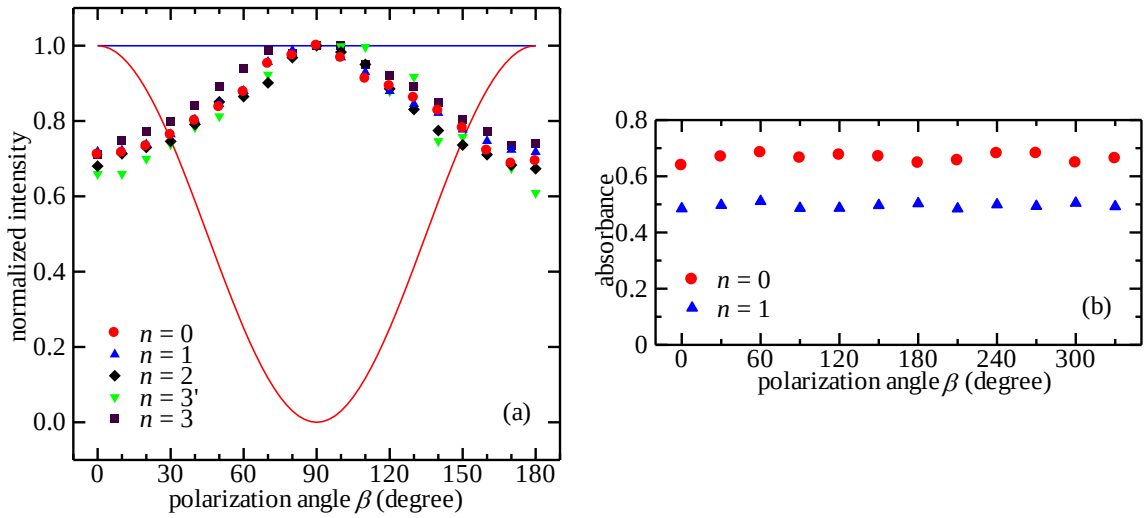

Fig. 5-7. (a) The normalized polarization dependence of the absorption peak of the main series at the incident angle α = 45°. The two traces are calculation results to the model for CH_3F locked in the c-axis (red) and random orientation (blue). (b) The polarization dependence at the incident angle α = 0°.

c-axis, then the absorbance would be smallest at $\beta = 90°$, as shown by the red trace in Fig. 5-7(a). But the experimental result is opposite to this. Or, supposing that the orientation of CH_3F is completely random in the crystal, then no polarization dependence would be observed like shown by the blue trace in Fig. 5-7(a). The experimental result at the 45° incident angle condition eliminated these two extreme cases of the orientation. That is to say, CH_3F does not orient completely to the *c*-axis, nor has it completely random orientation in the crystal.

On the other hand, when the incident angle α is set to 0°, the polarization dependence disappears as seen in Fig. 5-7(b). This result suggests that the orientation of CH_3F is somehow isotropic around the *Z*-axis.

§ 5.4 Discussion

The alignment of the rotational axis of molecules in *p*-H_2 crystal has been studied for some small molecules which can rotate in the crystal. For example, with the CO molecule, the $J = 1$ state splits into M (= J_z) = ±1 and 0 components due to the crystal field [63]. The rotational term value of the doubly degenerate $M = \pm 1$ states is lower than that of the $M = 0$ state by 1 cm^{-1}. This means that the rotational axis of the $M = \pm 1$ state has a polar angle of ±45° with respect to the *c*-axis, and that this molecular axis rotates in its perpendicular plane. Meanwhile, the $M = 0$ rotational axis lies in the *XY*-plane and then the molecular axis rotates in a perpendicular plane which involves the *Z*-axis. Therefore, the molecular axis does not align at all, however, the fact that the $M = \pm 1$ states have a lower term value than that of $M = 0$ suggests that it is easier to rotate in the ±45° angle plane than in the plane involving *Z*-axis.

5.4.1. Alignment of CH_3F in the crystal

The behavior of the β dependence in Fig. 5-7 suggests that CH_3F does not orient completely to the *c*-axis, nor has it completely random orientation in the crystal. Furthermore, the C_3-axis is more likely to orient in the *XY*-plane rather than to the *Z*-axis. Meanwhile, the 0° incident angle experiment suggests that the projection of the C_3-axis on *XY*-plane looks somehow isotropic around *Z*-axis. The quality of the solid *p*-H_2 in this research was checked by observing the spectrum of CH_4 and the local structure of solid *p*-H_2 around CH_4 is good, as mentioned in Sec. 5.3.1. However, the quality to the *XY*-plane is not checked.

In order to explain the result of the polarization experiments, we introduce a simple model in which

CH_3F orients to the *c*-axis with a polar angle of θ, at which the interaction energy between CH_3F and the crystal is minimized. This means that the orientation of CH_3F is determined by a vacant space of a lattice defect in the crystal. The shape of the ventricular space is geometrically determined by the position of 12 nearest neighbor sites of the hcp structure. The nearest neighbor sites make eight equivalent triangles and six squares as shown in Fig. 5-8. There are six line segments which connect the center of the triangle and square face each other across, and one more line segment which connects the center of the pairing triangles along the *c*-axis. The length of the line segment of the triangle-square is larger than that of the triangle pair. The polar angle of these axes to the *c*-axis is 63.5°. One can visualize a six-way vacant space which is built up by these axes for storing the CH_3F molecule along one of the triangle-square axes. This model is based on this six-way vacant space, except for not fixing the polar angle to 63.5° but rather treating it as an arbitrary angle θ. Therefore, the six orientation vectors of CH_3F in the crystal are expressed as below by using Cartesian coordinate (*X*, *Y*, *Z*).

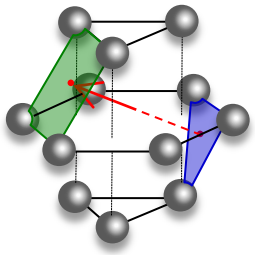

Fig. 5-8. The image of hcp structure of *p*-H_2 crystal. The first nearest sites of *p*-H_2 have eight triangles like blue color one and six squares like green color one.

$$(\sin\theta\cos\gamma, \sin\theta\sin\gamma, \pm\cos\theta),$$

$$\left(\sin\theta\cos\left(\frac{2}{3}\pi+\gamma\right), \sin\theta\sin\left(\frac{2}{3}\pi+\gamma\right), \pm\cos\theta\right), \qquad (5-1)$$

$$\left(\sin\theta\cos\left(\frac{4}{3}\pi+\gamma\right), \sin\theta\sin\left(\frac{4}{3}\pi+\gamma\right), \pm\cos\theta\right)$$

in which γ means an arbitrary angle between *X* and *a*-axis of hcp structure. The sign of the *Z* component means that three triangle-square axes are positive and the other three are negative. Note that the transition dipole moment vector $\boldsymbol{\mu}$ of the ν_3 band coincides with the C_3 symmetry axis. Meanwhile, the polarization vector of the laser beam with incident angle α passing through the *XZ*-plane is expressed as below.

$$(\cos\alpha\cos\beta, \sin\beta, \sin\alpha\cos\beta) \qquad (5-2)$$

As absorption intensity is represented as $|\boldsymbol{\mu}\cdot\boldsymbol{E}|^2$, the peak intensity is proportional to the squares of the inner product between equations (5-1) and (5-2). By summing up all the contributions of the six terms, the intensity is represented as a function of α, β and θ as follows by using the equivalence of

a- and *b*- crystal axes.

$$f(\alpha,\beta,\theta) \propto \sin^2\theta\cos^2\alpha\cos^2\beta + 2\cos^2\theta\sin^2\alpha\cos^2\beta + \sin^2\theta\sin^2\beta \qquad (5-3)$$

The arbitrary angle γ between X and a-axis of hcp structure is vanished. If the solid p-H_2 in this research has mosaic structure as mentioned above, the possible to change the arbitrary angle γ in this sample crystal could not be denied. However if each part of single crystal has a certain amount of CH_3F molecules, the polarization dependence would be analyzed by using Eq. (5-3) since it does not have the arbitrary angle dependence. In case of incidence angle $\alpha = 0°$, Eq. (5-3) becomes

$$f_{\alpha=0}(\beta,\theta) \propto \left(\sin^2\theta\cos^2\beta + \sin^2\theta\sin^2\beta\right) = \sin^2\theta \qquad (5-4)$$

Thus, no polarization angle dependence is expected. The experimental result at the incident angle of 0° is consistent with it and indicated that the CH_3F orientation angle θ is not 0°, as shown in Fig. 5-7(b).

In case of the incidence angle $\alpha = 45°$, Eq. (5-3) becomes

$$f_{\alpha=45}(\beta,\theta) \propto \sin^2\theta\cos^2\beta + 2\cos^2\theta\cos^2\beta + 2\sin^2\theta\sin^2\beta \qquad (5-5)$$

Thus, the unknown parameter θ can be determined using fitting analysis with the observed polarization function $f^{obs}_{\alpha=45}(\beta)$. As an example the result of the fitting for n = 0 is shown in Fig. 5-9. This simple model for the fitting analysis is adequate to explain the experimental result and succeeded in drawing the polar angle θ. The value of θ determined by least square fitting is 64.9(3)°. In Fig. 5-9, the green and blue lines indicate the result when the value of polar angle θ is fixed at 60 and 70°. The value in the parentheses is the 1σ statistical error, including systematic error due to an uncertainty in the incidence angle of α (±3°). It is interesting and perhaps a little surprising that this value is in good agreement with the value of 63.5° used in the original six-way triangle-square model, which only considers the geometric shape

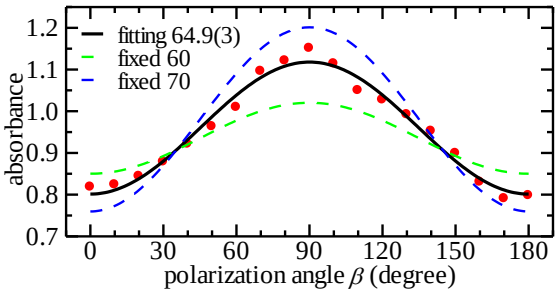

Fig. 5-9. Comparison of the experimental result of n = 0 peak and the model function (5-5), in which the incident angle α is fixed to 45° and θ is determined by least square fitting.

of the vacant space. In the case of CO_2 in *p*-H_2 crystals, there was theoretical work based on the interaction potential analysis using *ab initio* calculations [35]. CO_2 in the crystal occupies a potential with three-fold symmetry and takes the minimum energy at a polar angle of 51.3°. The difference between CH_3F and CO_2 might come from the size of the molecules. The molecular length of CO_2 and CH_3F based on Van der Waals radius are 5.12 and 4.73 Å, respectively. CO_2 might be a little long to store in the six-way vacancy.

5.4.2. Conformation of the accuracy for fitting function

In order to check the accuracy of the assumption for making the fitting function, one parameter and one term are added for Eq. (5-3). The new fitting function is below,

$$f(\alpha,\beta,\theta,C) \propto \left(3\sin^2\theta\cos^2\alpha\cos^2\beta + 6\cos^2\theta\sin^2\alpha\cos^2\beta + 3\sin^2\theta\sin^2\beta + 2C\sin^2\alpha\cos^2\beta\right) \quad (5-6)$$

The final term of Eq. (5-6) describes that the effect of CH_3F molecules whose C_3-axis is along the *c*-axis. The coefficient *C* shows the ratio of the CH_3F molecules locked along *c*-axis. At the fitting analysis, if *C* and θ were set to the running parameters, these values were not determined; therefore, the coefficient *C* is fixed from 0 to 0.7. The determined θ values at each *C* value are shown in Fig. 5-10. The statistical error increases with increasing the *C* value. The standard deviations for the residual error to the experimental result from fitting results are described in Fig. 5-11. The vertical axis plots to the root mean squared error (RMSE). The RMSE increases with increasing the *C* values. From Fig. 5-10 and 5-11, the coefficient *C* should be 0, thus almost all CH_3F molecules are not along to the *c*-axis of *p*-H_2 crystal. The approximation for the model which is based on the six-way vacant space, as mentioned above, would be reasonable for this fitting analysis.

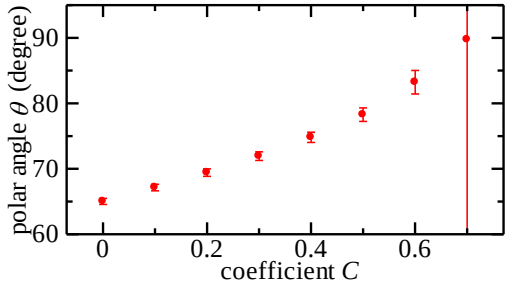

Fig. 5-10. The relation between fitting parameter θ and coefficient *C* which describes the ratio of CH_3F that aligns along to the c-axis. The error-bar shows the 1σ by determined in the fitting analysis.

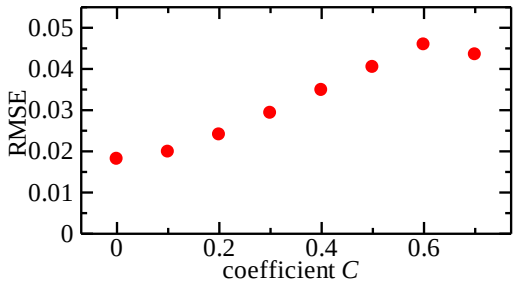

Fig. 5-11. The Root Mean Squared Error (RMSE) to the coefficient *C*. *C* describes the ratio of CH_3F molecules that align along to the *c*-axis.

5.4.3. Polarization dependence in n = 1, 2, 3, 3'

The values of θ for n = 1, 2, 3, and 3' are also determined by the fitting analysis and the results are shown in Fig. 5-12, in which each point presents the values with the error bar. The values for n = 0, 1, 2, and 3 are almost same, which suggests that the number of o-H_2 molecules in the first nearest neighbor sites does not affect the orientation of CH_3F in the crystal. However, it should be pointed out that the value of 67.5(5)° for n = 3' looks different from others beyond the error bars. The label n = 3' does not have physical implications, but just indicates the neighbor of the "regular" n = 3 peak of the main series. However, its temporal character has been noticed to be different from the other main and satellite series, since the intensity of the n = 3' peak increases with time in the cooled environment unlike the other main peaks [57]. Thus the nature of n = 3' might be fundamentally different, for example, it might be CH_3F in solid p-H_2 with fcc structure, as discussed in Chap. 3.

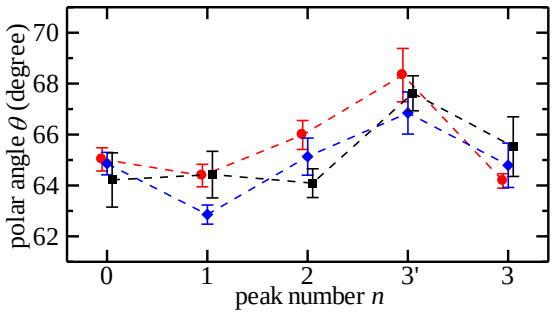

Fig. 5-12. The polar angle θ determined by the fitting at three different points of the crystal. The horizontal axis shows the labels of peaks in the main series. Each point in the same color is a series of measurement in the same position in the crystal. The error-bar of each point does not include systematic error.

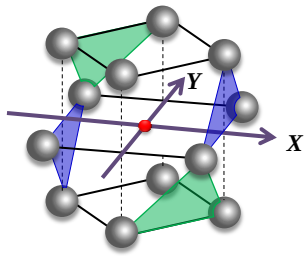

Fig. 5-13. The image of fcc structure of p-H_2 crystal. The first nearest sites have eight triangles as blue color one and eight triangles as green color one.

The alignment of CH_3F cluster in fcc structure would also like to be estimated by the similar model function. The image of the fcc structure is depicted in Fig. 5-13. The polarization vector of the laser beam with incident angle α is same definition for Eq. (5-2). The vectors of CH_3F molecules can be divided into two patterns. One is four line segments which connect the center of the pairing blue triangles in Fig. 5-13, and the other is also four line segments which connect the center of the pairing green triangles. We assume that the alignment of CH_3F should be firmly locked on these lines, the CH_3F orientation angles θ_1 for blue triangles and θ_2 for green triangles are estimated 71.57° and 54.74°, respectively. Therefore, the four orientation vectors of CH_3F molecules in the crystal are expressed as below by using Cartesian coordinate (X, Y, Z).

$$(\sin\theta_1, 0, \pm\cos\theta_1), \left(\frac{\sqrt{2}}{2}\sin\theta_2, \frac{\sqrt{2}}{2}\sin\theta_2, \pm\cos\theta_2\right), \\ (0, \sin\theta_1, \pm\cos\theta_1), \left(-\frac{\sqrt{2}}{2}\sin\theta_2, \frac{\sqrt{2}}{2}\sin\theta_2, \pm\cos\theta_2\right) \qquad (5-7)$$

The peak intensity is proportional to the squares of the inner product between equations (5-2) and (5-7). By summing up all the contributions of the eight terms, the fitting equation becomes the below,

$$f(\alpha,\beta,d) \propto \left(\cos^2\alpha\cos^2\beta + \sin^2\beta\right)\left\{d\sin^2\theta_1 + (1-d)\sin^2\theta_2\right\} \\ + 2\sin^2\alpha\cos^2\beta\left\{d\cos^2\theta_1 + (1-d)\cos^2\theta_2\right\} \qquad (5-8)$$

The coefficient of d describes the ratio of the type for the alignment of CH_3F. If the value of d is over 0.5, the alignment of CH_3F would be much easier to stay on the line which connects the center of the pairing blue triangles in Fig. 5-13. The values for θ_1 and θ_2 are fixed to the values that are calculated and the incidence angle α = 45° is also fixed. The fitting results for n = 3 and 3' are depicted in Fig. 5-14. The d value are estimated 0.62(2) and 0.85(5) for n = 3 and 3', respectively. The results would indicate that the alignment of CH_3F would be much easier to stay on the line which connects the center of the pairing blue triangles in Fig. 5-13. However, the fitting function for fcc structure can also represent the polarization dependence of n = 3 well. The independent variable for Eq. (5-8) is only β, in addition to it, the term including the coefficient d could be treated as a proportionality constant. Equation (5-8) becomes the function follows to,

$$f(\beta) \propto A + B\sin^2\beta \qquad (5-9)$$

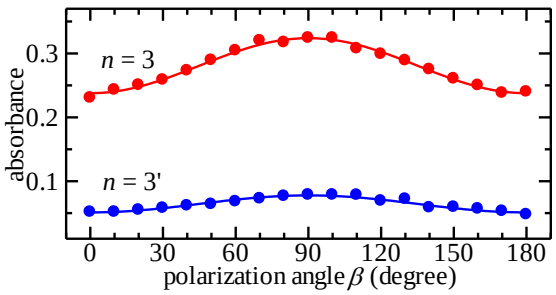

Fig. 5-14. Comparison of the experimental result of the n = 3 and 3' peaks and the model function (5-8) for fcc, in which the incident angle α is fixed to 45°.

Thus, the essential meaning of the fitting function for hcp: Eq. (5-3), and that for fcc: Eq. (5-8), are the same. From these result, the analysis to the polarization dependence with the fitting function for the fcc model can work, however the origin of each peak cannot be determined by only this analysis.

5.4.4. Polarization dependence of the satellite peaks

The polarization dependence gives one of the important information on the identity of the satellite peaks. As seen in Fig. 5-5, the polarization dependence is the same as that of the main peaks. If the satellite peaks were *M* splitting caused by the crystal field, a polarization difference would have been observed among the satellite peaks. But the fact of no difference in the polarization experiment eliminates this assumption likes Fig. 5-5, and thus supports the previous cluster model consisting of CH_3F and *o*-H_2 in the second nearest neighbor sites [61], as discussed in Chap. 4. The same polarization dependence means that the polar angle is also same. If this interpretation is right, it can be concluded that the alignment of CH_3F does not depend on the number of *o*-H_2 molecules in the first and second nearest neighbor sites.

5.4.5. Polarization dependence of the *d* series

The polarization dependences of the *d* series are also observed only at {1, 1} and {1, 2} as described in Fig. 5-6. Figure 5-15 shows the polarization dependence of the *d* series. As shown in Fig. 5-6, the peak intensities of the two peaks are dispersed since the observed spectrum has not good S/N. The fitting analysis by least square fitting with function (5-5) estimates that the polar angle θ for them and the values of θ for {1, 1} and {1, 2} are 68.6(42)° and 67.0(17)°, respectively. These values were a little bigger than the *n* main series and similar with the *n* = 3' peak. The physical implication of it has not defined yet. The origin of the *d* series is discussed in Chap. 6.

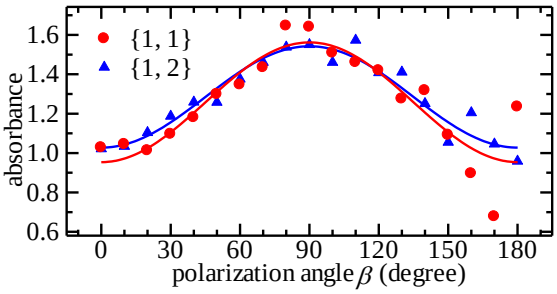

Fig. 5-15. The fitting results to the experimental result of {*d*, *d'*} = {1, 1} and {1, 2} by using the model function (5-5).

§ 5.5 Conclusion

The polarization dependence of the ν_3 vibrational transition of CH_3F, whose rotational motion is hindered in *p*-H_2 crystal, was observed. The experimental results were well explained by a simple six-way vacancy model and the alignment angle in the crystal is determined. The CH_3F is not aligned along the *c*-axis but tilted to 64° from the *c*-axis. This is the first time to estimate the

alignment of dopant molecule in solid *p*-H_2 by experimentally. The method to estimate the alignment of the dopant can be used for other dopant molecules. As mentioned above, the knowledge of the orientation of the dopant molecules is very important. For example, the surveys which need to switch the direction of dopant molecules should know the alignment of the dopant. This result could contribute to such kind of researches which use the direction of dopant molecules. Furthermore, by using this experimental way, a new physical phenomenon could be found. As mentioned above, CH_3F molecule is in the group which cannot rotate in solid *p*-H_2. The fact that CH_3F is not aligned along the *c*-axis was found in this research. However, the alignments of the other dopants which cannot rotate in solid *p*-H_2 have not been surveyed yet. Therefore, a new physical phenomenon could be found when the dopant which is aligned along the *c*-axis of solid *p*-H_2. The experiments for other dopant are desired.

The satellite peaks also has the same polarization dependence with the *n* main peaks. The polarization dependences to the unknown peaks named *d* were also observed. The alignment angles of them were also estimated. From these results, the origin of the *d* series would relate to CH_3F.

This result should be verified with more precise theoretical calculation based on molecular interaction of CH_3F and H_2. We hope the alignment of molecules in *p*-H_2 crystal will be elucidated from this experimental approach and theoretical approach in the future.

Chapter 6 The structural change by pumping

§ 6.1 Introduction

Pump-probe spectroscopy, one of the spectroscopic experimental ways, is sometimes called Time Resolved Spectroscopy (TRS). It is often used for understanding the mechanism of chemical reaction to the light with time. In general, the lasers used in TRS are pulse lasers. The basic technic of this experiment was introduced in session 11.4 of Ref. 91. Firstly, one pulse laser beam that is called pumping laser excites the target sample. Then, the other pulse laser that is called probing laser passes through or reflects at the sample with the delay time from the pumping beam. The probing laser observes the condition of the target sample at that time. The information by the probing beam changes with each delay time from the pumping beam and the changes correspond to the relaxation process from the excited state to ground state or the process of the chemical reaction. In these experiments, the time resolution is necessary and it depends on the width of the both laser pulses. The pump-probe spectroscopy is popular in the visible and middle infrared region since many pulse lasers have been developed for these regions. On the other hands, pump-probe spectroscopy for the near infrared region was not popular until several years ago since the development of the pulse lasers for this region was later than that for other regions.

In the previous study, our laboratory reported the photochromic phenomenon to the CH_3F cluster with *o*-H_2 in solid *p*-H_2 by using cw QC laser [58]. By irradiating of one cluster's peak at about 10 mW, the peak was bleached and some other peaks increased. And the reversible phenomenon was also observed. It would indicate that the *o*-H_2 which stays in the first nearest neighbor site of CH_3F is migrated by the thermal energy that is released from the vibrational energy of CH_3F by the pumping laser. Thus, the spectral changes are the changes of the cluster size, thus we observe the structural changes of the clusters. The QC laser beam can bleach the almost all cluster peaks, like the $n = 1$ main peak or the satellite peak of $n = 0$.

However, by using one QC laser, we only observe the before and after spectra by the pumping. It means that the ongoing process of the migration is not able to be analyzed. If the process of the photochromic phenomenon is observed, the understanding of this mechanism could be promoted and the origins of some unknown peaks, as labeled with *d*, could be identified. In this research, the real

time monitoring of pump-probe experiments by using two cw-QC lasers is attempted.

§ 6.2 Experimental details

The experimental setup is mentioned in Section 2.2.3. The concentrations of *o*-H_2 and CH_3F at this sample are around 1000 ppm and 0.4 ppm, respectively.

The pumping beam is set at the wavenumber of one target peak and irradiates it by a continuous wave. In order to monitor the change by the pumping in the real time, the two laser beams are completely overlapped by the grid polarizer at the front of the cryostat. Each peak of the *n* series is pumped in this experimental way. In order to investigate the pumping power dependence, the intensity changes of each cluster peak by bleaching the $n = 1$ peak are observed with changing the pumping powers. For changing the pumping powers, the number of attenuators for the pumping laser beam is changed.

§ 6.3 Results

Before to describe and analyze the experimental results, it should be pointed out that the mechanism of the pumping has not been clearly identified yet. In general, the pumping of the target peak means that the laser beam with the resonant frequency to the target cluster irradiates to the target. Therefore, the target cluster at the grand state is excited to an excited state. One of the results after the excitation is that the vibrational energy is released to the crystal lattice as a phonon with keeping the cluster structure and returns to the grand state. This phenomenon would be the main process. This is observed in the absorption spectrum by the probing beam whose power is weak enough and, moreover, their frequency is swept. Another result after the excitation is that the structure of the cluster is changed. Thus, the *o*-H_2 in the cluster is migrated to farther sites from the CH_3F. It could be checked from the pump-probe experimental results. One possible mechanism of the pumping would be that the *o*-H_2 in the cluster is migrated to other sites by getting thermal energy from the vibrational energy of CH_3F. The main mechanism of the migration of *o*-H_2 by the pumping would not be the one due to intermolecular interchange and to resonant *ortho-para* conversion, as discussed in Chap. 3. The potential energy between each site of *p*-H_2 crystal was theoretically calculated and estimated about 30 K [17]. This value is, of course, for *p*-H_2 crystal and not for the potential energy of CH_3F and *o*-H_2 in *p*-H_2. The potential energy between CH_3F and *o*-H_2 in *p*-H_2

crystal could be higher than this. Even so, the vibrational energy of CH_3F is around 1500 K, and it is enough for *o*-H_2 to migrate.

The difference between the probing beam and the pumping beam is only about the laser power, thus the number of the photons to one peak are different. The difference of the number of photons affects the interval between the excitations. If the migration rate of *o*-H_2 is proportional to the number of photons, the decay time of the peak intensity which is pumped would be inversely proportional to the pumping power. On the other hand, if the decay time is not so, some phenomenon could change the interval of the absorption by the cluster. In such case, one possible case is that the local temperature around the pumped cluster could affect the mechanism of the migration by the pumping. In order to check the mechanism for the pumping, the pumping power dependence is observed and the results are discussed in section 6.3.4 and 6.4.3.

6.3.1 Rapid scan data

The rapid scan experimental results are shown in Fig. 6-1. Figure 6-1(a) shows the spectrum that is measured for 20 seconds to the frequency region in which the n = 0 and 1 peaks are observed. The vertical and horizontal axes correspond to the intensity of the probing beam detected by an AC coupled detector (MCT) and data points saved by the oscilloscope, respectively. The total data points are 10^7 and recording time is 20 sec, and the sweep frequency of laser is 100 Hz. Therefore, one scan takes 10 ms and the data points per one scan are 5000 points, as described in Fig. 6-1(c). The red and green traces in Fig. 6-1(c) show the absorption spectrum and etalon signal for the wavelength calibration, respectively. The observation range is determined about 1 cm^{-1} from the etalon signal. Thus, the resolution becomes

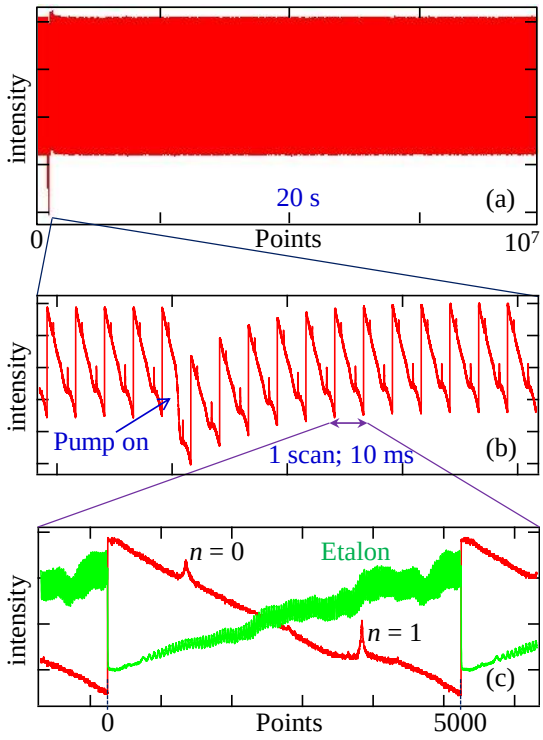

Fig. 6-1. The spectra observed by the rapid scan. (a) The absorption spectrum recorded for 20 sec. The horizontal axis shows the data points. (b) The expanded spectrum at the time when the pump starts. (c) One scan data of absorption spectrum. The frequency region is ~ 1 cm^{-1} in which the n = 0 and 1 peaks are observed. The red and green traces show the signal of absorption spectrum and etalon, respectively.

about 3×10^{-4} cm^{-1} after calibration, and the frequency resolution and signal to noise ratio are sufficient to analyze the peak intensity of each cluster peak. In order to discuss the change by the pumping, the shutter is closed to cut the pumping beam for about initial 1 second. Then, at the point described "Pump on" as seen in Fig. 6-1(b), the shutter is opened and the pumping beam keeps the irradiation. The probing laser beam is detected by the MCT detector that is an AC coupled detector. At that time when the shutter is opened, a few period of probed signal is affected by the pumping laser. The mean level of the probed spectrum decreases instantaneously, and returns to the original level before starting the pumping. It is because the pumping beam is not completely blocked by the final grid polarizer and the residual pumping laser affects the probing spectrum. However, the effect cannot be any problems since the pumping beam is a continuous wave without any sweep frequencies. That's why, the center of the triangle wave of probed spectrum returns to the same level before starting the pumping. The time of starting to irradiate the pumping beam can be determined from this instantaneous variation of the probed spectrum with the order of 10 ms.

The observed absorption spectra are converted to absorbance in order to discuss the population change of each cluster. The converted way of the spectra is the same with the one that is introduced in Sec. 2.2.1. The S/N of each segment spectrum is not enough for analyzing especially for weak peaks such as the *d* series. For detailed analysis, 10 or 100 scans data are averaged for the spectra which are converted to each absorbance spectrum.

6.3.2 Pumping of $n = 0$

Figure 6-2 shows the spectral change for the range of the $n = 0$ and 1 peaks by pumping of the $n = 0$ main peak. The pumping power is estimated about 2 mW. The black trace depicts the initial spectrum and the red trace shows the spectrum at each time from starting the pumping. Figure 6-2 describes that the population of the $n = 0$ main peak transferred to the $n = 1$ main peak. The main peak of $n = 0$ after the pumping becomes narrower than before, as comparing black and red trace in Fig. 6-2. On the other hand, the $n = 1$ main peak does not become wider. This result is, of course, the same with the result as Fig. 4-7. As mentioned above, it would mean that the main peak is formed by many types of clusters, like CH_3F and some *o*-H_2 molecules in above third sites. The peak shape which still remains at the main peak position after pumping of $n = 0$ might be the signal from isolated CH_3F in pure *p*-H_2 crystal since the other clusters are transferred to other peaks such as the $n = 1$ main peak. Based on this estimation, all *n* peaks are also originated by the same mechanism for the $n = 0$ main peak. The linewidth of the $n = 1$ main peak is kept after pumping of $n = 0$ since the

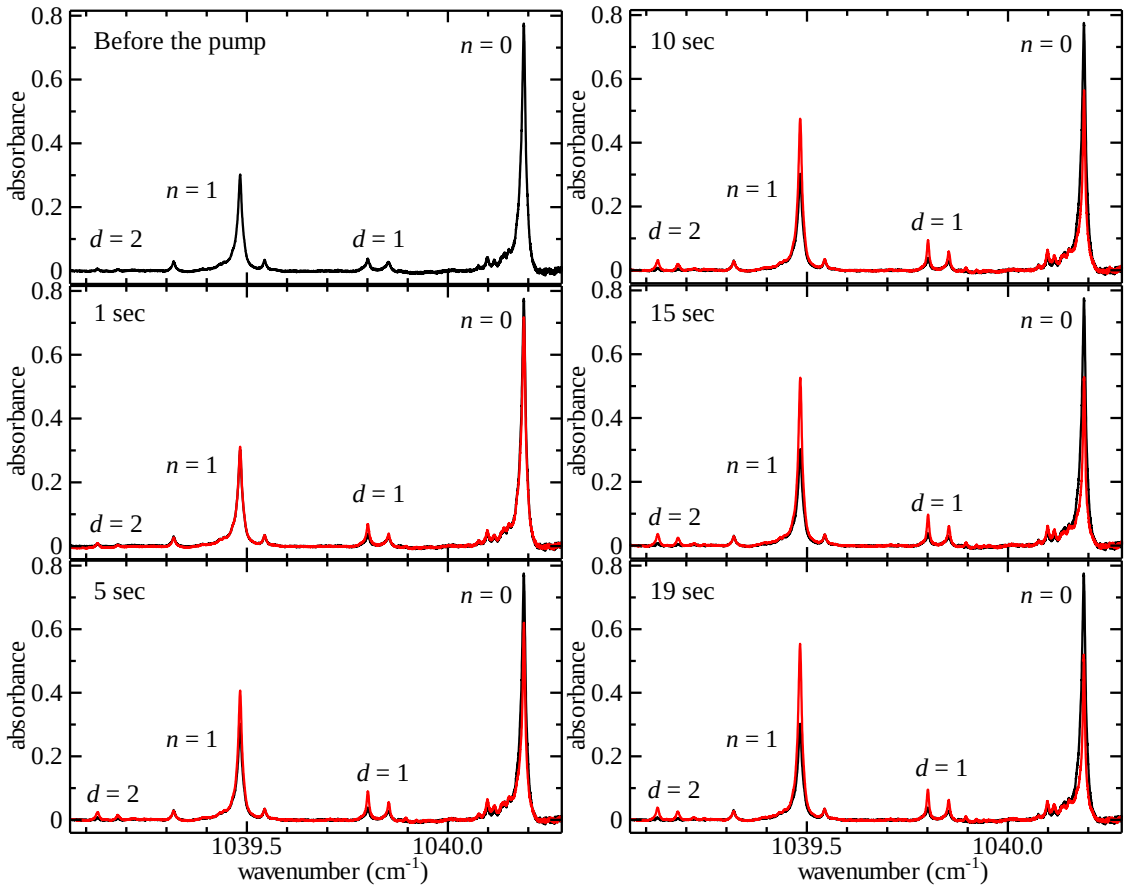

Fig. 6-2. The temporal behaviors of the absorption spectrum by the continuous pumping of $n = 0$. The pumping power is 2 mW. The black and red traces show the absorption spectrum before the pumping and spectra at the irradiated time of the pumping beam, respectively. The pumping times are shown on the upper left of each figure.

components are the same between before and after.

The population change by pumping of $n = 0$ does not only appear to $n = 1$, also $n = 2$ or 3, as described in Chap. 4. In addition to the n series, the d series are also changed their intensities. Figure 6-3 depicts the change of the peaks. (a) and (b) depict the spectra at $d = 1$ and 2, respectively. The d series named $d = 1$ and 2 increase with pumping of the $n = 0$ main peak. The existences of these peaks are reported in the previous research [57], however, the origin and the character have not been revealed yet. The main issue for them is their weak intensities. The intensities of these peaks increase with pumping of the n series, however without the pumping, their intensities decrease and only one or two peaks of them are observed. In this study, the d series are clearly observed and the characters of them are surveyed for the first time. The summary for the d series is described in Sec. 6.3.5. It should be noted that both $d = 1$ and 2 has very similar characters, like the number of the peaks and the intensity distributions in each series.

The behavior of d = 1 by pumping of n = 0 is a little different from d = 2. By pumping n = 0, d = 1 increases quickly and soon becomes saturated, on the other hand, d = 2 increases slower. From this result, one possible expectation is that if the n = 1 peak is pumped, d = 2 would increase more quickly and d = 1 would increase more slowly. This expectation is checked and the result is shown in next session. The four peaks observed at each d = 1 and 2 series make similar temporal behaviors. Each peak would increase similar rate, thus the relative intensities are roughly kept. One peak between {2, 1} and {2, 2} is observed. It is observed at d = 2, but is not observed at d = 1.

By comparing the two figures of Fig. 6-3, the offset position of each peak in the d = 1 and 2 series correlates well. Therefore, it is convenient to label those d peaks with a set of the number d and d' as {d, d'}, as described in Chap. 5. The type of parentheses is used the different one to the n and n' series in order to compare the differences between them. In this manner, the d-th left peak is represented as {d, 1} peak and the numbers are arranged from left to right. The peak appears at the position between {2, 1} and {2, 2} is not included the d' series.

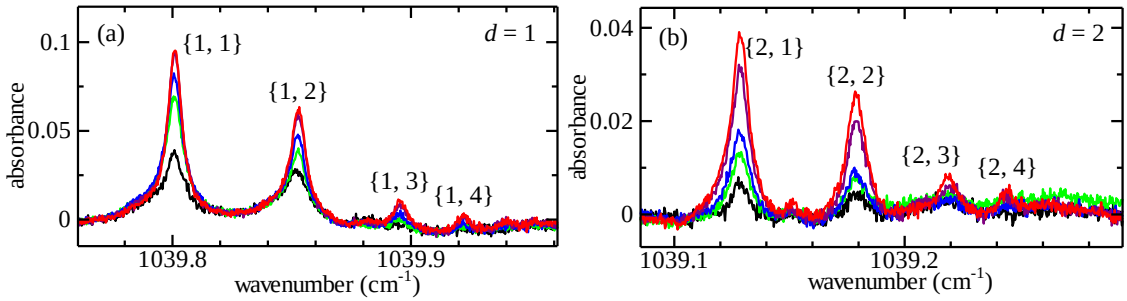

Fig. 6-3. The temporal behaviors of (a) d = 1 and (b) d = 2 series by pumping n = 0. The spectrum observed before the pumping (black), and after the beginning of the pumping 1 sec (green), 2 sec (blue), 10 sec (purple), 19 sec (red) after starting the pumping, respectively.

6.3.3 Pumping of n = 1

Figure 6-4 shows the spectral change by pumping of n = 1. The pumping power is about 5 μW. As mentioned in Chap. 4, the n = 1 main peak is bleached and the satellite peaks of n = 0 increase by pumping of n = 1. Few populations are transferred to the n = 2 and n = 3 peaks by pumping of n = 1, as mentioned in Chap. 4. The main peak of n = 0 also increases, but almost all populations are transferred to the satellite peaks of n = 0. This mechanism would be that one o-H_2 in the first nearest neighbor site of the n = 1 cluster transfers to the second nearest neighbor site and the structure becomes the cluster of CH_3F and o-H_2 molecule in its second nearest site. The cluster structure corresponds to the satellite peak of n = 0. However, the number of o-H_2 molecules cannot be

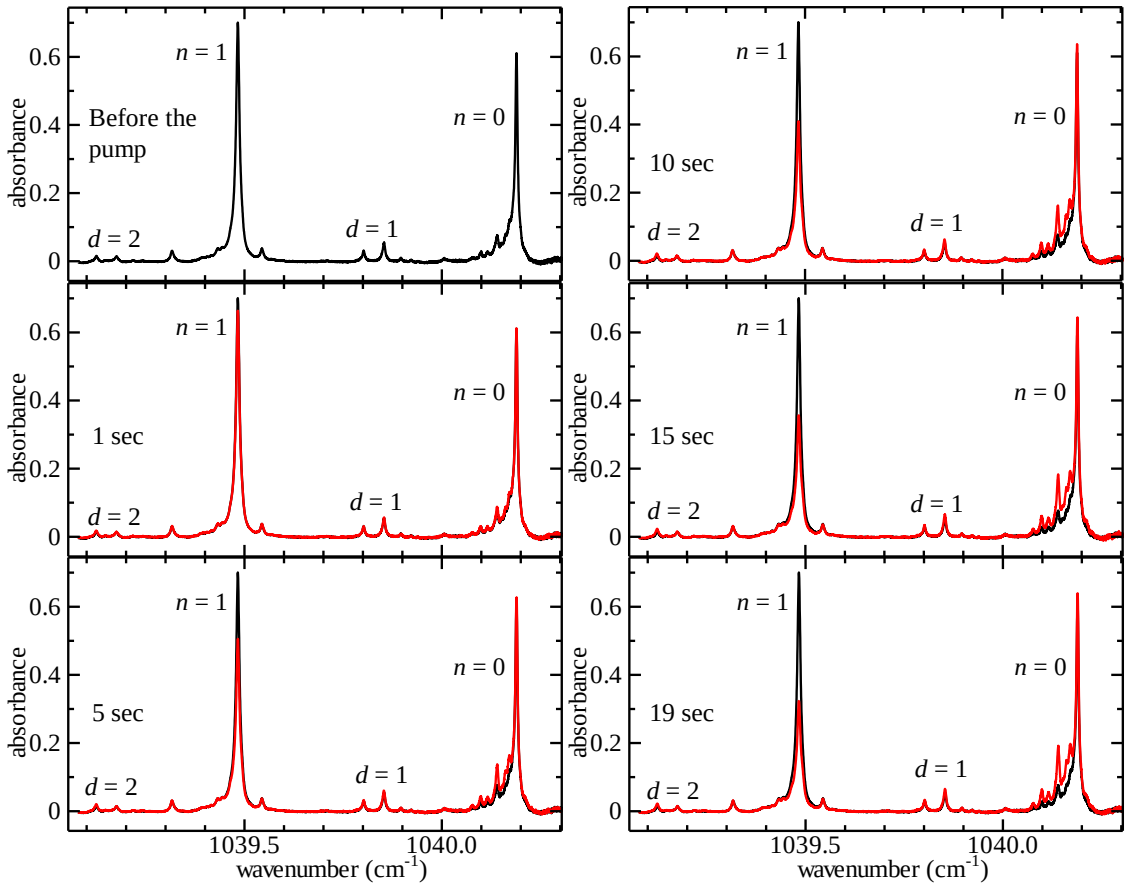

Fig. 6-4. The temporal behaviors of the absorption spectrum by the continuous pumping of $n = 1$. The pumping power is 5 μW. The black and red traces show the absorption spectrum before the pumping and spectra at the irradiated time of the pumping beam, respectively. The pumping times are shown on the upper left of each figure.

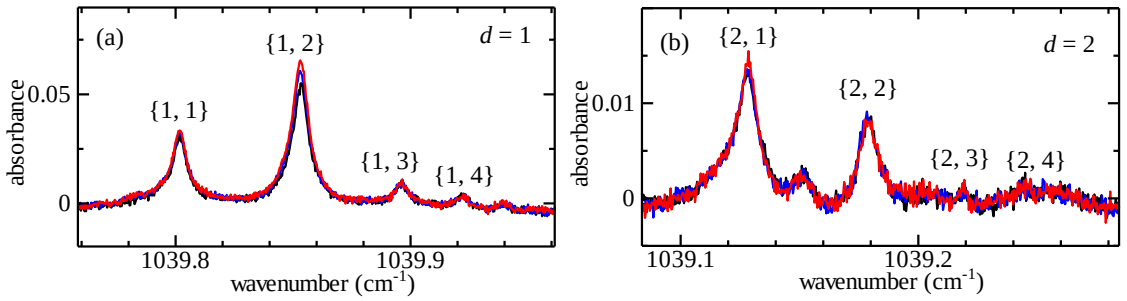

Fig. 6-5. The temporal behaviors of (a) $d = 1$ and (b) $d = 2$ series by pumping $n = 0$. The spectrum observed before the pumping (black), and after the beginning of the pumping 5sec (blue), 19 sec (red) after starting the pumping, respectively.

explained by only considering *o*-H_2 in the first nearest neighbor site since the experimental results show that all satellite peaks increase.

The intensity changes of the *d* series, however, are not observed clearly, as shown in Fig. 6-5. By

comparing with the experimental result at pumping of n = 0, the relative intensities of the d series show the different patterns. The increase in the populations are only observed at {1, 2} and {2, 1} peaks. Furthermore, the increases in the populations are very limited, and the relative intensities are not kept between before and after the pumping. The peak appears at the position between {2, 1} and {2, 2} is observed. However, the intensity of the peak is not changed by the pumping. The expectation in the previous session for the behavior of d = 2 by pumping of n = 1 is wrong. The behavior of the population at d = 2 by pumping of n = 1 could not be discussed since the population change is not clearly observed.

6.3.4 The dependence of the pumping power

In order to check the mechanism for the pumping, the power dependence of the pumping laser is observed. Figure 6-6 shows the temporal behavior of the integrated intensities of each peak by pumping of the n = 1 main peak. Each peak corresponds to each pumping power. The relative pumping powers are measured by using an MCT detector by inserted a chopper at the front of that. The laser power is estimated about 2 mW without any attenuators at the n = 1 main peak. This measurement only takes the relative pumping powers. The information about the relative power is enough for the analysis to the pumping power dependence since the number of photons is proportional to the power of the laser. The pumping power dependence is measured for five pumping powers with changing the number of attenuators from 4 to 0. The relative laser powers are 1, 5.4, 27, 79, and 366 by normalized at the weakest power. These experiments are measured one after another from 4 attenuators to 0. Therefore the initial intensities of the spectra for each measurement does not have equal value even though each initial state

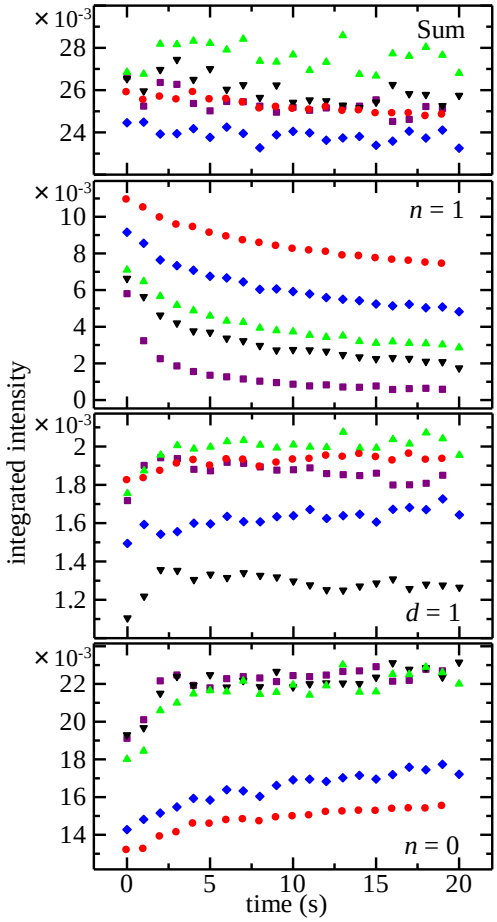

Fig. 6-6. The temporal behaviors of integrated intensities for each cluster peak. The relative pumping powers are 1 (red), 5.4 (blue), 27 (green), 79 (purple), and 366 (black).

is made by pumping of the n = 0 satellite peaks.

At 20 sec from starting the pumping, the population of n = 1 look to be stopping the decrease. The equilibrium population by each pumping power is bleached with increasing the pumping power. From the experimental results, the population of n = 1 would not become 0 if the laser power is not enough strong. It would indicate that the existence of the pass from the n = 0 state to n = 1. This phenomenon could occur that the *o*-H_2 in the second nearest neighbor of n = 0 cluster migrate to the first nearest neighbor of it. The possibility of this phenomenon is mentioned in Chap. 3.

6.3.5 The character of the *d* series

In order to check the character of the *d* series, the properties of the *d* series to the pumping on it are surveyed. Figure 6-7 shows the result by the pumping. The spectra have been offset. The trace (a) is the spectrum soon after pumping of the n = 0 main peak. Without pumping of n = 0, some peaks of the d = 1 series are still observed but the intensities of them are so weak. Therefore, the spectrum after pumping of n = 0 is set to an initial spectrum. The trace (b) shows the spectrum soon after pumping of {1, 1}. The peak is bleached and some of other peaks are also bleached their intensities but do not disappear. The trace (c) indicates the spectrum soon after pumping of {1, 2}. The peak is completely bleached out but {1, 1} is still observed. The trace (d), shown green, corresponds to the spectrum soon after pumping of (0, 0), thus it is the same situation with the trace (a) as an initial spectrum. The relative intensities of (a) and (d) are similar, therefore pumping of (0, 0) made the same spectral pattern at the *d* series. The top trace (e), shown yellow, is the spectrum soon after pumping of {1, 2}. These peaks named {1, 1}, {1, 3} and {1, 4} are observed. The relative intensity is no kept and the population of each peak of the *d* series is not conserved from before to after. The components are transferred to the other cluster structures, like the cluster structures for the satellite peaks of n = 0 and 1. Since the initial state is not in equilibrium, the immigrated population from the *d* series to

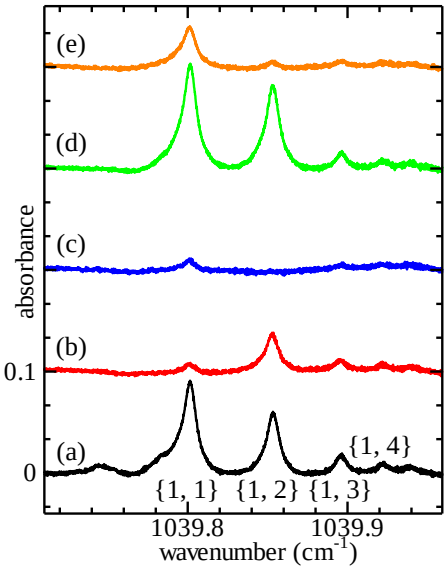

Fig. 6-7. The spectrum change at *d* series by pumping of each peak. Each spectrum is observed in order from the bottom trace according to the following conditions. Trace (a) initial spectrum. Trace (b) after pumping of {1, 1}. Trace (c) after successive pumping of {1, 2}. Trace (d) initial spectrum. Trace (e) after pumping of {1, 2}.

other clusters by the pumping could not be defined completely. The initial state is made by pumping of the n = 0 main peak, therefore, the population of d = 1 could be changed from the initial spectrum without pumping of the d peak.

The summary for the characters of the d series is that (1) they have the series that appear at the position of the middle for the n series. (2) they have the d' series for each d series, and each d' series has the similar pattern that looks like to be the blue shift from {1, 1} peak. (3) each d' peak can be bleached by the pumping. (4) the polarization dependence of the d' series of d = 1 is observed and the polar angle is estimated 68.6(42)° and 67.0(17)° for {1, 1} and {1, 2}, respectively. (5) the relative peak intensity for the d' series is changed by the pumping position. {1, 1} peak becomes the highest in the d' series of d = 1 when the n = 0 main peak is pumped. On the other hand, {1, 2} peak becomes the highest when the n = 1 main peak is pumped. From these characters, the d series would originate from some cluster structures with CH_3F.

§ 6.4 Discussion

6.4.1 Fitting analysis for n = 0 pumping

In order to estimate each reaction rate of each peak, these pump-probe experimental results are analyzed by using a model function. Figure 6-8 shows the image of the relaxation processes at

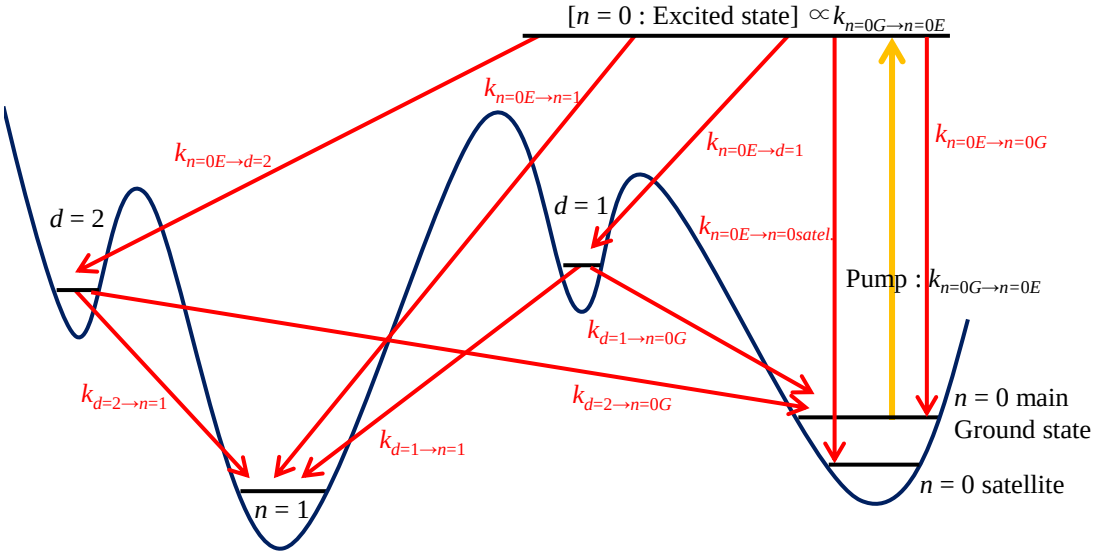

Fig. 6-8. The schematic diagram of the relaxation processes at pumping of the n = 0 main peak. The trace of dark blue shows the image of binding potential. The red and yellow arrows indicate the relaxation and pump process, respectively.

pumping of the n = 0 main peak. This figure shows a potential image, but the vertical and horizontal axes and the potential depth don't have the meaning of quantitative properties. The pumping laser beam excites the n = 0 cluster from the ground state to the excited state. The parameter $k_{n=0G\rightarrow n=0E}$ depends on the power of the pumping beam. If the *o*-H_2 molecule is migrated to the first nearest neighbor site or the crystal structure is changed for the *d* series, the population which correspond to n = 0 is transferred to other cluster's structures. Figure 6-8 does not show the processes of the relaxations from the *d* series to the n = 0 satellite and from n = 1 states to both states of n = 0 however the possibility wouldn't be denied. In fitting analysis, we attempted the fitting analysis with containing the passes. The spectral change at pumping of the n = 0 main peak indicates that the population in the satellite peaks such as (0, 4) and (0, 5) increase, as shown in Fig. 4-7(c). It should be considered to the model for relaxations. From this fact, we divide the population of n = 0 into two; the bleached one and the increased one. From the image of the relaxation processes for pumping of the n = 0 main peak as shown in Fig. 6-8, the reaction rates would be estimated by the fitting analysis. Each arrow in Fig. 6-8 corresponds to each transition and each k indicates the reaction rate of each transition. The rate equations used in the fitting analysis are expressed as

$$
\begin{aligned}
\frac{dN_{n=0}^{GS}}{dt} &= -k_{n=0G\rightarrow n=0E}N_{n=0}^{GS} + k_{n=0E\rightarrow n=0G}N_{n=0}^{EX} + k_{d=1\rightarrow n=0G}N_{d=1} + k_{d=2\rightarrow n=0G}N_{d=2} \\
\frac{dN_{n=0}^{EX}}{dt} &= k_{n=0G\rightarrow n=0E}N_{n=0}^{GS} \\
&\quad -(k_{n=0E\rightarrow n=0G} + k_{n=0E\rightarrow n=0\,satel.} + k_{n=0E\rightarrow n=1} + k_{n=0E\rightarrow d=1} + k_{n=0E\rightarrow d=2})N_{n=0}^{EX} \\
\frac{dN_{n=0\,satel.}}{dt} &= k_{n=0E\rightarrow n=0\,satel.}N_{n=0}^{EX} \\
\frac{dN_{d=1}}{dt} &= k_{n=0E\rightarrow d=1}N_{n=0}^{EX} - (k_{d=1\rightarrow n=1} - k_{d=1\rightarrow n=0G})N_{d=1} \\
\frac{dN_{d=2}}{dt} &= k_{n=0E\rightarrow d=2}N_{n=0}^{EX} - (k_{d=2\rightarrow n=1} - k_{d=2\rightarrow n=0G})N_{d=2} \\
\frac{dN_{n=1}}{dt} &= k_{n=0E\rightarrow n=1}N_{n=0}^{EX} + k_{d=1\rightarrow n=1}N_{d=1} + k_{d=2\rightarrow n=1}N_{d=2} \\
\frac{dN_{SUM}}{dt} &= 0 \\
N_{SUM} &= N_{n=1} + N_{d=1} + N_{d=2} + N_{n=0\,satel.} + N_{n=0}^{EX} + N_{n=0}^{GS}
\end{aligned}
\qquad (6-1)
$$

In this formula, each N shows the number or the population for each n or d state, and that information is distinguished by the subscript. The n = 0 main peak is distinguished only "n = 0" in order to be simplified. The ground state (GS) and excited state (EX) are shown by the superscript for $N_{n=0}$. The populations are approximately same as the integrated intensities of each peak. The populations of $N_{n=0\ satel.}$ and $N_{n=0}$ are divided at the border of wavenumber. The border position is almost between (1, 3) and (1, 4) peaks. The reaction rate $k_{n=0E\rightarrow n=0G}$ corresponds to the relaxation from excited state to ground state by radiative and non-radiative processes; therefore, the rate includes Einstein coefficients A and B. We assume that the decay times of spontaneous emission and stimulated emission of CH_3F in solid p-H_2 are longer than that of non-radiative. The decay time of spontaneous emission for the ν_3 vibrational band of CH_3F was reported as 67 ms [92]. The decay time of non-radiative process has not been identified yet however the order of magnitude of it would be shorter than 1 ms, based on other molecule [63]. Therefore, we estimate the reaction rate $k_{n=0E\rightarrow n=0G}$ would be the same value with that of non-radiative process and we can treat it as one parameter without any conditions.

However, the parameters did not converge. Then, the fitting analysis was attempted with fixed some parameters (e.g. $k_{d=1\rightarrow n=0G}$) to 0, but the fitting results did not represent the experimental results well. The parameters were estimated, however, the 1 sigma of each parameter and the residual errors were so large. The reason would be that we don't observe the excited state and the fitting function has too many parameters to be determined. For fitting analysis to estimate the reaction rates, the process in Fig. 6-8 should be more simplified. The simple model for constructing the fitting function is shown in Fig. 6-9. The new simplified model is only considered the structural change of the clusters. Each arrow and k in this figure shows the pass and the reaction rate of structural change between each cluster, respectively. From Fig. 6-9, the reaction rates could be estimated by the fitting analysis. Some possible passes, like d = 1 to n = 0 satellite, are not depicted. The reason is explained

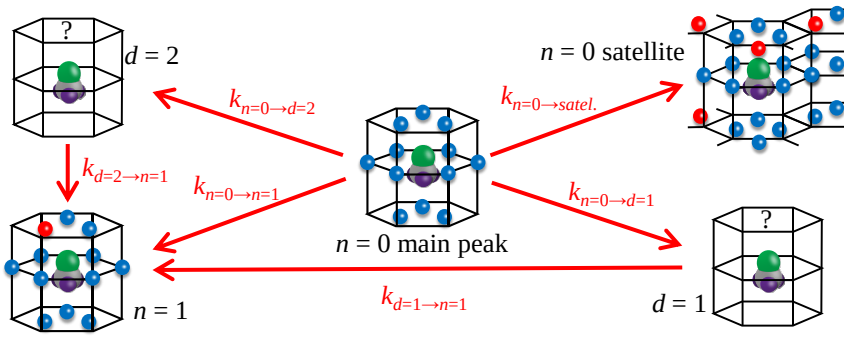

Fig. 6-9. The image of the structural change by the pumping of the n = 0 main peak. The red arrows indicate the passes for each structural change.

below. From the model in Fig. 6-9, the rate equations used in the fitting analysis are expressed as

$$\frac{dN_{n=0}}{dt} = -(k_{n=0\to n=0\ satel.} + k_{n=0\to n=1} + k_{n=0\to d=1} + k_{n=0\to d=2})N_{n=0}$$

$$\frac{dN_{n=0\ satel.}}{dt} = k_{n=0\to n=0\ satel.}N_{n=0}$$

$$\frac{dN_{d=1}}{dt} = k_{n=0\to d=1}N_{n=0} - k_{d=1\to n=1}N_{d=1}$$

$$\frac{dN_{d=2}}{dt} = k_{n=0\to d=2}N_{n=0} - k_{d=2\to n=1}N_{d=2} \qquad (6-2)$$

$$\frac{dN_{n=1}}{dt} = k_{n=0\to n=1}N_{n=0} + k_{d=1\to n=1}N_{d=1} + k_{d=2\to n=1}N_{d=2}$$

$$\frac{dN_{SUM}}{dt} = 0$$

$$N_{SUM} = N_{n=1} + N_{d=1} + N_{d=2} + N_{n=0} + N_{n=0\ satel.}$$

In this formula, the meaning of each N is the same for Eq. (6-1). Equation (6-2) still has so many parameters. In order to estimate each parameter more accurately, the simultaneous fitting to the two experimental results for pumping (0, 0) and (0, 3) is attempted. At the experiment pumping (0, 3), the populations around (0, 3) are bleached and that around the n = 0 main peak increases; therefore, the populations of n = 0 are also divided into two. Thus, at the pumping of (0, 3), the positions of the cluster's images for n = 0 main peak and n = 0 satellite are exchanged in Fig. 6-9. Some parameters do not become common values for the two different experiments. However, the reaction rates $k_{d=1\to n=1}$ and $k_{d=2\to n=1}$ are not relevant to the pumping power and the pumping position. Therefore, we can treat them as the same values for the two experiments. The possible relaxation processes, like d = 1 to n = 0 satellite, were also considered. However, at the fitting analysis, these values became nearly equal to 0 with large errors, thus they did not converge. Therefore, in this model, these two processes could be ignored. The results of the fitting by using the linear differential the equations (6-2) to the two experiments are described in Fig. 6-10. The pumping powers at pumping (0, 0) and (0, 3) are 2 mW and 0.5 mW, respectively. The estimated fitting parameters are listed in Table 6-1. The values in the parentheses show the values of 1σ statistical error. The behaviors by the pumping are represented by the fitting functions. However, the residual errors shown in the top figures of Fig. 6-10 are not small by comparing with the values of the d series.

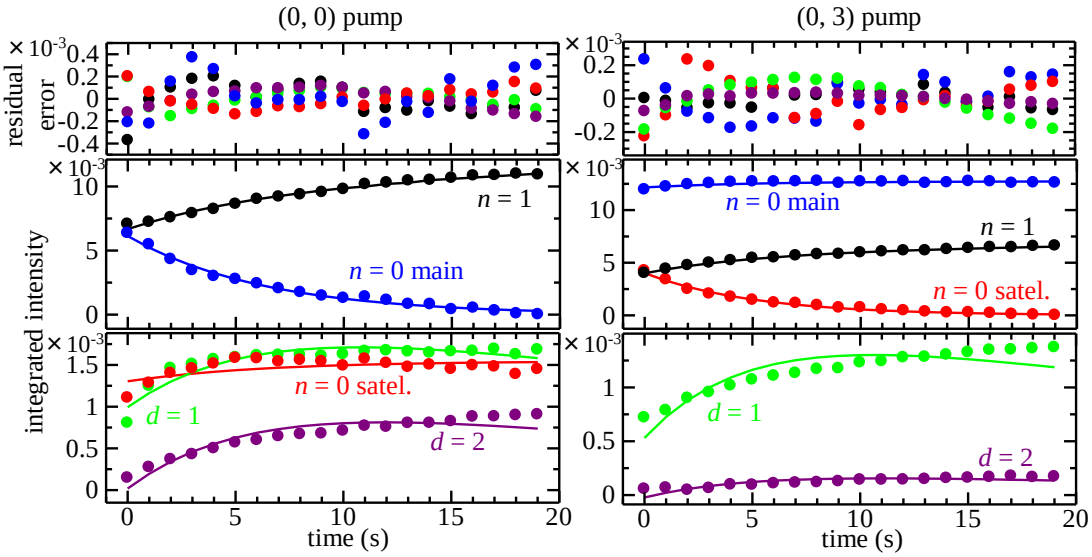

Fig. 6-10. The temporal behavior of integrated intensities for each cluster peak by the pumping. The pumping powers at pumping of (0, 0) and (0, 3) are 2 mW and 0.5 mW, respectively. Each mark and trace show the experimental results and fitting analysis results. The left figures: the result of pumping of the n = 0 main peak. The right figures: the result of pumping of (0, 3) peak. Top figures show the residual errors. Each color corresponds to each cluster's peak.

Table 6-1. The estimated fitting parameters for the pumping experimental results of n = 0 and (0, 3)

Simultaneous			
(0, 0) pump		(0, 3) pump	
$k_{n=0\rightarrow n=1}$	$9.8(6)\times10^{-2}$	$k_{n=0\ satel.\rightarrow n=1}$	$8.7(4)\times10^{-2}$
$k_{n=0\rightarrow n=0\ satel.}$	$2.8(4)\times10^{-2}$	$k_{n=0\ satel.\rightarrow n=0}$	$6.3(2)\times10^{-3}$
$k_{n=0\rightarrow d=1}$	$5.7(6)\times10^{-2}$	$k_{n=0\ satel.\rightarrow d=1}$	$3.4(4)\times10^{-2}$
$k_{n=0\rightarrow d=2}$	$1.2(4)\times10^{-2}$	$k_{n=0\ satel.\rightarrow d=2}$	$3.2(4)\times10^{-2}$
$k_{d=1\rightarrow n=1}$		$2.2(4)\times10^{-2}$	
$k_{d=2\rightarrow n=1}$		$3.6(10)\times10^{-2}$	

One cause of this residual error would be that the reaction rates do not have the same values with time for each cluster. As seen in Fig. 4-7(c), the peak called n = 0 originates from some clusters which are formed by one CH_3F molecule and some o-H_2 molecules in above its second nearest neighbor sites. Therefore, the reaction rate could be changed for the number of o-H_2 around the CH_3F. In the n = 0 clusters, some clusters with many o-H_2 molecules could be changed their structure easier than others with a few o-H_2 molecules. Based on this discussion, the reaction rates after a few seconds from starting the pumping would be faster than the one after ten seconds from starting the pumping. Other possibility is that the spontaneous emission could affect the absorption intensity. In this analysis, we assumed that the effect of the spontaneous emission was neglected.

This assumption was based on one hypothesis that the non-radiative process would be much faster than radiative processes. We should estimate the decay time of non-radiative process of CH_3F in solid *p*-H_2 more accurately by theoretical or experimental approach.

In this analysis, we estimate the average of the reaction rates for each cluster and that could be one of the causes of the residual error in this analysis. It should be noted that this analysis could only check the processes of the structural change for the cluster by the pumping roughly.

6.4.2 The pumping power dependence for $n = 1$

Following the fitting analysis for the population changes by pumping $n = 0$, the experimental results of the pumping power dependence are also analyzed with similar model functions. The experimental results in Fig. 6-3 and Fig. 6-5 show that the *d'* series of $d = 1$ are changed their intensities by pumping $n = 0$ and 1. On the other hand, the *d'* series of $d = 2$ are only changed their intensities by pumping $n = 0$. Therefore, the transition processes to the *d* series should be changed by the pumping position. As seen in Fig. 6-6, the populations of $n = 0$, 1 and $d = 1$ are changed with the pumping time. Furthermore, the summed populations of each cluster keep constant with time. It would mean that the effect of the stimulated emission is not so large. Therefore, we can assume that the relaxation process form the excited state to ground state is mainly non-radiative. In such case, the vibrational energy of the cluster by the pumping is released to the crystal and raises the temperature around the cluster [94]. The peak position of CH_3F is shifted with the increase of the temperature [57], as mentioned in Chap. 3. Based on the previous research, the shift rate is about 0.001 cm^{-1}/K between 2 K and 5 K. Until the temperature decreases to the equilibrium point, thus 2 K, the resonant frequency of the cluster would be shifted. Since the line width of the pumping laser beam is estimated narrower than 10 MHz, the pumping beam is not able to pump the cluster while the resonance frequency is shifted. It means that there would be other states between excited state and ground state at 2 K. The model for the relaxation processes at pumping $n = 1$ is depicted in Fig. 6-11. The P indicates that the pumping power and α shows absorption coefficient. The pumping power would be proportional to the population at the excited state. The relaxation process from the excited state to the ground state of the $n = 1$ cluster could not be treated one process since the temperature of the crystal around the cluster would be higher soon after the relaxation by non-radiative process, as mentioned above. The relaxation process in the ground state of $n = 1$ in hot environment is treated one process approximately. The population at the excited state would correlate to the population that transfer to $n = 0$ and $d = 1$ structures. From Fig. 6-11, the rate equations used in the fitting analysis

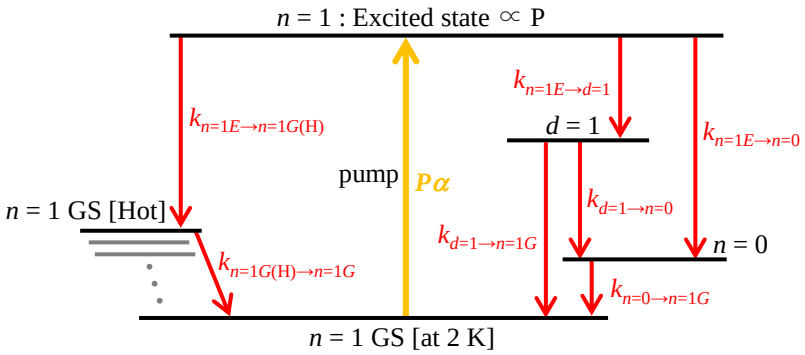

Fig. 6-11. The schematic diagram of the relaxation processes at pumping n = 1. The black trace shows the each state. The gray traces show the ground states of the n = 1 cluster in high temperature in order from the top. The red and yellow arrows indicate the relaxation and pumping processes, respectively.

are expressed as

$$\frac{dN_{n=1}^{GS}}{dt} = -P\alpha N_{n=1}^{GS} + k_{n=0\to n=1G}N_{n=0} + k_{d=1\to n=1G}N_{d=1} + k_{n=1G(H)\to n=1G}N_{n=1}^{GS(H)}$$

$$\frac{dN_{n=1}^{EX}}{dt} = P\alpha N_{n=1}^{GS} - \left(k_{n=1E\to n=1G(H)} + k_{n=1E\to d=1} + k_{n=1E\to n=0}\right)N_{n=1}^{EX}$$

$$\frac{dN_{d=1}}{dt} = k_{n=1E\to d=1}N_{n=0}^{EX} - (k_{d=1\to n=0} + k_{d=1\to n=1G})N_{d=1}$$

$$\frac{dN_{n=0}}{dt} = k_{n=1E\to n=0}N_{n=0}^{EX} + k_{d=1\to n=0}N_{d=1} - k_{n=0\to n=1G}N_{n=0} \qquad (6-3)$$

$$\frac{dN_{n=1}^{GS(H)}}{dt} = k_{n=1E\to n=1G(H)}N_{n=1}^{EX} - k_{n=1G(H)\to n=1G}N_{n=1}^{GS(H)}$$

$$\frac{dN_{SUM}}{dt} = 0$$

$$N_{SUM} = N_{n=1}^{GS} + N_{n=1}^{EX} + N_{d=1} + N_{n=0} + N_{n=1}^{GS(H)}$$

In this formula, the meaning of each term is the same with Eq. (6-1). The coefficients P and α represent pumping power and absorption, respectively. The $P\alpha$ corresponds to the number of the absorption. The population of ground states of n = 1 at 2 K and at other higher temperature are described *GS* and *GS*(*H*) by superscript, respectively. At the simultaneous fitting for the five experimental results with the different pumping powers, the coefficient P is fixed to each value. The pumping powers are calculated from two values: one is the relative pumping power measured in

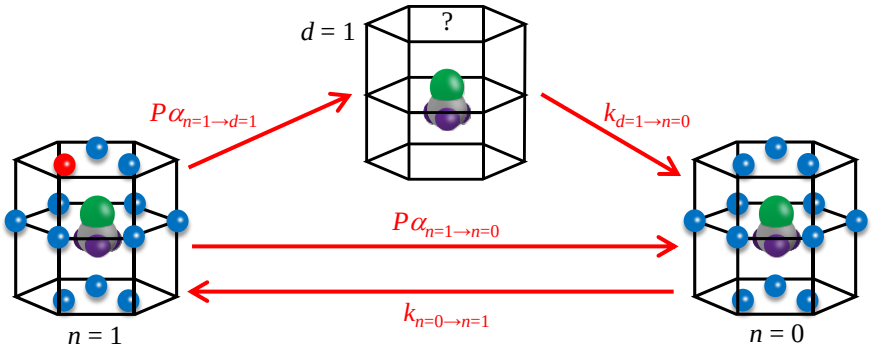

Fig. 6-12. The image of the structural change by the pumping n = 1. The red arrows indicate the passes for each structural change.

each experiment, and the other is the estimated beam power that is 2 mW without any attenuators. Each k is estimated as a common value for all pumping powers. However, the fitting analysis with Eq. (6-3) does not represent the experimental results well. Each parameter was not estimated. One of the reasons would be that the passes of the structural change for the cluster are not only from the excited state of n = 1. We do not know when the structural change is happened. The arrows to d and n = 0 states in Fig. 6-11 are only from the excited state however it could be possible from the ground state of n = 1 in hot environment. In addition, the integrated intensity of n = 1 could include the population of the n = 1 state in hot environment. The resonant frequency is shifted if the cluster is in the hot environment, as mentioned above. Therefore, the pumping beam does not pump the cluster in hot environment. However, the integrated intensity of n = 1 is calculated with containing the satellite peaks of n = 1 from the probing spectrum. If the shifted peak appears around the satellite peaks in probing spectrum, the population at ground state in hot would be included $N_{n=1}^{GS}$.

Following the failure of the above fitting analysis, we attempt to analyze the pumping power dependence by the same way for the experimental result at pumping n = 0. Fig. 6-12 shows the image of the structural change for the clusters by pumping of n = 1. This model is only considered the structural change of the clusters, as Fig. 6-9. Each arrow and k in this figure shows the pass and the reaction rate of structural change between each cluster, respectively. Some passes (e.g. from d = 1 to n = 1) could be possible, however, they are not included. The reason is mentioned below. The pumping power P has the same meaning of the number of the photons of the pumping laser beam. $P\alpha_{n=1\to n=0}$ and $P\alpha_{n=1\to d=1}$ correspond to the rate of occurrence for the structural change of the clusters. Therefore, the meaning of α is not equal to the general meaning of absorption coefficient. From Fig. 6-12, the reaction rates could be estimated by the fitting analysis. The rate equations used in the fitting analysis are expressed as

$$\frac{dN_{n=1}}{dt} = -(\alpha_{n=1\to d=1} + \alpha_{n=1\to n=0})PN_{n=1} + k_{n=0\to n=1}N_{n=0}$$

$$\frac{dN_{n=0}}{dt} = \alpha_{n=1\to n=0}PN_{n=1} + k_{d=1\to n=0}N_{d=1} - k_{n=0\to n=1}N_{n=0}$$

$$\frac{dN_{d=1}}{dt} = \alpha_{n=1\to d=1}PN_{n=1} - k_{d=1\to n=0}N_{d=1} \qquad (6-4)$$

$$N_{SUM} = N_{n=1} + N_{d=1} + N_{n=0}$$

$$\frac{dN_{SUM}}{dt} = 0$$

In this formula, the meaning of each term is the same with Eq. (6-2). At the simultaneous fitting for the five experimental results with the different pumping powers, the coefficient P is fixed to each value. The pumping powers are calculated from the same way for Eq. (6-3). Each k is estimated as a common value for all pumping powers. The absorption coefficients α are estimated as different values for each pumping power. The results of the simultaneous fitting analysis by using the linear differential the equations (6-4) to the five experiments are described in Fig. 6-13. The figures show the pumping power dependence of n = 1, d = 1 and n = 0 in (b), (c), and (d), respectively. Figure 6-13(a) indicates the residual errors of all results. The estimated fitting parameters are listed in Table 6-2.

Some estimated coefficients have large 1 σ statistical errors. The fitting carves for the

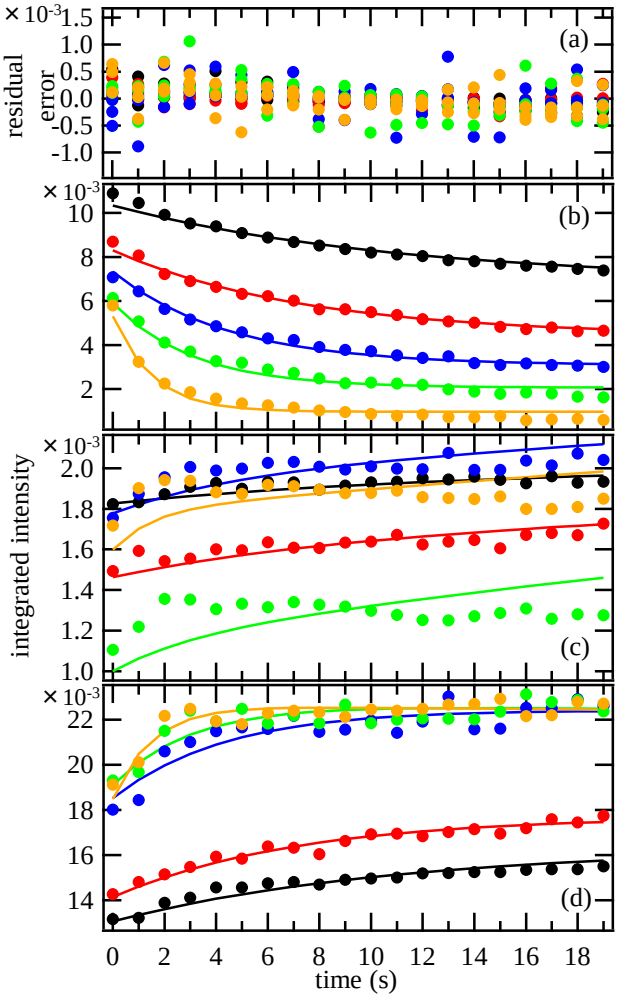

Fig. 6-13. The pumping power dependence. The temporal behavior of the integrated intensities for each cluster peak by pumping of n = 1 with changing the pumping power. (a) residual errors. (b), (c), and (d) show the result of n = 1, d = 1, and n = 0, respectively. The relative pumping powers are 1 (black), 5.4 (red), 27 (blue), 79 (green), and 366(orange).

Table 6-2. The estimated fitting parameters for the experimental results pumping n = 1with changing the pumping power

P (μW) [a]	$\alpha_{n=1\rightarrow n=0}$	$\alpha_{n=1\rightarrow d=1}$	$k_{d=1\rightarrow n=0}$ [b]	$k_{n=0\rightarrow n=1}$ [b]
5.5	$1.1(1)\times10^{-2}$	$1.9(7)\times10^{-3}$		
30	$3.4(2)\times10^{-3}$	$4.3(16)\times10^{-4}$		
1.5×10^{2}	$1.2(1)\times10^{-3}$	$1.3(5)\times10^{-4}$	$3.4(16)\times10^{-2}$	$2.9(2)\times10^{-2}$
4.3×10^{2}	$6.7(4)\times10^{-4}$	$6.1(1)\times10^{-5}$		
2.0×10^{3}	$3.0(2)\times10^{-4}$	$3.2(13)\times10^{-5}$		

[a] The values are fixed
[b] Common to all powers

d = 1 do not represent well the experimental results, as shown in Fig. 6-13(c). The possible relaxation processes from d = 1 to n = 1 and from n = 0 to d = 1 were also considered. However, at the fitting analysis, these values became nearly equal to 0 with large errors; thus, they did not converge. Therefore, for this model, these two processes could be ignored.

In order to change the structure of the cluster, the cluster has to absorb a photon from the pumping beam. Therefore, the rate of occurrence of the structural change would be proportional to the number of the photons which they absorb. The coefficients α related to the absorption ratio of the n = 1 cluster should be a common value for every pumping power if the absorbed power is proportional to the pumping power, namely the number of photons. However, the value of α changes with the pumping power, as seen in Table 6-2. The rate for the structural change of the clusters are estimated from $\alpha_{n=1\rightarrow n=0}\times P$ and $\alpha_{n=1\rightarrow d=1}\times P$, and the estimated values are shown in Fig. 6-14(a) and (b), respectively. As mentioned above, the rate of the structural change of the cluster is proportional to the absorbed power. Therefore, we treat the products of the α and P as absorbed power below. The estimated absorbed powers are not linear to the pumping powers, as shown in Fig. 6-14. The cause would be that the effect of the ground state of n = 1 in hot environment, as mentioned above. The behaviors look similar with a saturated absorption. In order to discuss the possibility of the hot state, we attempt to analyze the pumping power dependence.

If the resonance frequencies for the ν_3 band of CH_3F are completely same value for all target molecules, the absorption ratio α could be expressed as a function of the pumping power P as follows [93],

$$\alpha(P) = \frac{\alpha(0)}{1 + P / P_s} \qquad (6-5)$$

$\alpha(0)$ corresponds to the value at $P = 0$, thus it indicates the linear absorption. P_s shows the saturation power. From this equation, the absorbed power $P\alpha(P)$ would be represented as the following function,

$$P\alpha(P) = \frac{P\alpha(0)}{1 + P / P_s} = \frac{\alpha(0)}{1/P + 1/P_s} \qquad (6-6)$$

The fitting results with Eq. (6-6) are depicted as a red trace in Fig. 6-14. The fitting parameters for $P\alpha_{n=1\rightarrow n=0}$ are estimated as $P_s = 5.7(25) \times 10^2$ μW and $\alpha(0) = 1.3(4) \times 10^{-3}$. As mentioned above, the values of $P\alpha$ estimated from the experimental results are not the same meaning of the absorbed power in general. Therefore, the estimated coefficient α is not the linear absorption. The parameters for $P\alpha_{n=1\rightarrow d=1}$ are estimated with large statistical errors. The fitting results do not represent the experimental results well and the saturation powers P_s are not determined accurately. It would be derived from that the data points are too few to determine the curvature and the parameters. Another possible cause is that the model function is not good for the experimental results. In above analysis, one assumption that the resonance frequency for the ν_3 band of CH_3F is absolutely same for all target molecules is used. However, the resonance frequency of CH_3F could be changed if the environment around the CH_3F molecule is changed.

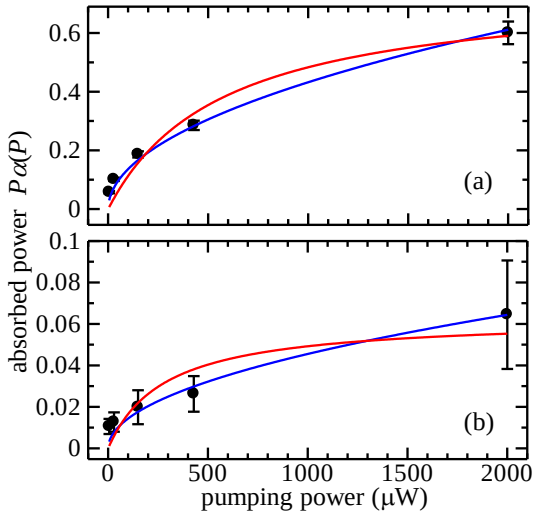

Fig. 6-14. The pumping power dependences of the absorbed power. (a) $\alpha_{n=1\rightarrow n=0} \times P$. (b) $\alpha_{n=1\rightarrow d=1} \times P$. The black circle shows the estimated value. The red and blue traces indicate the fitting results with Eq. (6-6) and Eq. (6-7), respectively.

The vibrational energy of the cluster by pumping is released to the crystal and increases the temperature around the cluster [94]. The peak position of CH_3F is shifted with the increase of the temperature [57], as mentioned above. Following this assumption, the decay time of the thermal energy around the cluster could affect the interval to the next absorption. Based on one hypothesis that the inhomogeneous line width by increasing the temperature follows one Gaussian, the saturated

absorption character would be represented by the following equation.

$$P\alpha(P) \propto \frac{\alpha(0)P}{\sqrt{1+P/P_s}} \qquad (6-7)$$

In this research, the shift would only be the red sides from the peak position therefore the equation is not perfectly same with the one for Gaussian. The fitting results to the absorbed power by Eq. (6-7) are depicted as a blue trace in Fig. 6-14. The curvature looks better to represent the absorbed powers than the fitting results with Eq. (6-6), however, the parameters are not converged. It might be derived from the number of the data points are not enough. From the fitting analysis with two different functions, we conclude that Eq. (6-7) would be better for representing the experimental result. It means that the resonant frequency would be shifted. In order to discuss more detail for the pumping power dependence, the pump-probe experimental results at higher and lower pumping power have to be observed. The experimental results of the pumping power dependence show that the resonant frequency of the cluster is shifted by increasing the local temperature and the phenomenon could affect the efficient of the absorbed power of the pumping beam.

In addition, one interesting phenomenon was observed in our laboratory. In this thesis, only the phenomenon at the C-F stretching mode of the ν_3 band of CH_3F has been introduced. However, the spectra with the C-H stretching mode of the ν_1 and $2\nu_5$ bands were surveyed by using cw optical parametric oscillator (OPO) system [95]. The frequency ranges of the ν_1 and $2\nu_5$ bands of CH_3F are around 2962 cm^{-1} and 2859 cm^{-1}, respectively. The absorption spectrum peaks at both bands have broad linewidth than the ν_3 band, but they also have the series by the CH_3F-(o-H_2)$_n$ clusters [87]. If one peak of the n series at the ν_3 band was bleached, the line shape at the $2\nu_5$ band was also changed. This phenomenon is easy to understand since the bleached peak at the $2\nu_5$ band originates by the cluster that was bleached at the ν_3 band. However, if the peak at the $2\nu_5$ band was pumped, the peak was not bleached and the line shapes at both bands were not changed. The results would indicate that the mechanism of the migration of the o-H_2 molecule in the cluster with CH_3F does not depend on the thermal energy, but depend on the vibrational modes. The thermal energies of the pumping beams for the ν_3 and $2\nu_5$ are around 1500 K and 4100 K, respectively. Therefore, if the migration mechanism only relates to the thermal energy, the migration of o-H_2 would be much occurred when the peak at the $2\nu_5$ band is pumped. This phenomenon should be identified in order to understand the mechanism of the dynamics at the local structure by the pumping beam. Theoretical studies are desired to confirm it.

6.4.3 The origin of *d* series

From the pump-probe experimental results, the fact becomes much clear that the *d* series relate to the CH_3F cluster. The *d* series could be one intermediate state for n = 0 and 1 from the fitting analyses. The characters of the *d* series are confirmed from our experiments and summarized in Sec. 6.3.5. From these characters, one of the possible origins for the *d* series is that the double-substitutional trapping site model. This possibility has been introduced in some previous studies for CO_2 and SiF_4 molecules [96,97]. The previous studies did not have the critical evidence to determine the origin for this structure. Based on this assumption, the peaks of the *d* series originate from the clusters described by CH_3F in the double sites and *d*-th *o*-H_2 molecules around it.

In order to form this model, one new vacancy at the first nearest neighbor site of CH_3F is necessary. The energy for forming the vacancy in the *p*-H_2 crystal was estimated around 150 K by the theoretical approach [48]. The local *p*-H_2 crystal around CH_3F could easily get this energy from the pumping beam since CH_3F absorbs around 1040 cm^{-1}, thus it is nearly 1500 K. From the viewpoint of energy for forming the vacancy, the substitutional trapping sites model is possible.

If the *o*-H_2 in the first neighbor site of CH_3F is migrated and the site becomes vacancy, the space for CH_3F would be larger than one site. The peak shift (the *n* series) would be mainly caused by the intensity of the interaction between CH_3F and *o*-H_2. If the vacancy changes the distance between CH_3F and *o*-H_2, the intensity of interaction between them could also be changed and the peak position could be shifted. The origin of d = 1 would correspond to the cluster with CH_3F in double substitutional trapping sites and one *o*-H_2 molecule in its first nearest site. From the simple image, the peak position of the *d* series could be explained qualitatively. However, the double substitutional trapping site model would be difficult to analyze because the position for the center of the mass of the CH_3F would not be defined. The image in the previous research was depicted that the center of mass migrates to the center of the double vacant sites as seen in Fig. 4 in Ref. 96. In other previous research, the theoretical calculation result described that the center of mass of Al atom in double sites is in the position of the middle between its original substituted site and the new vacancy site [98]. However, at the position, the distance between CH_3F and *p*-H_2 in its nearest sites become closer even if the *p*-H_2 molecules form the hcp structure strictly. In fact, one vacancy might make some distortion in the *p*-H_2 crystal therefore the distance between CH_3F and *p*-H_2 molecules could be much closer. The *d* series could be observed for a several hours with weak intensities. This experimental result suggests that the cluster structure is not so unstable. The image might be hard that the CH_3F molecule stays in its original substituted site and one vacancy around CH_3F keeps the

form for a several hours.

From the polarization spectroscopy, the polar angle for $d = 1$ is a little larger than the other main n series. It would mean that the C_3 axis of CH_3F for the d series is much closer to the XY plane. Based on an assumption that the center of the mass of CH_3F moves to the center of the double vacant sites, the direction of C_3 axis of CH_3F would be aligns on the axis that connects to the double vacancy sites. The polar angle of CH_3F in the d series could be divided into two cases: one is that the new vacancy is made at in-plane (IP) for the CH_3F in the cluster, and the other is that the one is made at out-of-plane (OP). In the former case, the polar angle of CH_3F becomes 90°, and in the latter one, θ becomes 35.26°. By following this model, the average of the polar angle could be estimated. From the discussion in Chap. 5, CH_3F in the cluster is tilted from the c-axis of p-H_2 crystal, as seen in Fig. 5-8. The vacancy would be made at the site which is one of the vertexes of the triangle or square that are penetrated by the C_3 axis of CH_3F. These are four IP sites and three OP sites. Therefore, the average of the polar angle for the double-substitutional trapping site model would be 66.54°. The fitting result indicates that the polar angle is estimated $68.6(42)^\circ$ and $67.0(17)^\circ$ for {1, 1} and {1, 2}, respectively. The fitting result and this calculation result are good agreement. This estimation supports the double-substitutional trapping site model for the d series.

The d series has four or more the d' peaks, however, the origins of them have not been obviously yet. The peak intensities of the d' series are changed by the pumping. The spectrum patterns are changed by the pumping position of the n series, as seen in Fig. 6-3 and 6-5. In addition to this, each peak can be bleached by the pumping beam. Each d peak would originate from each formation of the clusters. One assumption is that the position of o-H_2 in the double substituted sites model would change the peak position. For the n series, the distance between CH_3F and the first nearest neighbor sites is the same. On the other hand, for the double substituted sites model, that becomes different. Therefore, the site of o-H_2 would make the peak position shift. It would be main issue of the research from now on.

§ 6.5 Conclusion

The structural changes by the pumping laser were surveyed. By using two QC lasers, the processes of the structural change by the pumping beam were observed at the first time. In order to estimate each reaction rate of each cluster, these pump-probe experimental results were analyzed by using some model functions. The fitting result showed that the rates of the structural change for the $n = 1$

cluster are not proportional to the pumping power. It would mean that the local thermal energy of the *p*-H_2 crystal around CH_3F is increased and the resonance frequency of the CH_3F in the cluster is shifted. The thermal relaxation process in solid *p*-H_2 around dopant has not been studied yet. The pump-probe experiments at other pumping power could estimate the decay time of the thermal energy around dopant. The research could contribute to understand the mechanism of the relaxation of the thermal energy around dopant. Furthermore, it also contributes to develop the knowledge of the migration of *o*-H_2 molecules around the dopants. The theoretical and experimental studies for it are desired.

The characters of the *d* series were studied. From some experimental results, the *d* series would originate from the clusters described by CH_3F in double substituted sites. In order to determine the origin of it, some additional researches have to be done.

Chapter 7 Conclusions and future prospect

This research surveyed the local structure of *p*-H_2 crystal around dopant CH_3F by using high resolution QC lasers.

From this research, some influences of the dopant molecule to the local structure of solid *p*-H_2 were cleared. Furthermore, the knowledge about the interaction between *o*-H_2 molecules and CH_3F would be improved.

The temporal behaviors of the absorption spectrum of CH_3F-(*o*-H_2)$_n$ were observed. This research investigated that the nuclear spin conversion rate of *o*-H_2 molecules in the first nearest neighbor site of CH_3F. The estimated self-conversion rate has large uncertainty, and the value is the same order with the previous study [5]. The catalyzed-conversion rate is also estimated by the fitting analysis. The decay time is 24.4(8) hours and it is longer than that in the previous studies [16]. The main cause of the inconsistency would be the difference of the experimental ways. This is the first time to estimate the catalyzed-conversion rate between one *o*-H_2 and one dopant molecule. From this research, we found that the catalyzed-conversion rate of *o*-H_2 by CH_3F is faster than the self-conversion rate, but the difference between them are not so big. The effect of CH_3F is not only to do the catalyzed-conversion, but also to accelerate the self-conversion by making *o*-H_2 come close to it. The achievement in this research could contribute not only to the knowledge for the system of CH_3F in solid *p*-H_2, but also the development of the detailed physical implications of nuclear spin conversion of *o*-H_2 with the dopant in the solid *p*-H_2. This result suggests that the effects of the dopant molecules should be divided into some parts.

From some experimental results, new satellite series were found to the lower energy side of each main peak of the ν_3 band of CH_3F embedded in a *p*-H_2 crystal. All the peaks showed a common red shouldered line profile, which corresponds to partly resolved transitions of *ortho*- and *para*- CH_3F. Some experimental results may suggest that these satellite series originate from a family of CH_3F clusters involving *o*-H_2 in second nearest neighbor sites. A model function assuming this idea was used to resolve the observed spectrum into each Lorentzian component, and then the detailed features of these series were studied. The peak intervals in the series are not as equally spaced as the main series, but there is a strong resemblance to the satellite series. We proposed that the effect of *o*-H_2 molecules in the second nearest neighbor site of CH_3F could not be ignored.

The polarization dependence of the ν_3 vibrational transition of CH_3F, whose rotational motion is hindered in *p*-H_2 crystal, was observed. The experimental results were well explained by a simple

six-way vacancy model and the alignment angle in the crystal is determined. The CH_3F is not aligned along the *c*-axis but tilted to 64° from the *c*-axis. This is the first time to estimate the alignment of dopant molecule in solid *p*-H_2 by experimentally. The method to estimate the alignment of the dopant can be used for other dopant molecules. The knowledge of the orientation of the dopant molecules is very important. For example, the surveys which need to switch the direction of dopant molecules should know the alignment of the dopant. This result could contribute to such kind of researches which use the direction of dopant molecules. Furthermore, by using this experimental way, a new physical phenomenon could be found. CH_3F molecule is in the group which cannot rotate in solid *p*-H_2. The fact that CH_3F is not aligned along the *c*-axis was found in this research. However, the alignments of the other dopants which cannot rotate in solid *p*-H_2 have not been surveyed yet. Therefore, a new physical phenomenon could be found when the dopant which is aligned along the *c*-axis of solid *p*-H_2. This result should be verified with the more precise theoretical calculation based on the molecular interaction of CH_3F and H_2. We hope the alignment of molecules in *p*-H_2 crystal will be elucidated from this experimental approach and theoretical approach in the future.

The structural changes by the pumping laser were surveyed. By using two QC lasers, the processes of the structural change by the pumping beam were observed at the first time. In order to estimate each reaction rate of each cluster, these pump-probe experimental results were analyzed by using some model functions. The fitting result showed that the rates of the structural change for the $n = 1$ cluster are not proportional to the pumping power. It would mean that the local thermal energy of the *p*-H_2 crystal around CH_3F is increased and the resonance frequency of the CH_3F in the cluster is shifted. The thermal relaxation process in solid *p*-H_2 around dopant has not been studied yet. The pump-probe experiments at other pumping power could estimate the decay time of the thermal energy around dopant. The research could contribute to understand the mechanism of the relaxation of the thermal energy around dopant. Furthermore, it also contributes to develop the knowledge of the migration of *o*-H_2 molecules around the dopants. The theoretical and experimental studies for it are desired.

In addition, some unknown peaks such as the *d* series and $n = 3$' peak have surveyed the characters and the origins for them were estimated. Some theoretical supports are quite important for the determination of the origins of these peaks. Some infrared absorption peaks that have not been assigned have remained.

For the future research, I would like to suggest some experiments. One is that we should survey the pump-probe experiment with changing the temperature of the sample. This experiment could

improve the knowledge of the mechanism. The experiment should keep the crystal volume, therefore, the method of making the crystal should be changed. The sample made by the deposition method is not good for the observation of the temperature dependence since it can be sublimated. One method is a liquid epitaxial method that was reported [26]. It should be comfortable for this experiment.

The second is that we should observe the pumping power dependence. By this experiment, the saturation power for this target cluster could be determined. The results could contribute the knowledge of the relaxation process of the thermal energy in the crystal. Furthermore, the mechanism of the migration of *o*-H_2 around CH_3F could be solved by this research.

The third is for the nuclear spin conversion rate. We should investigate the temporal behavior of the whole CH_3F clusters. In this research, we observed the spectrum of the cluster for n = 0 - 3. If we observe the n = 0 - 12, the phenomenon for the migration of *o*-H_2 around CH_3F could be cleared. Moreover, the mechanism at the n = 3 cluster could be solved.

The theoretical studies are quite important to construct the cluster model. Some models that are introduced in this thesis such as double-substitutional trapping site model are still one of the candidates for the unassigned peak. We believe that the combination of the theoretical and experimental studies could determine the cluster structures and solve the issues have not been revealed.

Bibliography

[1] W. Heisenberg, Z. Phy. **41**, 239 (1927)

[2] T. Hori, Z. Phy. **44**, 834 (1927)

[3] D. M. Dennison, Proc. R. Soc. A **115**, 483 (1927)

[4] J. Van Kranendonk: *Solid Hydrogen*, Theory of the properties of solid H_2, HD, and D_2, Plenum, New York (1983).

[5] S. Washuburn, R. Schweizer, and H. Meyer, J. Low Temp. Phys. **40**, 187 (1980)

[6] A. H. Larsen, F. E. Simon, and C. A. Swenson, Rev. Sci. Instrum. **19**, 266 (1948)

[7] L. Farkas, L. Sandler, J. Chem. Phys. **8**, 248 (1940)

[8] G. E. Schmauch, A. H. Singleton, Ind. Eng. Chem. **56**, 20 (1964)

[9] E. Ilisca, and S. Sugano, Phys. Rev. Lett. **57**, 2590 (1986)

[10] E. Ilisca, Phys. Rev. Lett. **66**, 667 (1991)

[11] S. A. FitzGerald, K. Allen, P. Landerman, J. Hopkins, J. Matters, and R. Myers, J. L. C. Rowsell, Phys. Rev. B **77**, 224301 (2008)

[12] T. Kosone, A. Hori. E. Nishibori, Y. Kubota, A. Mishima, M. Ohba, H. Tanaka, K. Kato, J. Kim, J. A. Real, S. Kitagawa, and M. Takata, R. Soc. Open Sci. **2**, 150006 (2016)

[13] V. Shevtsov, P. Malmi, E. Ylinen, M. Punkkinen, Phys. B **284**, 385 (2000)

[14] V. Shevtsov, E. Ylinen, P. Malmi, and M. Punkkinen, Phys. Rev. B **62**, 386 (2000)

[15] L. A-. Marguin, A.-M. Vasserot, Chem. Phys. Lett. **460**, 82 (2008)

[16] L. A-. Marguin, A.-M. Vasserot, A. Lekic, Chem. Phys. Lett. **470**, 228 (2009)

[17] I. F. Silvera, Rev. Mod. Phys. **52**, 393 (1980)

[18] C. Kittel: *Introduction to Solid State Physics*, 4th ed., John Wiley & Sons, Inc. (1971)

[19] Elizabeth J. Allin, W. F. J. Hare and R. E. MacDonald, Phys. Rev. **98**, 554 (1955)

[20] W. F. J. Hare, Elizabeth J. Allin and H. L. Welsh, Phys. Rev. **99**, 1887 (1955)

[21] Elizabeth J. Allin, T. Feldman, and H. L. Welsh, J. Chem. Phys. **24**, 1116 (1956)

[22] M.-C. Chan, M. Okumura, Charles M. Gabrys, L.-W. Xu, Brent D. Rehfuss, and T. Oka: Phys. Rev. Lett. **62**, 32 (1989)

[23] M.-C. Chan, M. Okumura, C. M. Gabrys, L.-W. Xu, B. D. Rehfuss, and T. Oka, Phys. Rev. Lett. **66**, 2060 (1991)

[24] M.-C. Chan, S. S. Lee, M. Okumura, and T. Oka, J. Chem. Phys. **95**, 88 (1991)

[25] K. E. Kerr, T. Momose, D. P. Weliky, C. M. Gabrys, and T. Oka, Phys. Rev. Lett. **72**, 3957

(1994)

[26] D. P. Weliky, T. J. Byers, K. E. Kerr, T. Momose, R. M. Dickson, T. Oka, Appl. Phys. B **59**, 265 (1994)

[27] M. Mengel, B. P. Winnewisser, and M. Winnewisser, Phys. Rev. B **55**, 420 (1997)

[28] M. Mengel, B. P. Winnewisser, and M. Winnewisser, J. Low Temp. Phys. **111**, 757 (1998)

[29] M. Mengel, B. P. Winnewisser, and M. Winnewisser, J. Mol. Spectrosc. **188**, 221 (1998)

[30] T.Oka, Annu. Rev. Phys. Chem. **44**, 299 (1993)

[31] Y. Zhang, T. J. Byers, M.-C. Chan, T. Momose, K. E. Kerr, D. P. Weliky, and T. Oka, Phys. Rev. B **58**, 218 (1998)

[32] M.-C. Chan, L.-W. Xu, C. M. Gabrys, and T. Oka, J. Chem. Phys. **95**, 9404 (1999)

[33] Y. Miyamoto, M. Fushitani, D. Ando, and T. Momose, J. Chem. Phys. **128**, 114502 (2008)

[34] M. E. Fajardo, C. M. Lindsay, and T. Momose, J. Chem. Phys. **130**, 244508 (2009)

[35] J. H. Du, L. Wan, L. Wu, G. Xu, W. P. Deng, A. W. Lin, Y. Chen, S. M. Hu, J. Phys. Chem. A **115**, 1040 (2011)

[36] Y. Miyamoto, M. Tsubouchi, T. Momose, J. Phys. Chem. A **117**, 9510 (2013)

[37] F. M. Mutunga. S. E. Follett, and D. T. Anderson, J. Chem. Phys. **139**, 151104 (2013)

[38] P. Das, and Y.-P. Lee, J. Chem. Phys. **140**, 244303 (2014)

[39] S. Tam, and M. E. Fajardo, H. Katsuki, H. Hoshina, T. Wakabayashi, and T. Momose, J. Chem. Phys. **111**, 4191 (1999)

[40] M. Bahou, H. Witek, and Y.-P. Lee, J. Chem. Phys. **138**, 074310 (2013)

[41] T. Nakamura, Prog. Theor. Phys. **14**, 135 (1955)

[42] K. Motizuki, T. Nagamiya, J. Phys. Soc. Jpn. **11**, 93 (1956)

[43] O. Nagai, and T. Nakamura, Prog. Theor. Phys. **24**, 432 (1960)

[44] S. Luryi, and J. V. Kranendonk, Can. J. Phys. **57**, 136 (1979)

[45] S. Luryi, and J. V. Kranendonk, Can. J. Phys. **57**, 933 (1979)

[46] D. Scharf, M. L. Klein, and G. J. Martyna, J. Chem. Phys. **97**, 3590 (1992)

[47] F. Operetto, F. Pederiva, Phys. Rev. B **73**, 184124 (2006)

[48] F. Operetto, F. Pederiva, Phys. Rev. B **69**, 024203 (2004)

[49] F. Operetto, F. Pederiva, Phys. Rev. B **75**, 064201 (2007)

[50] T. Zeng, H. Li, R. J. Le Roy, and P.-N. Roy, J. Chem. Phys. **135**, 094304 (2011)

[51] P. L. Raston, W. Jager, H. Li, R. J. Le Roy, and P.-N. Roy, Phys. Rev. Lett. **108**, 253402 (2012)

[52] K. Yoshioka and D. T. Anderson, J. Chem. Phys. **119**, 4731 (2003)

[53] K. Yoshioka and D. T. Anderson, J. Mol. Struct. **786**, 123 (2006)

[54] S. M. Freund, G. Duxbury, M. Römheld, J. T. Tiedje, T. Oka, J. Mol. Spectrosc. **52**, 38 (1974)

[55] B. Gauthier-Roy, L. Abouaf-Marguin, and F. Legay, Chem. Phys. **46**, 31 (1980)

[56] B. Gauthier-Roy, C. Alamichel, A. Lecuyer, L. Abouaf-Marguin, J. Mol. Spectrosc. **88**, 72 (1981)

[57] A. R. W. McKellar, A. Mizoguchi, and H. Kanamori, J. Chem. Phys. **135**, 124511 (2011)

[58] A. R. W. McKellar, A. Mizoguchi, and H. Kanamori, Phys. Chem. Chem. Phys. **13**, 11587 (2011)

[59] M. Fushitani, N. Sogoshi, T. Wakabayashi, T. Momose, T. Shida, J. Chem. Phys. **109**, 6346 (1998)

[60] M. Fushitani, and T. Momose, J. Chem. Phys. **116**, 10739 (2002)

[61] H. Kawasaki, A. Mizoguchi, H. Kanamori, J. Mol. Spectrosc. **310**, 39 (2015)

[62] H. Kawasaki, A. Mizoguchi, H. Kanamori, J. Chem. Phys. **144**, 184306 (2016)

[63] N. Toda, A. Mizoguchi, and H. Kanamori, J. Chem. Phys. **132**, 234504 (2010)

[64] Y.-P. Lee, Y.-J. Wu, and J. T. Hougen, J. Chem. Phys. **129**, 104502 (2008)

[65] L. Abouaf-Marguin and A.-M. Vasserot, Low Temp. Phys. **37**, 4 (2011)

[66] B. A. Tom, S. Bhasker, Y. Miyamoto, T. Momose, and B. J. McCall, Rev. Sci. Instrum. **80**, 016108 (2009)

[67] M. E. Fajardo, and S. Tam, J. Chem. Phys. **108**, 4237 (1998)

[68] Y. Futami, S. Kudoh, M. Takayanagi, M. Nakata, Chem. Phys. Lett. **357**, 209 (2002)

[69] R. F. Curl, F. Capasso, C. Gmachl, A. A. Kosterev, B. McManus, R. Lewicki, M. Pusharsky, G. Wysocki, F. K. Tittel, Chem. Phys. Lett. **487**, 1 (2010)

[70] M. Bloom, Physica. **23**, 767 (1959)

[71] A. J. Berlinsky, W. M. Hardy, Phys. Rev. B **8**, 5013 (1973)

[72] L. A.-Marguin, A.-M. Vasserot, C. Pardanaud, J. Stienlet, X. Michaut, Chem. Phys. Lett. **454**, 61 (2008)

[73] L. A.-Marguin, A.-M. Vasserot, C. Pardanaud, J. Chem. Phys. **130**, 054503 (2009)

[74] R. F. Buzerak, M. Chan, and H. Meyer, J. Low Temp. Phys. **28**, 415 (1997)

[75] Y.-P. Lee, Y.-J. Wu, R. M. Lees, L.-H. Xu, J. T. Hougen, Science **311**, 365 (2006)

[76] K. Yoshioka, P. L. Raston, and D. T. Anderson, Int. Rev. Phys. Chem. **25**, 469 (2006)

[77] D. Ramm, H. Meyer, J. Low Temp. Phys. **40**, 173 (1980)

[78] R. Oyarzun, J. V. Kranendonk, Can. J. Phys. **50**, 1494 (1972)

[79] V. Shevtsov, A. Scherbakov, P. Malmi, E. Ylinen, M. Punkkinen, J. Low Temp. Phys. **104**. 211 (1996)

[80] J. Tang, Y. Xu, A. R. W. McKellar, W. Jäger, Science **297**, 2030 (2002)

[81] N. S. Sullivan, M. Devoret, B. P. Cowan, C. Urbina, Phys. Rev. B **17**, 5016 (1978)

[82] A. F. Schuch, R. L. Mills, D. A. Depatie, Phys. Rev. **165**, 1032 (1968)

[83] Y. Miyamoto, T. Momose, J. Phys. Chem, A **115**, 14254 (2011)

[84] J. H. Constable, C. F. Clark, and J. R. Gaines, J. Low. Temp. Phys. **21**, 599 (5/6) (1975)

[85] C. H. Townes, A. L. Schawlow: Dover Publications, Inc, "Microwave Spectroscopy" (1975).

[86] M. Miki, T. Momose, J. Low. Temp. Phys. **26**, 661 (2000)

[87] Y. Miyamoto, T. Momose, H. Kanamori, J. Chem. Phys. **137**, 194315 (2012)

[88] C. M. Lindsay, M. E. Fajardo, Knowledge Bank (2006), *INFRARED SPECTROSCOPY OF HYDROGEN CYANIDE IN SOLID PARAHYDROGEN*, http://hdl.handle.net/1811/30973, (Accessed 2017-01-26)

[89] M. E. Fajardo, C. M. Lindsay, J. Chem. Phys. **128**, 014505 (2008)

[90] S. Tam, M. E. Fajardo, Rev. Sci. Instrum. **70**, 1926 (1999)

[91] W. Demtröder: *Laser Spectroscopy*, 3rd ed., Springer-Verlag, (2002)

[92] A. A. Radzig, B. M. Smirnov: *Reference Data on Atoms, Molecules, and Ions*, Springer-Verlag, (1985)

[93] K. Shimoda: *Introduction to Laser Physics*, 2nd ed., Springer-Verlag, (1991)

[94] H. Hoshina, T. Wakabayashi, T. Momose, T. Shida, J. Chem. Phys. **10**, 5728 (1999)

[95] Y. Miyamoto, A Mizoguchi, and H. Kanamori, (to be submitted)

[96] S. Tam, M. E. Fajardo, Low Temp. Phys. **26**, 653 (2000)

[97] H. Ooe, Y. Miyamoto, S. Kuma, N. Sasao, K. Kawaguchi, Chem. Phys. Lett. **631**, 54 (2015)

[98] D. T. Mirijanian, M. H. Alexander, G. A. Voth, Chem. Phys. Lett. **365**, 487 (2002)

Acknowledgements

This thesis has been the product of much dedication on the part of several individuals. Therefore, I would like to express my gratitude in acknowledging them here.

First, I would like to express my deepest gratitude to Dr. Hideto Kanamori, who has given me not only the knowledge and basic skills, but also his time and guidance in discussing my research. His suggestions have often helped me to overcome obstacles and move to the next stage of my research. He exemplifies what a researcher should be. His commitment to his students is without limits.

Second, it would be nearly impossible not to acknowledge Dr. Asao Mizoguchi, with whom all my research began. He taught me not only the foundations for all of my experimental procedures but also how to best conduct research and analysis. I believe that my research could not have been achieved without his contributions.

Thirdly, I would like to express my gratitude to the "Academy for Global Leadership" program. Prof. K. Yamada has given me so many opportunities to challenge my own beliefs, but beyond that he has also afforded me so much of his own time. His dedication and commitment are of an unprecedented quality that deserves the highest praise. Furthermore, Prof. S. Furui and many other members at the program who have aided me in so many different ways. In addition, I firmly believe that I will treasure the relationships I have formed with other students in the program for life.

I wish to thank the members of Dr. Kanamori's laboratory. They have helped me to broaden my perspectives.

I am also grateful for the constructive discussions and advice on my research that I have been given by many other professors who I have met at various conferences. I would especially like to express my gratitude to Dr. M. Araki, Dr. M. Fukushima, Dr. H. Ishikawa, Dr. S. Kasahara, and Dr. M. Nakajima. All of them encouraged me so many ways.

In addition, I would like to express my gratitude to Dr. Y. Ohshima, and Dr. M. Kozuma. They gave me so many comments and advices to improve my doctoral thesis and research. In addition, I acknowledge Dr. Y. Aoki, and H. Foster for critically reading the paper.

Lastly, I am forever indebted to my family for their unconditional love. They have supported me through these past five years. You have given me the great honor of calling myself a son and a brother.

Thank you all.

December 2016

Hiroyuki Kawasaki